Modelling and analysis of electro-mechanical interactions in wind turbines

A thesis accepted by the Faculty of Aerospace Engineering and Geodesy of the University of Stuttgart in fulfilment of the requirements for the degree of Doctor of Engineering Sciences (Dr.-Ing.)

by

Fiona Dominique Lüdecke

born in Frankfurt am Main, Germany

Main referee:	Prof. Dr. Po Wen Cheng
Co-referee:	Prof. Alasdair McDonald
Date of defence:	15.12.2023

Stuttgart Wind Energy at Institute of Aircraft Design

University of Stuttgart

2024

Contents

Abbreviations and Symbols

List of Abbreviations

BDF	Backward differentiation formula
BI	Blade imbalance
BS	Bearing stiffness
CAD	Computer aided design
CFD	Computational fluid dynamics
DEL	Damage equivalent load
DFIG	Doubly-fed induction generator
DLR	German Aerospace Centre
DoF	Degree of freedom
EmeI	Electro-mechanical interaction
ETM	Extreme turbulence model
FA	Fore-aft
FEM	Finite element method
FFT	Fast Fourier Transformation
IEA	International Energy Agency

IEC	International Electrotechnical Commission
JNI	Java Native Interface
MB	Multi-body
MT	Monopile torsion
NREL	National Renewable Energy Laboratory
PMSG	Permanent magnet synchronous generator
RMSD	Root mean square difference
RQ	Research question
SS	Side-to-side
STEP	STandard for the Exchange of Product model data
WT	Wind turbine

List of Latin Symbols

B_r	Remanent flux density of magnets
J_A	Current layer density
J_s	Winding current density
c_D	Aerodynamic drag coefficient
$\mathbf{A}$	Area
$\mathbf{B}$	Induction
$\mathbf{b}$	Width
$\mathbf{c}$	Stiffness coefficient of spring or linearised bearing
$\mathbf{D}$	Equivalent dynamic bearing load
$\mathbf{DEL}$	Damage equivalent load
$\mathbf{e}$	Error

F	Force
f	Frequency
h	Height
I	Nominal current
i	Instantaneous current
k	Woehler exponent
l	Length
M	Torque or moment
m	Mass
N	Total number of a countable set
o	Gearbox ration
P	(active) Power
p	Empirical exponent for equivalent dynamic bearing loads
R	Radius
S	Load cycle amplitude
s	Placeholder variable
T	Time period
t	Time
U	Nominal voltage
u	Instantaneous voltage
v	Velocity
x	Position in cartesian coordinates along x-axis
y	Position in cartesian coordinates along y-axis
z	Position in cartesian coordinates along z-axis

List of Greek Symbols

Δ	Difference
β	Section width angle for discretised generator
$\delta_{\mathbf{0}}$	Air gap design length
δ	Air gap length
ϵ	Generator eccentricity
γ	Rotation angle around cartesian z-axis
κ	Sub-function for electromagnetic stiffness
$\mu_{\mathbf{0}}$	Vacuum magnetic permeablility, natural constant
$\mu_{\mathbf{r}}$	Relative magnetic permeability, material constant
ω	Rotational speed
ϕ	Magnetic flux
π	Transcendental number, natural constant
ρ	Density
$\tau_{\mathbf{p}}$	Pole pitch at generator rotor, generator design parameter
θ	Sector angle for discretised generator
φ	Electrical phase angle
ξ_1	Winding factor
ζ	Tolerance factor

List of Subscripts

0	Reference value
B	Bearing

D	Drag
DoF	Degree of freedom
G	Generator
H	Hub
M	Monopile
N	Nacelle
PM	Permanent magnet
RA	Rotor assembly
R	Rated
SS	Side-to-side
S	Stator
TP	Transition piece
T	Tower
Tip	Blade tip
abs	Absolut
base	Baseline model
cg	Center of gravity
co	Conductor
cy	Cycles
δ	Airgap
el	Electric
emag	Electromagnetic
i	Counter
in	Cut-in
j	Counter

lin	Linearised
max	Maximum
min	Minimum
out	Cut-out
ph	Phase
p	Pole pair
rel	Relative
rot	Rotating
s	Spring
stat	Non-rotating mass
tol	Tolerance
tor	Torsional
w	Windings
x	Direction in cartesian coordinates
y	Direction in cartesian coordinates

List of mathematical Operators

$P_{xx}(\cdot)$	Percentile of the vector in the brakkets of xx %
$\hat{(\cdot)}$	Amplitude
$\bar{(\cdot)}$	Mean value
$\vec{(\cdot)}$	Vector
$(\cdot)'$	Directional derivative
$\dot{(\cdot)}$	Time derivative
$\sim$	Proportional: indicates that the two variables left and right of it are proportional to each other
$\lvert\cdot\rvert$	Absolute value

$\mathbf{m}$	Matrix (bold variables)
$(\cdot) \in [xx, yy]$	Element of interval between xx and yy
$\sum_{i=1}^{N}$	Sum over a set of N values

Glossary

AeroDyn

Aerodynamic solver for blade element momentum theory around predefined airfoils by National Renewable Energy Laboratory (NREL) and integrated as aerodynamic module in *OpenFAST*

Arduino Uno

Microcontroller board

Bearinx

Commercial calculation module to design bearing configurations by Schaeffler Technologies

Bladed

Commercial wind turbine simulation software by DNV

Comsol Multiphysics

Commercial multi-physics simulation software

C

Programming language

Fortran

Programming language

GitHub

Cloud-based service for software development including version control and used to share software releases

HAWC2

Commercial wind turbine simulation software by DTU Wind Energy

HydroDyn

Hydrodynamic solver by National Renewable Energy Laboratory (NREL) and integrated as hydrodynamic module in *OpenFAST*

Java

Object-oriented programming language

Matlab/Simulink

Commercial programming software

OpenFAST

Open-source modular wind turbine simulation software by the National Renewable Energy Laboratory (NREL)

RT-Lab

Simulation platform for real-time simulations integrated in *Matlab/Simulink*

Rosco

Open-source tool set to design wind turbine controllers, used to design the official reference controller of the International Energy Agency (IEA) 15MW reference wind turbine, used in this work

Simpack

Commercial multi-body simulation software by Dassault Système

TurbSim

Open-source software to create turbulent wind fields created and distributed by National Renewable Energy Laboratory (NREL) and used to create input wind fields for *OpenFAST*

User Routine

Simpack internal functionality to extend program capabilities by programming in *Fortran* or *C* a new function for the solver, following a given function structure.

Kurzfassung

Der Beitrag der Windenergie zur Energiewende nimmt stetig zu. Dies beruht auf zwei Aspekten: dem Bau neuer Anlagen und der Vergrößerung der Anlagen. Insbesondere auf See liegt die Nennleistung neuer Anlagen inzwischen bei bis zu 16 MW und steigt weiter. Im Wesentlichen werden zwei Antriebsstrangkonzepte verwendet, mit Getriebe und ohne (sogenannte Direktantriebe).

Direktantriebe, die im Mittelpunkt dieser Arbeit stehen, zeichnen sich durch eine niedrige Drehzahl aus, die der Begrenzung der Blattspitzengeschwindigkeit dient. Dies führt zu großen Generatordurchmessern, die um die 10 m erreicht haben. Skalierungsgesetze zeigen, dass die strukturelle Stützmasse schneller wächst als die aktive Masse, die zur Energieerzeugung beiträgt. Daher werden neue Konstruktionsmethoden zur Verringerung der Masse benötigt. Die Generatorkonstruktion wird auf der Grundlage der gegebenen Eingangslasten optimiert und muss den Luftspalt zwischen Rotor und Stator stets sicherstellen. Dies wird in der Regel durch sehr hohe Anforderungen an die Steifigkeit der Hauptlager und der Tragstruktur des Generators erreicht, was das Potenzial zur Gewichtsreduzierung einschränkt.

In dieser Arbeit wird davon ausgegangen, dass die Auslegung von Windenergieanlagen auf der Grundlage einer Komponentenoptimierung nicht das beste Systemdesign gewährleistet. Ein verstärkt systemorientierter Ansatz erfordert jedoch neue, ganzheitliche Modellierungsmethoden zur Simulation von Windenergieanlagen, unter Berücksichtigung der elektromagnetischen Kräfte des Generators. Das erforderliche Systemmodell wird in dieser Arbeit durch Hinzufügen eines zusätzlichen radialen Freiheitsgrades zu dem Standard-Windenergieanlagenmodell abgeleitet. Zwei Generatormodelle mit unterschiedlicher De-

tailtiefe werden mit dem Windenergieanlagenmodell gekoppelt, ein analytisches und ein Finite-Elemente-Modell. Die Einflüsse der Modellanpassungen auf das Systemverhalten werden ermittelt.

Die Ergebnisse zeigen, dass niedrige Systemmoden durch die Modellierung in ihrer Eigenfrequenz beeinflusst werden können. Außerdem wird eine neue Systemmode eingebracht, die mit dem neuen Freiheitsgrad zusammenhängt. Darüber hinaus zeigt die Arbeit, dass der Regler für bestimmte Parameterkombinationen die neue Systemmode resonant anregt. Auch werden frequenzabhängige Rückkopplungen in die Aerodynamik identifiziert. Basierend auf dem Vergleich der beiden Generatormodelle verspricht das analytische Generatormodell einen guten Kompromiss zwischen Genauigkeit und Rechenzeit.

In einem zweiten Schritt werden die Auswirkungen der identifizierten Wechselwirkungen auf die Turbinenlasten innerhalb und außerhalb des Antriebsstrangs analysiert, d.h. im Hauptlager, am Turmkopf, am Turmfuß und an der Blattwurzel. Dazu werden die äquivalenten Lasten beider Modelle verglichen.

Der Belastungsvergleich zeigt, dass Komponenten innerhalb und außerhalb des Antriebsstrangs beeinflusst werden. Insbesondere die Hauptlager und der Turm weisen signifikante Laständerungen auf. Die Lasten können im Vergleich zum Standardmodell jedoch sowohl erhöht als auch verringert werden. Dies stützt die Hypothese dieser Arbeit, dass eine Systemdesignoptimierung vom Ergebnis der Komponentenoptimierung abweicht.

Darüber hinaus kann gezeigt werden, dass sich der zusätzliche radiale Freiheitsgrad und die elektromagnetischen Kräfte in einigen Fällen addieren und in anderen Fällen gegenseitig aufheben. Basierend auf den Ergebnissen dieser Arbeit ergeben sich Folgefragen, unter anderem zur Lebensdauerabschätzung.

Insgesamt trägt diese Arbeit zu einem besseren Verständnis der elektromechanischen Wechselwirkungen in getriebelosen Windenergieanlagen bei und gibt einen Einblick in die für deren Analyse erforderlichen Modellierungsansätze. Sie fördert damit den Weg zur systemorientierten Auslegung von Windenergieanlagen.

Abstract

The contribution of wind energy to the energy transition is steadily increasing. This growing contribution is driven by two aspects: the construction of new turbines and the increase in turbine size. In particular, for offshore sites, the nominal power of new turbines is now up to 16 MW and rising. Two main drive-train concepts are used, the geared and the direct-drive.

Direct-drives, the focus of this work, have a characteristically low speed in order to limit the blades' tip speed. This results in large generator diameters, which have reached around 10 m. Scaling laws show that structural support mass grows faster than active mass, contributing to power generation. Therefore, new design methods for mass reduction are desired. The generator design is optimised based on given input loads and must maintain the air gap between the rotor and stator at all times. Typically, this is achieved by very high main bearing and generator support structure stiffness requirements, limiting mass reduction potential.

In this work, it is assumed that designing wind turbines based on component optimisation does not ensure the best system design. However, moving to a more system-oriented approach requires new, holistic modelling techniques to simulate the wind turbine system, including electromagnetic forces from the generator. The required system model is derived in this thesis by adding a radial degree of freedom to the state-of-the-art wind turbine model. Two generator models of different fidelity are coupled to the wind turbine model, an analytical and a finite element model. Influences of the model adaptations on the system behaviour are identified. Structural component interactions are analysed and the effects of modelling on interactions with the aerodynamic solver and controller are investigated.

The results show that lower system modes can be affected in their natural frequency by the modelling. Furthermore, a new system mode is introduced which is related to the new degree of freedom. The controller shows a high excitation of the new system mode for specific parameter combinations. Frequency-dependent feedbacks into the aerodynamics are also identified. Based on the comparison of both generator models, the analytical generator model promises a good trade-off between accuracy and computation time.

In a second step, the effects of the identified interactions on turbine loads inside and outside the drive-train are analysed at the main bearing, the tower top, the tower base and the blade root. For this purpose, the equivalent loads of both models are compared.

The load comparison shows that components inside and outside the drive-train are affected by the modelling. In particular, the main bearings and the tower show significant changes in load. However, loads can be increased as well as decreased compared to the state-of-the-art model. This supports the hypothesis of this work that a system design optimisation will differ from the component optimisation result.

Furthermore, it can be shown that the added radial degrees of freedom and the electromagnetic forces add up in some cases and cancel each other out in other cases for load level changes. Based on the results of this work, follow-up questions arise, including lifetime estimation.

Overall, this work contributes to a better understanding of the electro-mechanical interactions in direct-drive wind turbines and provides insight into the modelling approaches required for their analysis. It thus promotes the way towards system-oriented design of wind turbines.

Acknowledgements

This work was carried out during my time as a researcher at the Stuttgart Chair for Wind Energy (SWE) at the University of Stuttgart. It would not have been possible to complete this work without the support of several people. I would like to thank all people who have supported me throughout the journey of my thesis.

I want to thank Prof. Dr. Po Wen Cheng for giving me the opportunity to focus my thesis on electro-mechanical interactions and to start a new field of interdisciplinary research at SWE. I also want to thank Prof. Dr. Nejila Parspour for supporting this topic from the electrical side. The trust they both gave me encouraged me to take on all the challenges of such an interdisciplinary topic and make it through to the successful end.

In addition, I want to express my gratitude to Prof. Dr. Alasdair McDonald for being my co-referee. His comments and input have been a great help in improving my research. And I very much appreciate the time and effort that Prof. Dr. Ewald Krämer has taken as the chairman of the examination committee.

During my work at SWE, I have had the honour of working with several colleagues whom I would like to thank. In particular, I would like to mention Vasilis Pettas, Ines Würth, Andrew Clifton and Mohammad Youssef Mahfouz. With their expertise and our discussions on technical and strategic aspects of the thesis, they have strongly supported me in shaping and enhancing my topic. Outside of SWE, I also had a great collaborator in Martin Schmid from the Institute of Electrical Energy Conversion (IEW) at the University of Stuttgart. Our discussions about the generators helped to put my investigations on solid ground. In addition to my colleagues, I would like to thank the students who supported my research

with their work. Special thanks go to Eva Rehe and Sangamithra Panneer Selvam.

I want to close with a very big thank you to my family and friends. They have been supporting and encouraging me through all the ups and downs such a work is connected with. Here, a very special thank you goes to my partner, Clemens. You have always been there to listen, to discuss or to review and just being the person I needed at that moment. I am filled with gratitude to have you as my partner.

Chapter 1

Introduction

"You never change things by fighting the existing reality.
To change something,
build a new model that makes the existing model obsolete."

Richard Buckminster Fuller, US architect and system theorist [1, p.137]

The European Union aims to install 510 GW of wind power capacity by 2030, in response to climate change and political circumstances [2, p. 142]. The suitable sites for the installation of Wind turbine (WT)s are limited due to multiple factors. Offshore, the feasibility of wind farms depends on shipping routes, water depth, and distance from shore. Moreover, the number of WTs that can be installed in a certain area is limited, e.g. due to wake effects, which can reduce the power output.

To use available sites more efficiently, manufacturers aim to increase the rated power per WT [3, p. 35]. Newly released WTs have a rated power up to 16 MW [4] and keep growing. These WTs often use direct-drive concepts. Scaling laws have been identified and utilised to expedite the design process of WTs with higher rated power. The scaling laws for direct-drive generators indicate a disproportionately large increase of generator mass compared to the power. This increase of mass affects the WT system design, as the generator of a horizontal axis WT is located on top of a tower of 100 m and more. The increase in tower top mass necessitates a higher tower stiffness to support the weight, while satisfying the prescribed natural frequency limits. Additional stiffness is usually attained using extra material, which runs against the objective of resource-efficient and economical designs.

Therefore, there is a need for new designs with reduced tower top mass. This involves

exploring lightweight design approaches and novel generator concepts. At the same, current design approaches try to minimise radial displacement of the generator. As a result, the drive-train can be considered as an independent subsystem with a pre-defined loading, which enables separate design optimisation. However, this requires a high radial stiffness in bearings and the generator frame, which contributes towards the increase in mass. These requirements need to be re-examined for the further development of large WTs. The assumption is made that a system-oriented design approach would better facilitate the identification of a global optimum.

WT design approaches are based on modelling. Due to the objective of high stiffness, current modelling assumes perfect alignment between the generator rotor and stator. The system design approach requires discarding this assumption. In consequence, appropriate modelling techniques have to be derived prior to applying the system design approach. These modelling method must include Electro-mechanical interactions (EmeI), as the generator, an electrical machine, is connected to the mechanical system of the WT.

The thesis aims to identify possible EmeIs in large WTs based on a system modelling approach. An electro-mechanical WT model is developed, including an additional, radial Degree of freedom (DoF) and a description of electromagnetic forces due to generator eccentricity. The model is analysed for EmeIs and the results are compared to a baseline model, which represents the state-of-the-art.

The thesis is structured as follows: In Chapter 2 the state-of-the-art of WT technology and modelling is introduced and provides a comprehensive overview of the theoretical background, deriving the Research questions (RQ). To describe the electromagnetic forces of the generator, two models of different level of complexity are used and compared. The model of high complexity requires a software coupling, which is introduced in Chapter 3, while the implementation of the WT and generator models is explained in Chapter 4. The conducted investigations and analysis results are outlined in Chapter 5. Ultimately, Chapter 6 summarises the presented work and results and provides an outlook on potential future work. All in all, the thesis delivers a first appropriate modelling technique to take EmeIs into account in future WT designs and provides insights to mechanisms causing EmeIs in WTs.

Chapter 2

State of the Art

Following the introduction, this chapter provides the needed theory for the analysis of EmeIs in WTs. Besides the knowledge about WT components and technology trends, modelling theory is key for the understanding of the present work. This requires reviewing technical and numerical aspects, as outlined in the following.

Section 2.1 provides insights into the technical concept of wind energy, and the specifics of the different components. A special focus is put on the drive-train concepts and the generator technology, as they are key to the EmeIs. Furthermore, technological trends supporting the outlined motivation of Chapter 1 are summarised.

The background of modelling and simulation is introduced in Section 2.2, explaining the background of mechanical and electromagnetic modelling. In addition, aspects of multi-fidelity modelling and co-simulations are explained, as the analysis of EmeIs in numerical simulations rely on those techniques.

Following the overview of needed technology and methodology, the state-of-the-art modelling of EmeIs and current research in the area are presented in Section 2.3. Based on the literature overview, concluding RQs for this work are outlined in Section 2.4.

2.1. Wind energy overview

Wind energy technology can be categorised by different aspects. As shown in Figure 2.1, one way to categorise WTs is their working principle. This divides WTs into horizontal

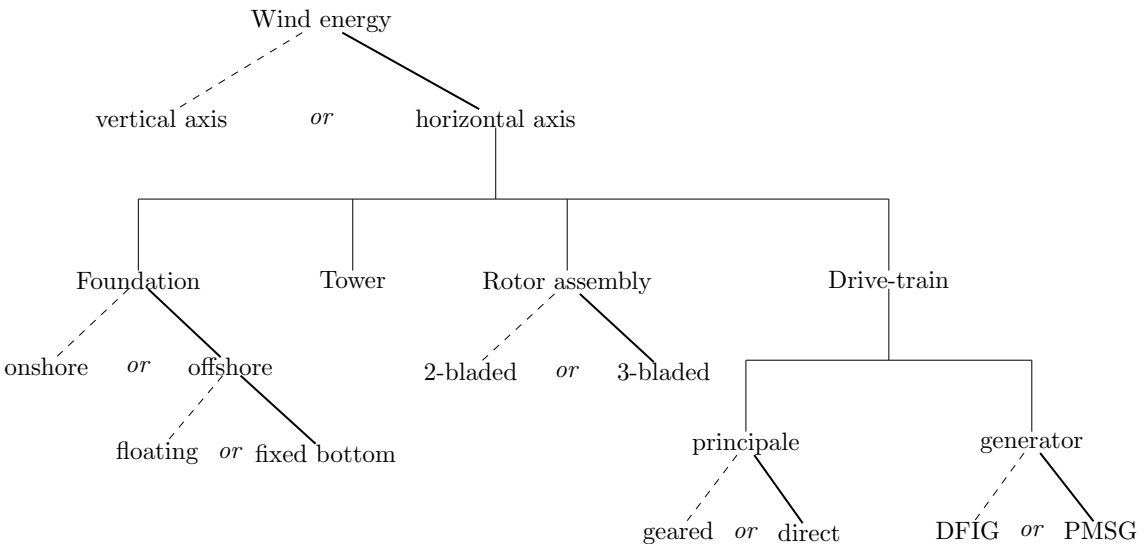

Figure 2.1.: Categorisation of WTs according to the most commonly used concepts. Solid lines connect the concepts applied in this thesis, whereas dashed lines illustrate alternative concepts.

and vertical axis WTs. Until now, the horizontal axis concept is dominating the market due to its higher power coefficient and lower load fluctuations than the vertical axis WTs [5]. Therefore, the present work will focus on this type of WTs.

Depending on the location, the WT needs a foundation for ground connection. In high level, the locations can be divided in onshore and offshore locations. The first meaning a site on land and the latter meaning a site out at the sea. The latter adds additional excitation forces due to hydrodynamic forces from waves and sea current. This kind of foundation can be further divided into fixed bottom and floating foundations. The floating foundations add additional movements to the system that complicate the system design and increase interactions. To limit the system complexity, this work will use a fixed bottom offshore foundation.

For horizontal axis WTs, a tower is placed on the foundation. The tower carries the rotor nacelle assembly. With a logarithmic wind profile, the mean wind speed increases with the height, and so does the energy available.

The first step of energy conversion happens at the rotor assembly. Modern WTs use the principle of lift to create aerodynamic forces at the rotor blades that lead to an aerodynamic torque acting on the drive-train shaft [6, pp. 124-134]. While the number of blades can vary, the dominating concept consists of three rotor blades. The more rotor blades are used, the higher the possible energy extraction from the wind is. But at the same time, more

blades mean higher costs. As the energy yield increases non-linear, with the highest increase for low numbers of blades, cost related optimisation has lead to three blades. In general, the rotor assembly can be placed in front of the tower from the perspective of the wind or behind. The first is called upstream WT. The latter is called downstream WT. Currently, the market is dominated by the upstream WTs [6, p. 144] and this concept is also used for the present work.

The aerodynamic torque causes the rotor assembly and the drive-train shaft to rotate. The rotation is then transmitted through the drive-train until it reaches the generator. There, the kinematic energy is transformed into electrical energy. The existing concepts for WT drive-trains and generators are introduced in the following two subsections.

2.1.1. Drive-train concepts

The power P transmitted through the drive-train equals the product of rotational speed ω and acting torque M, as given in Equation (2.1). The power is transmitted from the rotor assembly through the drive-train to the WT generator. The rotational speed of the rotor assembly is limited due to aerodynamics. Current blade design limits restrict the tip speed of the rotor blades v_{Tip} to a maximum of 100 $\frac{\mathrm{m}}{\mathrm{s}}$ for offshore applications [6, p. 136]. The blades' tip speed depends on the rotational speed and the rotor radius R, according to Equation (2.2). Therefore, a specific power transmitted through the drive-train with a low rotational speed means a high torque and vice versa a high rotational speed means a low torque.

$$P = \omega \cdot M \tag{2.1}$$

$$v_{\mathrm{Tip}} = \omega \cdot R \tag{2.2}$$

$$\omega_{\mathrm{G}} = o \cdot \omega_{\mathrm{RA}} \tag{2.3}$$

The two options of power transmission are reflected in the two major drive-train concepts, namely the direct-drive and the geared drive-train [7, 8]. The direct-drive configuration has a high generator torque and a low rotational speed. The shaft is directly connected to the generator. This means generator rotor and WT rotor have the same rotational speed. The geared configuration increases the rotational speed seen by the generator using a gearbox, placed between rotor assembly and generator. Here, the generator rotor has a rotational

speed ω_G equal to the product of WT rotor assembly rotational speed ω_{RA} and gear ratio o, as given in Equation (2.3). The direct-drive concept reduces the number of components that can fail, and failure statistics have shown that gear-box failures are a frequent reason for WT downtime [9]. Especially, at offshore sites the required maintenance needs to be kept low because of the lower accessibility, which leads to a preference of direct-drive concepts for offshore sites [10]. Moreover, the EmeIs, investigated in this work, are expected to be more dominant in direct-drive configurations. Therefore, this work uses a direct-drive configuration.

To enable the rotation of the rotor assembly, bearings are needed as important components of the drive-train. For direct-drive WTs three major concepts exist [10]. These concepts differ by the number of support points along the drive-train, from one to three. The number of support points mainly affects the non-torque load distribution. All concepts have their advantages and disadvantages, and they are used in current WT designs. In this work, a two-point concept is used.

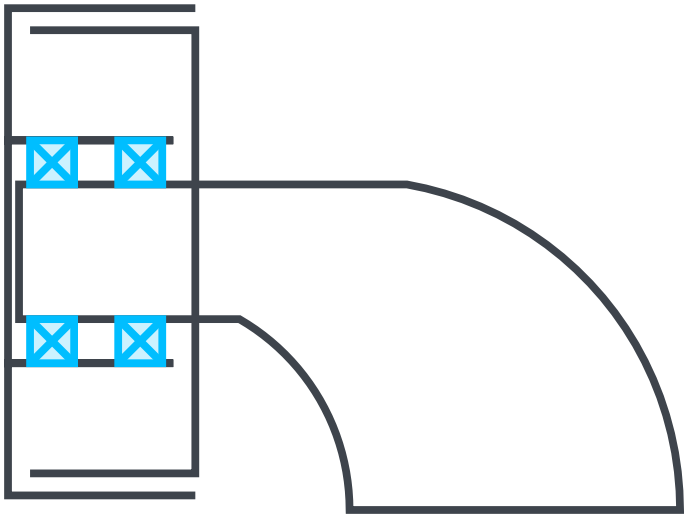

Figure 2.2.: Two-point main bearing concept for direct-drive WT

The two-point concept uses two bearings along the drive-train, as shown in Figure 2.2. Usually, one bearing is designed as fixed bearing and the second as floating bearing. The fixed bearing carries the axial loads of the drive-train. Both bearings share the radial drive-train loads. In this work, the downwind bearing is chosen to be the fixed bearing due to the used reference wind turbine.

2.1.2. Generators

The two drive-train concepts result in different characteristics of the generator. The geared concept with high rotational speed allows a compact generator with relatively low generator torque. The low rotational speed of the direct-drive concept leads to a large diameter to allow for the high generator torque [3, pp. 37-38]. Mainly, two types of generators are used in WTs: a Doubly-fed induction generator (DFIG) and a Permanent magnet synchronous generator (PMSG) [8]. In direct-drive configuration, mainly the PMSG is used [8]. It offers a higher efficiency and a lower mass [8]. Therefore, this work focuses on PMSG as electrical machine and the basic principle is explained in the following.

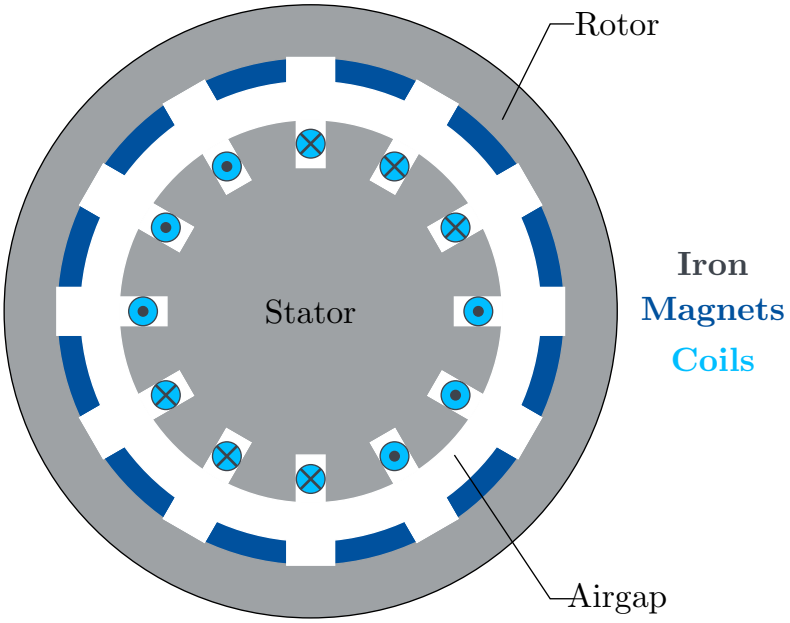

Figure 2.3.: PMSG with an outer rotor carrying surface mounted permanent magnets (dark blue) and an inner stator carrying coils (light blue) both made out of iron (gray) and separated by an air gap (white).

Figure 2.3 shows a schematic illustration of a PMSG. The PMSG uses permanent magnets (dark blue bars) on the generator rotor to create a magnetic field. The stator side has coil windings (light blue circles), where a current is induced by the rotating magnetic field of the rotor. The current leads to a second magnetic field at the stator side, following the rotor field. An air gap separates the two components.

Due to the two magnetic fields, surface forces act between rotor and stator. They have two components: tangential and radial forces. The tangential force results in a torque, experienced by the rotor and stator. The torque acting on the rotor equals the generator

torque, which is the counterpart to the aerodynamic torque on the shaft, coming from the wind. This ensures a constant rotational speed for a stable operating point.

The other component of the surface forces acts in radial direction. These forces lead to an attraction of stator and rotor towards each other.

$$F_{\text{emag}} \sim -\frac{1}{\delta^2} \tag{2.4}$$

Both components of the surface forces F_{emag} depend on the length of the local air gap δ,

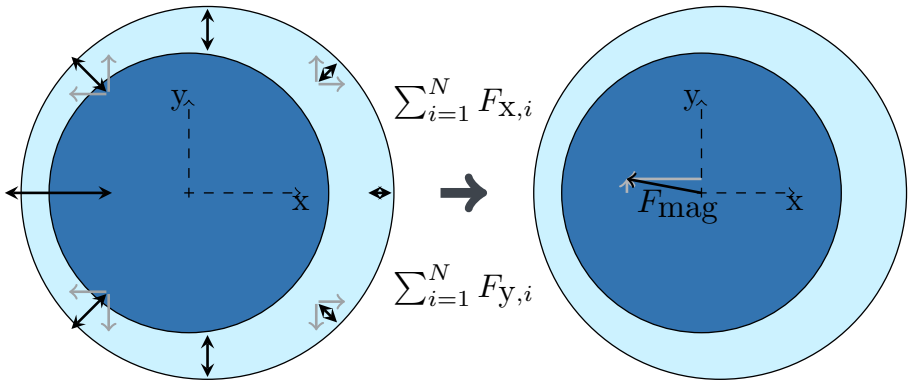

Figure 2.4.: Procedure to transform surface forces on a rigid body to summarized forces in the centre of gravity, by summing up the N discretised local forces $F_{\text{x},i}$ and $F_{\text{y},i}$ per direction and then get the summary force F_{emag} using the Pythagorean equation

according to Equation (2.4). The smaller the air gap, the higher the acting surface forces. Note that the dependence is highly non-linear.

Neglecting the deformations of the rotor and stator surface due to the distributed forces, they can be integrated over the surface giving the resulting force in the centre of gravity, as illustrated in Figure 2.4. In an ideal assembly, where the centres of the generator rotor and stator are aligned, and both bodies are ideally round, the air gap is uniform in all directions, as are the radial forces. Therefore, they act as surface stress without a resulting force at the centre of gravity.

But as soon as e.g. the centre of the rotor is moved with respect to the centre of the stator, the surface forces do not cancel out any longer. The resulting force increases with the eccentricity, as it attracts the two components in one direction stronger than the other. It is acting at the centre of gravity of the two components, similar to the case illustrated in Figure 2.4.

From Equation (2.4), it can be seen, that the attraction force increases non-linearly with

increasing eccentricity. To avoid serious damage to the generator, the stator and rotor must never touch each other. Therefore, it is important to maintain a minimum air gap at all times and especially during operation.

Even if the supporting bearings ensure a minimum air gap at all times, these forces can still cause significant vibrations [11]. It has been shown that the level of vibration depends on the pole slot combination [12] and the magnets' rotor design [13]. These mechanical vibrations due to electromagnetic forces are considered as EmeIs and are the key aspect of investigation in this work.

2.1.3. Trends in wind energy

The contribution of wind energy to the energy transition towards renewable energies was driven significantly by technological enhancements in recent years. Additionally, a trend towards offshore wind farms can be observed. Offshore wind farms experience more steady wind conditions due to reduced flow disturbance by the landscape. As a consequence, the mean wind speed is higher compared to an onshore site. Therefore, offshore wind farms promise higher annual energy production. Besides economic aspects, offshore wind farms avoid issues with acceptance due to people living nearby. In addition, competing for land use with farming and industry can be avoided. The costs of offshore wind reduce with increasing turbine size as fewer turbines for the same total capacity mean faster installation, fewer foundations and less cabling.

Nevertheless, offshore wind farms also have a downside, as WTs out at the sea are less accessible than onshore WTs. Installation and maintenance are strongly dependent on weather conditions, and travel distances are significantly longer. In consequence, more reliable WTs that need less maintenance are needed to keep the operation and maintenance costs low.

One way to increase reliability of WTs are direct-drive WTs, as gearboxes increase the maintenance need in WTs [9]. The direct-drive WTs mean a low rotational speed for the generator rotor, leading to large generator diameters. Research has shown, that traditional scaling laws of generators cause a faster increase of passive mass, which does not contribute to the power transformation, than active mass [14]. Even adapted design methods taking into account a multi-physics approach show a dominant increase of passive mass [15]. As

a consequence, multiple investigations have been carried out to reduce the passive mass, which is mainly located at the support structure, for different generators with more than 2 MW rated power.

New concepts of generator design for PMSG type machines have been presented, showing potential for mass reduction. One of the concepts removes the attraction forces between stator and rotor by a new arrangement of magnets and coils in a c-core shape [16]. Others investigate the influence of magnetic bearings on the transmission of excitation forces into the generator. The results show that they can reduce the needed stiffness in the generator support structure [17]. Furthermore, new manufacturing techniques like additive manufacturing and their potential for mass reduction were analysed. They showed a potential of up to 39% mass reduction for a 5 MW generator [18].

Besides these more disruptive design approaches, classical optimisation techniques are used to further optimise the state-of-the-art design. Manufacturing oriented approaches develop objective functions for classical optimisers for a 10 MW generator, including estimated material costs and energy conversion losses [19].

Operation oriented approaches consider static and dynamic loading of the generator support structure. These methods remove passive mass in the design, where it is not contributing to structural stiffness [20]. One study analyses the generator behaviour in the frequency domain with modal and harmonic approach [21] to minimise the air gap deflection of the design. Another study presents simplified stiffness models for the structure and the magnetic field to calculate local air gap deflections in the time domain and analyse possible resonances with characteristic excitation frequencies of the WT [22], i.e. the rotational speed and its higher harmonics. To tune the generator design for WTs, natural frequencies of the generator design are adapted using, e.g. stiffeners. An extension of the study takes multiple aspects of air gap deflection, e.g. eccentricity or deformation due to resonance, into account [23]. The extended study shows the importance of considering the forces and deformations for a stiff design that can maintain the air gap. In summary, the actual potential for mass reduction is less when considering the additional factors.

All the listed investigations have in common that they optimise the generator as an isolated system with given external loading. As a consequence, they assume the need for a stiff generator and drive-train design to limit generator eccentricity and avoid EmeIs under the

given external excitations coming from the WT dynamics.

2.1.4. IEA 15MW reference wind turbine

Following the trends of wind energy, the research community has joint forces in the IEA Wind task 37 to develop a reference WT reflecting the design trends [24]. The WT has a rated power of 15 MW, using a direct-drive concept with a PMSG. The WT design is open-access, with a description available on *GitHub*. The model information includes blade, tower, foundation and drive-train parameters that are needed to describe the WT with a state-of-the-art simulation software. A model in the WT simulation tool *OpenFAST* [25] is available in the repository. The present work is based on the version of this WT from April 2022. The parameters of the WT, as used for this work, are listed in Table 2.1. The published open access model uses as suggested controller the *Rosco* controller [26]. The version of this controller, tuned for the monopile reference model, is used throughout the work.

Table 2.1.: WT parameters according to [24] as implemented in the models used in this thesis

Description	Symbol	Value	Unit
Rated power	P_R	15.0	MW
Cut-in wind speed	v_in	3.0	$\frac{\mathrm{m}}{\mathrm{s}}$
Cut-out wind speed	v_out	25.0	$\frac{\mathrm{m}}{\mathrm{s}}$
Rated wind speed	v_N	10.6	$\frac{\mathrm{m}}{\mathrm{s}}$
Hub height	h_H	150.0	m
Rotor diameter	R	240.0	m
Rotor assembly mass	m_RA	274.9	t
Tower mass	m_T	870.5	t
Transition piece mass	m_TP	100.0	t
Monopile mass	m_M	1318.0	t
Rotating drive-train mass	m_rot	151.8	t
Non-rotating drive-train mass	m_stat	523.0	t
Nacelle centre of gravity x	$x_\mathrm{cg,N}$	−4.5	m
Nacelle centre of gravity y	$y_\mathrm{cg,N}$	0.0	m
Nacelle centre of gravity z	$z_\mathrm{cg,N}$	4.1	m
Minimum rotor speed	ω_min	5	rpm
Rated rotor speed	ω_R	7.56	rpm

Furthermore, a Computer aided design (CAD) file in the file format STandard for the Exchange of Product model data (STEP) is available in the repository, which is used to set up a Finite element method (FEM) model of the generator. The generator model is based on the parameters listed in Table 2.2, with adapted number of windings per phase N_w and the nominal current per phase I. These changes were necessary as the values given in the report lead to a nominal torque four times higher than the actually needed torque. With these adaptations, the expected nominal torque of 20.5 MNm for rated operating conditions were achieved.

Table 2.2.: Generator parameters according to [24] with adaptations, ensuring a rated torque of 20.5 MNm.

Description	Symbol	Value	Unit
Core length	l_s	2.17	m
Air gap radius	R_δ	5.08	m
Relative permeability	μ_r	1.06	-
Magnets height	h_{PM}	58.39	mm
Air gap length	δ_0	10.00	mm
Magnets width	b_{PM}	127.64	mm
Remanent flux density of magnets	B_r	1.28	T
Pole pitch	τ_p	159.55	mm
Stator winding turns per phase	N_w	2	-
Nominal winding current per phase	I	4525.48	A
Winding current density	J_s	3.39	$\frac{A}{mm^2}$

2.2. Wind turbine modelling

Designing a WT includes multiple steps. Owing to the substantial cost, prototype manufacturing and testing needs to be as purposeful as possible. Thus, most engineering design is done virtually. Before testing a design as a scaled prototype in the lab or full scale out in the field, the design is analysed based on modelling and simulation. This means, the behaviour of the WT during operation under varying environmental conditions is investigated, and the design is adapted if needed.

To simulate the WT behaviour, a description of fluid dynamics, mechanics, controls and

electromagnetic behaviour is required. The software including fluid dynamics, mechanics, and controls is called aero-servo-elastic code. They use the external loads from wind and waves (at offshore sites) as input. Then they calculate the dynamic response of the WT and the load distribution. To govern the power output of the WT, the system is connected to a controller. The controller is adjusting blade pitch angle and generator demanded torque based on the measured rotational speed.

This work focuses on EmeIs, while the fluid dynamics and controls are taken as given. The interested reader is referred to further literature for more detailed explanations about control [27] or fluid dynamics of WTs [6]. The theory and used methods to describe mechanical and electromagnetic systems in WTs are explained in Section 2.2.1 and Section 2.2.2, respectively. For the analysis of EmeIs, the aero-servo-elastic code needs to be coupled with the electromagnetic solver. The aspects of interfacing different physical phenomena in a multi-physical simulation are outlined in Section 2.2.3. Depending on the modelling approaches chosen for the two physical phenomena, the level of detail of the models, the fidelity, can differ. The methods to tackle differences in model fidelity to ensure a consistency in the interface parameters are described in Section 2.2.4. The section closes with the summary of existing simulation software for WT modelling and generator modelling in Section 2.2.5, providing details about the used software in this work.

2.2.1. Mechanical system modelling

Depending on the fidelity of the analysed system, mechanical models are divided into two types of mechanical systems. The first type is called multi-body system. The latter is called FEM system. Their main difference is the number of DoFs taken into account and their focus of investigation. A multi-body system usually has up to 100 DoFs and aims for system understanding, while a FEM model can have up to several million DoFs and seeks to understand the component's internal load distribution.

In the case of the multi-body system, all bodies are assumed to be non-deformable point masses and can only be displaced relative to other bodies. Bodies are connected through joints and force elements. Joints define the DoF between two bodies, deciding about the possible relative movements. Each joint can have zero to six DoF. These are the translational movement in the three directions of space and the rotations around the three axes of space.

Force elements describe the forces acting between two bodies. One simple example of such a multi-body system is the pendulum given in Figure 2.5.

The pendulum consists of two bodies, a point mass m at the bottom and a massless rod. The two are connected to a fixed point in space through a joint with one rotational DoF, shown as a blue dot. The pendulum can rotate around this point in the 2D plane. As a force element, a spiral spring (dark blue) is added, acting between the rod of the pendulum and the connection point in space. The spring has the stiffness c.

Figure 2.5.: Stiff pendulum with massless rod and point mass at the end, having one DoF, rotating around the joint (light blue) and connected with a torsional spring (dark blue) to fixed point in space.

Similar to this very simple example, a WT can be described as a multi-body system with multiple DoFs. The WT is divided into its components, e.g. three blades, one tower and a nacelle, and the local joints and force elements between them are defined. Then the dynamic behaviour of the system can be described based on this description.

In modern WTs, the assumption of non-deformable bodies is not applicable for all components. Especially the rotor blades and the tower should be treated as flexible bodies. In many cases, a FEM representation is used for these components, describing the deformations.

In the case of a FEM system, the component is divided into elements of constant material properties. The boundaries of the elements touch each other. The assembly of all elements is called the FEM mesh. A meshed cube is illustrated in Figure 2.6 (a). At each node of the mesh, the equation of motion needs to be fulfilled locally. Additionally, some material and mesh element specific boundary conditions need to be fulfilled. Each element can deform by stretching, shrinking, bending or twisting, depending on the element type.

In WTs, the rotor blades and the tower are described using Euler-Bernoulli-Beam elements [28]. As shown in Figure 2.6 (b) the meshing in this case only runs along the longest component axis z. Each element can only bend under a bending moment M_b at the end of the element. This discretised description of the flexible tower and blades is included into

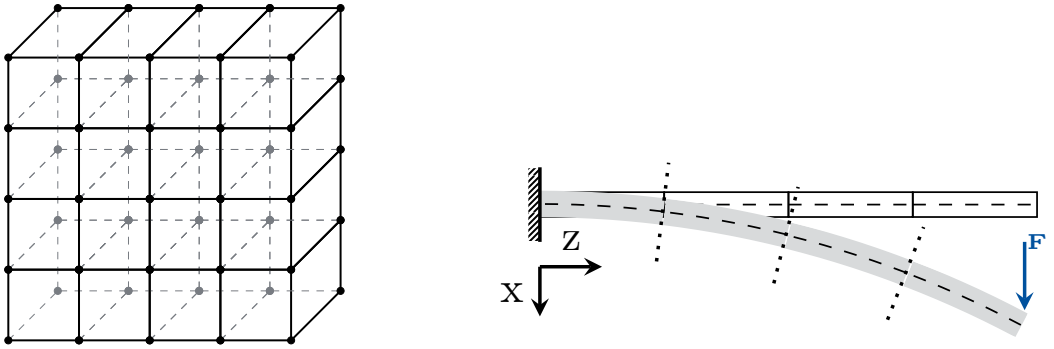

Figure 2.6.: Discretisation (a) of a cube and (b) of a beam

the multi-body system description of the WT as a system. All aspects together populate the system matrices of the equation of motion, which is solved to calculate the system dynamic behaviour. The equation of motion is a differential equation. Analytical solutions to differential equations are not always available and therefore, often numerical solution methods are applied, e.g. the Runge-Kutta method. For further information about the theory of numerical methods, the interested reader is pointed to the literature, e.g. [29, pp. 55-66].

2.2.2. Electromagnetic system modelling

An electromagnetic field can be characterised by the Maxwell equations [30, p. 112]. The equations have to be fulfilled at every point of an electromagnetic field. The basic theory explained in the following is taken from [31, pp. 85-115] if not stated otherwise.

$$B(x) = \mu_0 \frac{N_{\mathrm{w,p}} i}{2\delta(x)} \tag{2.5}$$

The basic principle of electrical machines are rotating electromagnetic fields. Such an electromagnetic field, when created by current, flowing through conductors, can be described by the induction B distributed along a location x that depends on the vacuum magnetic permeability μ_0, the number of windings per pole pair $N_{\mathrm{w,p}}$, the current i through the windings and the local air gap length $\delta(x)$, as given in Equation (2.5). In electrical machines, $B(x)$ has a wave shape that can be approximated using Fourier series by a sum of sinusoidal functions, where the fundamental frequency component is dominant. It has the amplitude

$\hat{B}_1$.

$$B_1(x,t) = \hat{B}_1 \cos\left(\frac{x\pi}{\tau_\mathrm{p}} - \omega t\right) \tag{2.6}$$

In typical modern electrical machines used as generators in WTs, the electromagnetic field is generated by a three-phase winding design, where the three phases' currents are shifted in time by 120 deg. They are rotating synchronously, leading to a joint rotating magnetic field that can be described for each location x and every instant in time t by Equation (2.6) with the pole pitch τ_p and the electrical rotational speed ω.

$$\hat{J_{\mathrm{A},1}} = 2\frac{N_\mathrm{w}\xi_1}{N_\mathrm{p}\tau_\mathrm{p}}\hat{I} \tag{2.7}$$

Due to the distributed windings, the current loading distributes over the circumference of the stator. This distribution of the current over the circumference is expressed by the fictitious quantity of the current layer, assuming a current density at each location. The distribution of the current density J_A is equal to a sinusoidal function with the amplitude of the fundamental wave $\hat{J}_{\mathrm{A},1}$ given in Equation (2.7). It depends on the amplitude of the imprinted current $\hat{I}$, the number of pole pairs N_p, the total number of windings $N_\mathrm{w} = N_\mathrm{w,p}N_\mathrm{p}$ and the winding factor ξ_1.

$$u_\mathrm{co}(x,t) = B_1(x,t) \cdot v \cdot l \tag{2.8}$$

An electromagnetic field moving relative to a conductor with the relative speed v induces a voltage $u_\mathrm{co}(x,t)$ in the conductor of length l, according to Equation (2.8).

$$\hat{U}_\mathrm{ph} = 2\hat{B}_1\frac{\omega\tau_\mathrm{p}}{\pi}lN_\mathrm{ph}\xi_1 \tag{2.9}$$

For a multiphase distributed winding, this sinusoidal voltage results in a peak voltage $\hat{U}_\mathrm{ph}$ per phase, as given in Equation (2.9) with the number of windings per phase N_ph.

$$\hat{\phi}_1 = \frac{2}{\pi}l\tau_\mathrm{p}\hat{B}_1 \tag{2.10}$$

It is common practice to replace the induction with the flux per pole $\hat{\phi}_1$, as given in Equation (2.10).

$$P_{\mathrm{el}} = 3U_{\mathrm{ph}}I_{\mathrm{ph}}\cos\varphi \tag{2.11}$$

When current and voltage appear at the same time in the same conductor or winding, respectively, the product of the two equals the electrical power transmitted through it. For a three-phase electrical machine, the active power output P_{el} can be calculated by Equation (2.11) based on the effective values of voltage U_{ph} and current I_{ph} per phase and the phase angle φ between the two.

$$M = \frac{1}{2}N_{\mathrm{p}}^2\tau_{\mathrm{p}}\hat{J}_{\mathrm{A},1}\hat{\phi}_1\cos\varphi \tag{2.12}$$

Based on Lorenz' law, the conductor with a relative movement to the electromagnetic field also experiences a force. In the case of an electrical machine, this leads to a radial and a tangential force at the surface of the rotor and stator. The tangential component of the force produces the mechanical torque M of the electrical machine. This torque can be calculated for a three-phase electrical machine by Equation (2.12).

This work focuses on PMSG. For this generator type, the rotor magnetic field is created by permanent magnets attached to the rotor. Windings, carrying current and voltage load, are located only on the stator side. Therefore, the magnetic field of the rotor is independent of current amplitudes but results out of the magnetisation of the permanent magnets. An exemplary full analytical model describing the PMSG is presented in [32]. An analytical description of the radial forces attracting the rotor towards the stator in a PMSG are described in [33, pp. 66-73]. This model will be used in this thesis and is explained in more details in Section 4.2.1.

As introduced at the beginning of this section, the given equations assume that the fundamental sinusoidal wave of the electromagnetic field is the most dominant and higher harmonics can be neglected. A more detailed approach, taking the harmonics into consideration, is given by the FEM similar to the method explained for mechanical solvers. The governing equations for the electromagnetic field are the Maxwell's equations. The boundary conditions are based on magnetic field potential at the outer system boundaries. For further details on FEM based electrical machine simulations, the interested reader can

consult further literature, e.g. [31].

2.2.3. Multi-physic interactions

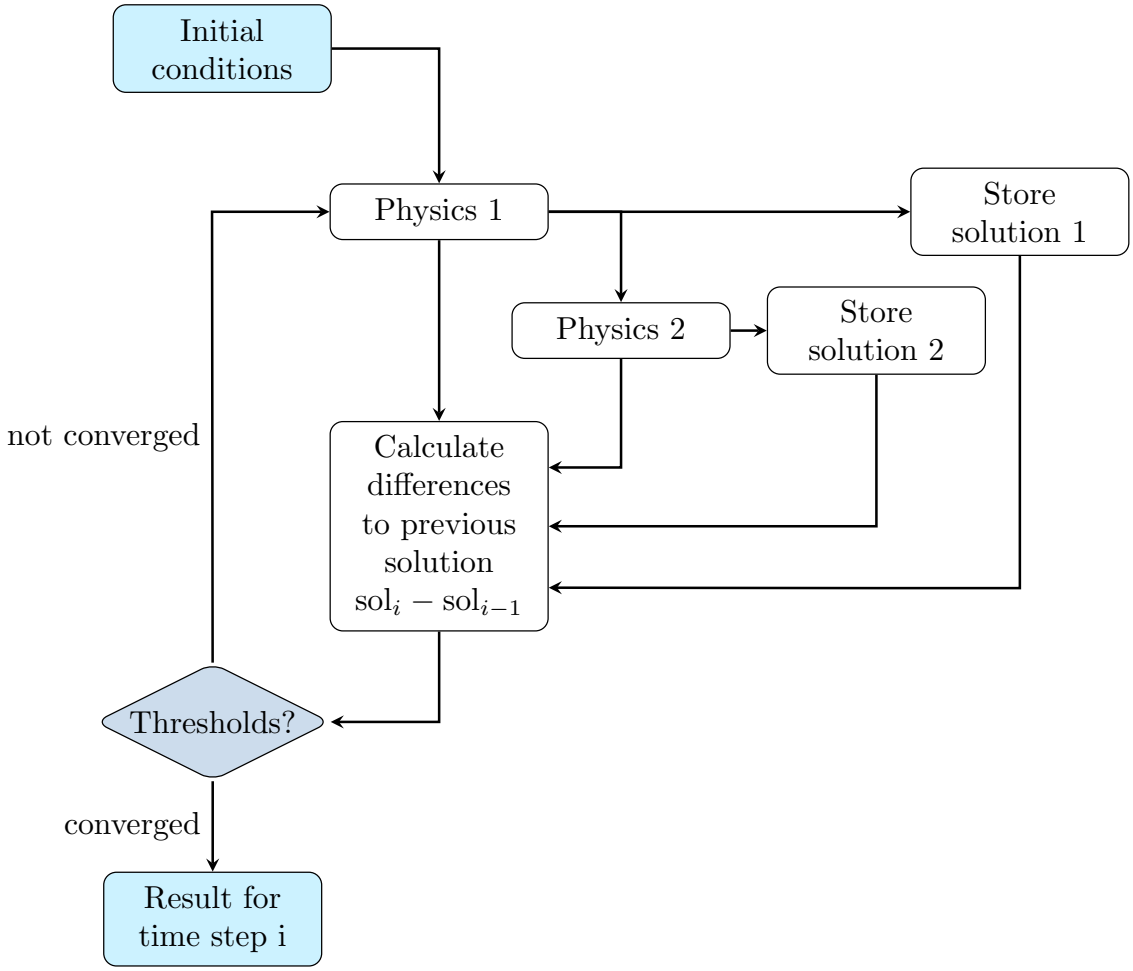

Figure 2.7.: Basic schema of iteration procedure in multi-physical simulations

Connecting the different physical effects acting on a WT, it is important to consider that some system reactions cause feedback from one physical phenomena into another. Therefore, the multi-physical solution normally requires iterations. A basic schema of the iteration is shown in Figure 2.7. In consequence, it means that the equations of Section 2.2.1 and Section 2.2.2 are solved iteratively with changing inputs. This procedure is repeated until the difference of the solutions between two iterations is below a predefined threshold. The threshold is called convergence criteria. When the solutions of the differential equations of both physics fulfil the convergence criteria, the system reaches convergence.

This procedure is generally needed for any interactions of physical phenomena. This includes

the EmeIs as well as the aero-elastic interaction (blade – aerodynamics) and the hydro-elastic interaction (foundation – hydrodynamics).

As the system equations are based on differential equations that usually do not have an analytical solution, numerical solution methods are applied. Numerical time integration solves the differential equations by using incremental time stepping. Therefore, the iterative procedure is used to find a converged solution for every time step. This means, each time step has to fulfil a convergence criterion for all states in the coupled system before the next time step is started.

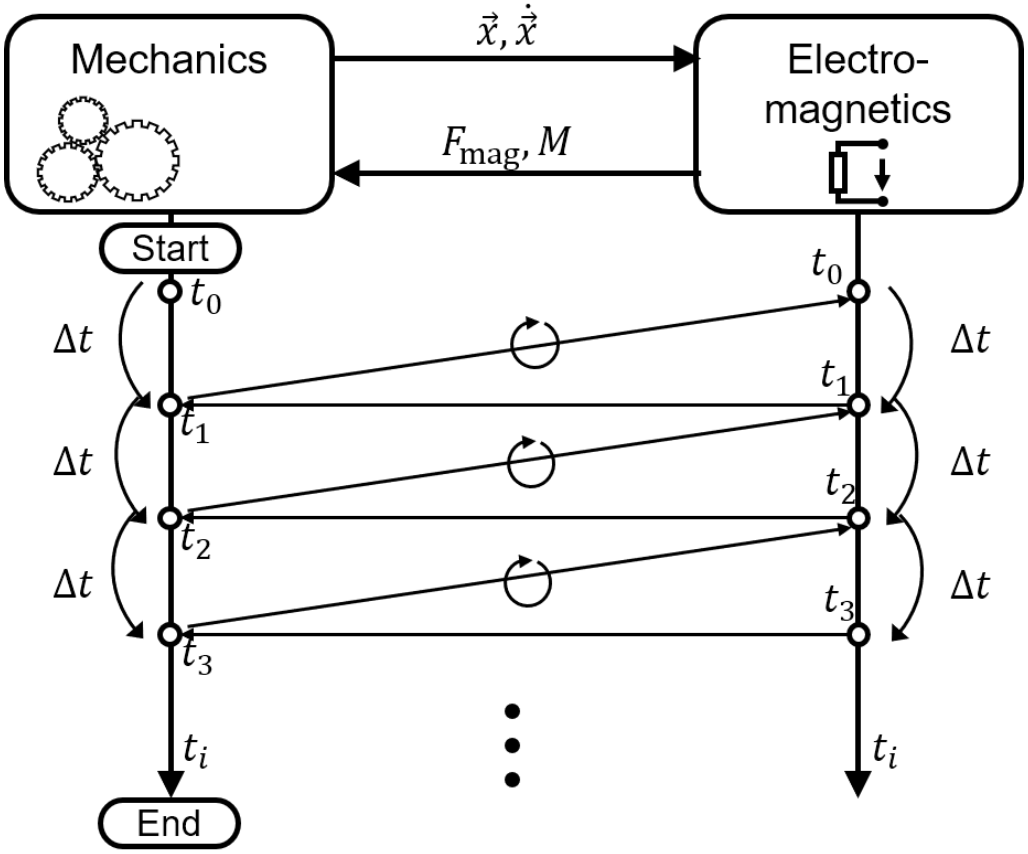

Figure 2.8.: Time integration workflow for coupling scheme [34]

Figure 2.8 shows a schematic representation of the needed workflow for electro-mechanical coupled solutions. The mechanical system starts with the calculation of positions $\vec{x}$ and velocities $\dot{\vec{x}}$ of all bodies in the system. Then, the system states are handed over to the electromagnetic solver. There, the resulting forces F_{emag} and torques M are calculated and returned to the mechanical solver. At the beginning of the simulation, both solvers run a static analysis, to initialise the system. After convergence is reached for the initialisation,

the time integration starts. Now the mechanical solver performs a time integration over a time interval Δt and hands over the resulting states at the end of the time step to the electromagnetic solver. The electromagnetic solver initialises with the states of the last call and solves the time integration to reach the states of the mechanical solver as end states of the time interval. The resulting loads at the end of the time interval are returned to the mechanical solver. If the solution is not converged, the time integration is repeated with the last solution as initial value. When the system reached convergence, the next time step is started.

Looking at Figure 2.8, an additional aspect of coupling can be found. When the mechanical solver starts a new time step, there is no solution of the electromagnetic solver available for the end of the time step. This means, an estimation of the solution is needed until the first run of the electromagnetic solver for this time step. One way to obtain such an estimation is extrapolating the previous solutions. Additionally, this method can help to limit the computational effort, as explained in the following.

Extrapolation: The electromagnetic solver is based on the FEM and therefore is computationally expensive. A similar situation is known from Computational fluid dynamics (CFD) simulations. Research has investigated couplings of fluid and structure frequently in the past [35]. A method used to reduce the computational effort was to reduce the number of communication calls between the solvers. This means, that the Multi-body (MB) solver can compute intermediate results for the system without calling the electromagnetic solver. It is important to notice that this method includes the risk that the solution can be far off due to wrong estimations. This can be corrected with the next communication time step, when the electromagnetic solver is called again. The more the estimation of the extrapolation differs from the new solutions, the more repetitions of the FEM solver calls are needed to reach convergence. In consequence, the length of the communication interval needs to be balanced between reducing the number of intervals and limiting the extrapolation error.

Figure 2.9 illustrates the procedure. Based on the results at former communication intervals, the solution for the next interval is estimated. The estimation is found by fitting an interpolation function with the results and then evaluating this function for future time steps. As fitting functions, constant, linear and cubic functions have been applied. Figure 2.9 compares the different methods to each other and with an example function that represents the exact solution. The constant extrapolation showed good results for small communication

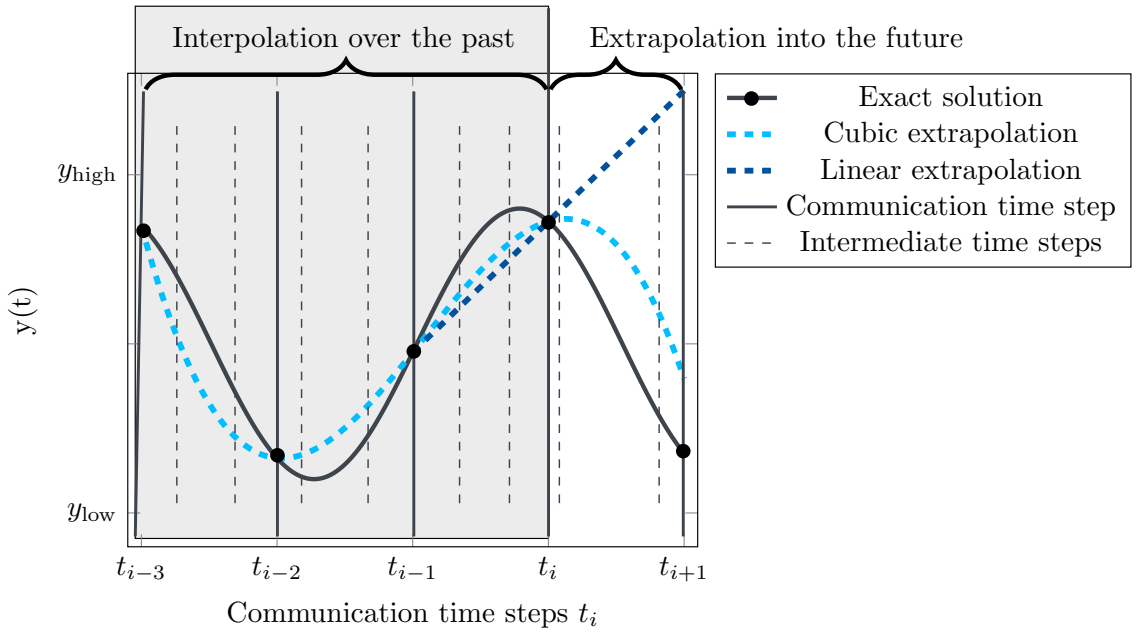

Figure 2.9.: Extrapolation solution for t>0 using linear extrapolation (dark blue, dashed line) or cubic extrapolation (light blue, dashed line) in comparison to the unknown exact solution (solid, grey line) by interpolating over the known solutions at discrete communication time steps t_i (black dots) with $t_i \leq 0$ [34]

intervals. To achieve lager communication intervals and further reduce the computational effort, the other two interpolation options are needed.

The drawback of these two options is the need for former solutions $t_{i-N}...t_{i-1}$. Therefore, they can only be applied after the run of some time steps, i.e. linear after finishing the first communication interval ($N = 1$) and cubic after finishing the first three communication intervals ($N = 3$). To overcome this drawback, the extrapolation method can be adjusted dynamically. This means after initialisation constant extrapolation is used, after the first communication interval linear extrapolation is applied and for the next communication intervals the order of the extrapolation polynomial increases further if wanted. In summary, the extrapolation method solves the issue of unavailable solution data for the mechanical solver. At the same time, a similar issue exists for the electromagnetic solver, when the extended communication intervals are used and interpolation methods are needed.

Interpolation: In this case, the electromagnetic solver needs to solve for intermediate time steps but only has a solution from the mechanical solver for the initial and final states. Therefore, interpolation methods are applied to calculate the intermediate states. Here, step function, linear and spline interpolation have been investigated. Step function and

linear interpolation only need the values at the beginning and end of the time interval. The spline interpolation additionally needs the derivatives of the function at the beginning and end of the interval. This enables a C1-continous function over the whole time integration. Another standard method for interpolation is polynomial interpolation. The drawback with this method is the increased storage need, as such an interpolation would need solutions from former time steps. Therefore, this method has not been used here.

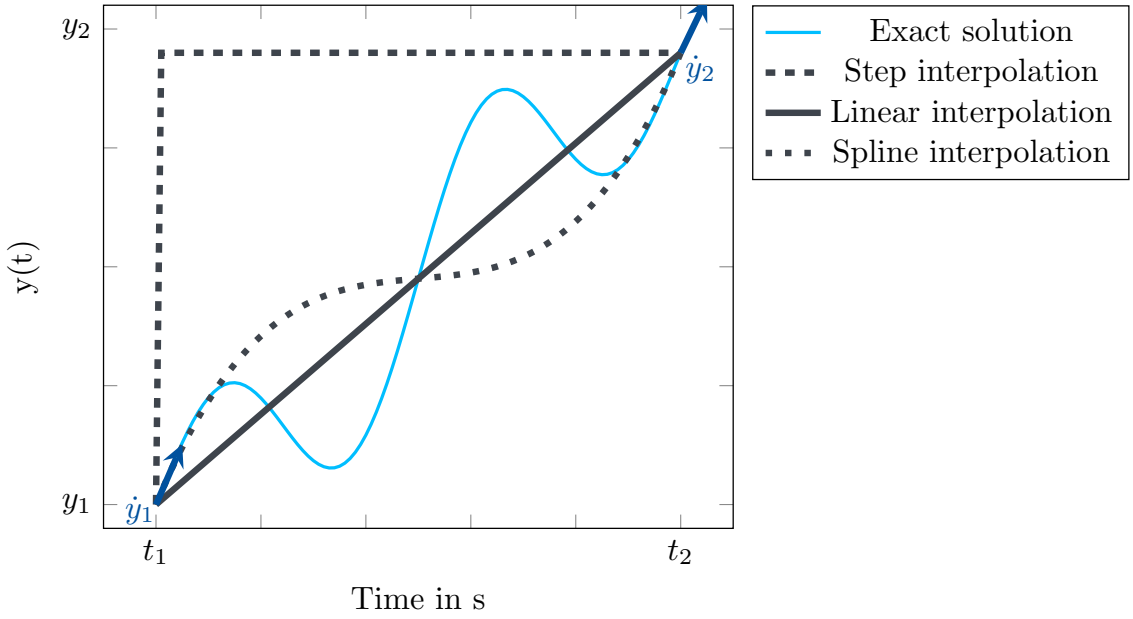

Figure 2.10.: Interpolation of a function between two known solutions at t_1 and t_2 in comparison to the unknown exact function in light blue using step interpolation (dashed line), linear interpolation (solid dark line) or spline interpolation (dotted line) with additional known derivatives $\dot{y}_1$ and $\dot{y}_2$ [34]

Figure 2.10 shows the resulting interpolation results for the investigated methods in comparison to an example function, that is assumed to be the exact solution.

2.2.4. Multi-fidelity interfaces

When coupling the FEM model of the electromagnetic system to the mechanic system modelled as multi-body system, the models are of different fidelity. In the FEM model, the electromagnetic force applies as a surface force to the generator components, as indicated in Figure 2.11 with the small arrows around the circumference. These forces depend on the local air gap δ and increase with decreasing δ. Changes of the local air gap can occur for two reasons: one of the bodies or both are flexible bodies and deform, or in case of rigid bodies they can displace. At the same time, the multi-body system assumes non-deformable

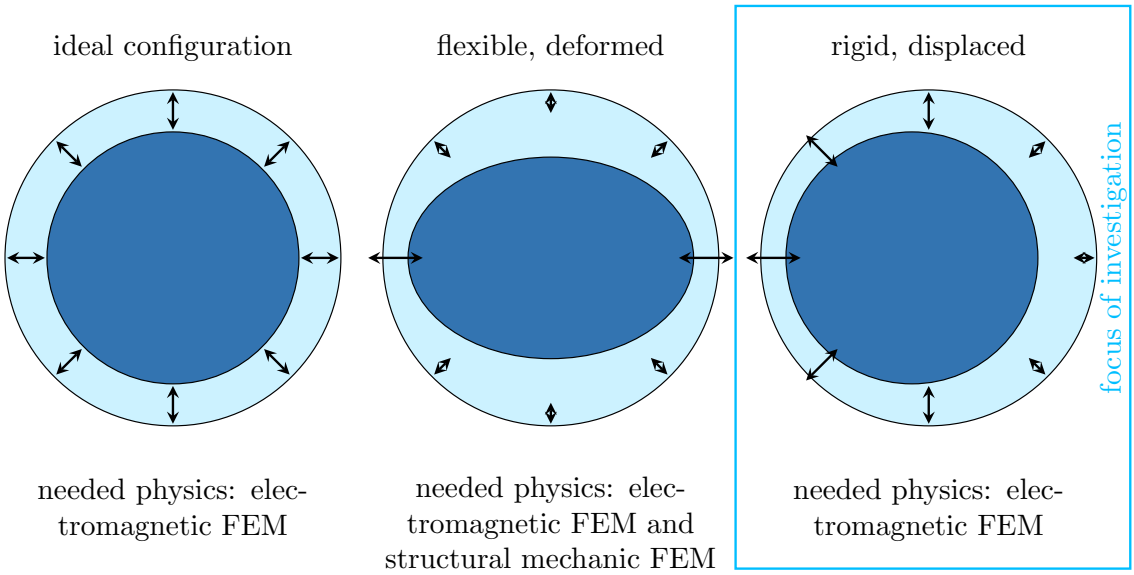

Figure 2.11.: Influences to electromagnetic forces in electrical machines and needed physics for computation. From left to right, the ideal electrical machine, the deformed electrical machine and the displaced or eccentric electrical machine are illustrated.

point masses, connected through joints and force elements. To connect the two solvers, a procedure similar to the one described before in Figure 2.4 is needed. The reduction of the surface forces to one resulting force at the centre of gravity can be transmitted to the mechanical system.

To enable the coupling in the opposite direction, from the mechanical solver to the electromagnetic solver, a moving mesh and a deforming mesh are needed. An illustration is given in Figure 2.12, showing how the mesh elements change their shape and size in case of a displacement of the inner component. The states given by the MB solver are used as input to the moving mesh, relocating the two components relative to each other.

If the components can not be assumed as rigid, a structural analysis needs to be performed together with the electromagnetic analysis before handing over the resulting loads to the MB solver.

2.2.5. Modelling software

The presented methods to model mechanical and electromagnetic systems have been implemented into validated software. These offer a standardised user interface and a quality management to ensure, the implementation of the methods into code are correct.

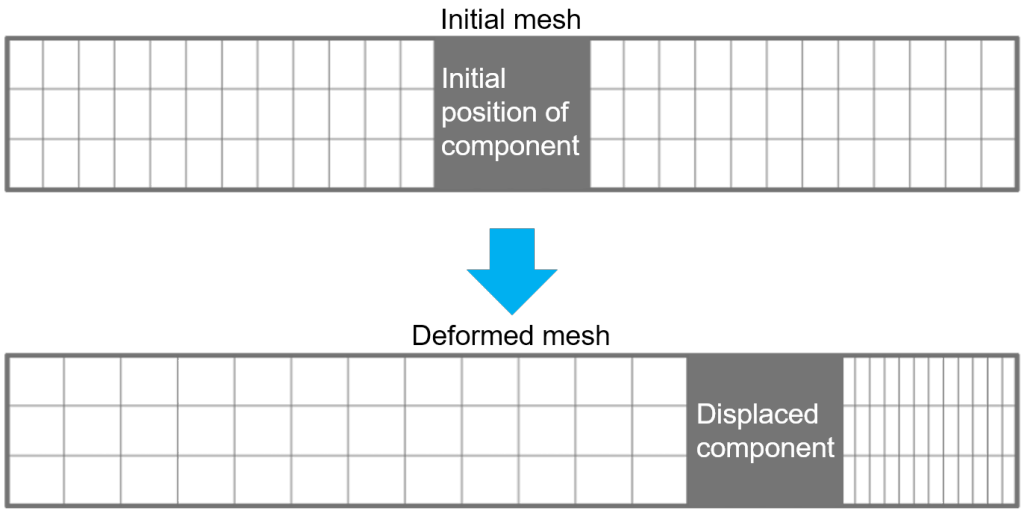

Figure 2.12.: Example for deforming mesh due to a moving part. The upper plot shows the initial mesh. The lower part shows the deformed mesh after moving the gray squared component.

This work uses such software for both, electromagnetic and mechanic system modelling. Examples of broadly used software for the investigated physics are named in the following and the software, used in this work, is explained in more details.

For WT modelling, *OpenFAST*, *Bladed*, *HAWC2* and *Simpack* are the most commonly used software tools. The last three are commercial software, whereas *OpenFAST* is an open source software. In this work *OpenFAST* and *Simpack* are used. Their capabilities and limitations are outlined below.

OpenFAST is an open source software written in *Fortran* and developed by the National Renewable Energy Laboratory (NREL) in the USA. As known from above, the modelling of WTs includes several physical phenomena. *OpenFAST* contains a module for each of the different physics. The main part of the program represents the interface between the physics. This makes *OpenFAST* a multi-physics tool. For the structural representation of the WT, *OpenFAST* offers an Euler-Bernoulli-beam model for blades and tower. Alternatively, the blades can be modelled using the geometrically exact beam theory, increasing their model fidelity. The substructure is modelled using a linear frame finite-element beam model and the Craig-Bampton method. Other than these flexible components, the drive-train is reduced to a multi-body model representing torsional stiffness and damping with a force element and representing the drive-train mass as a point mass with a mass moment of inertia around the axis of rotation of the drive-train. Uniting these components of varying

fidelity makes *OpenFAST* a multi-fidelity tool. The tool populates the system matrices of the equation of motion and solves them using numerical time stepping methods.

Generally, *OpenFAST* is a well documented tool [36] that has proven its validity in many applications, as it is often used in research projects [37]. *OpenFAST* is explicitly designed to model WTs. This has advantages and disadvantages. Setting up a new WT model is easy and straightforward. Only system parameters have to be specified. Thinking about the definition of DoF is not needed. They are all implemented into the software. However, the predefined DoF become a disadvantage when the WT concept to evaluate does not follow the standard configuration of two or three blades on top of one tower, or the research focus intends for a change in fidelity of certain components. In those cases, a high coding effort is needed, to adapt *OpenFAST* to the new application. In consequence, the change to the implementation requires a new validation of the code afterwards. This drawback can be avoided when using *Simpack*.

Simpack is a commercial MB tool, initially developed by the German Aerospace Centre (DLR) and today a part of Dassault Systèmes [38]. *Simpack* allows defining any mechanical system from simple pendulums to trains and cars or WTs. Other than *OpenFAST*, it is a software dedicated to the analysis of one physical phenomena, namely mechanical system dynamics. With the included functionality of flexible bodies as modal representation or beam models, it allows for mechanical multi-fidelity in the models. For WT applications, *Simpack* offers standard interfaces through Force Elements to aerodynamics, hydrodynamics and control, enabling a multi-physical analysis in a co-simulation-like setup. One aerodynamic solver coupled to *Simpack* is the *OpenFAST* submodule *AeroDyn*. Similarly, the coupled hydrodynamic solver is the *OpenFAST* submodule *HydroDyn*. The controller can be included as a dynamic library or through an interface to *Matlab/Simulink*. The solver uses a modal reduction method to solve the equation of motion in a computationally efficient way. The system matrices are populated automatically according to the definitions of bodies (masses), joints and force elements set up by the user. The modal reduction is automated in the solver.

The capability of *Simpack* to model any mechanic system offers a high modelling flexibility. On the one hand, this requires a validation of the kinematic tree of the system for every new model, which can be time-consuming. On the other hand, for an existing model, it is comparably easy and fast to add additional DoF through the graphical user interface

without any coding effort. This also avoids the need to validate the coding implementation of the added DoF as needed with *OpenFAST*.

Besides the capability to include further DoF into the model, additional functionality can be added to *Simpack* using so called *User Routine*s. They offer the possibility to code a user specific force element. This functionality allows interfacing *Simpack* to other solvers and exchange data during simulation runs. This functionality is used to connect *Simpack* to the electromagnetic solver.

For the simulation of electromagnetic systems, a wide range of software is provided, too. These mainly use FEM modelling approaches. Widely used FEM electromagnetic solvers are provided by *Ansys Maxwell*, *Opera* by *Dassault Systèmes* and *Comsol Multiphysics*. All codes mentioned are commercial software. For this work *Comsol Multiphysics* is used.

Comsol Multiphysics is a general purpose multi-physics simulation software provided by *Comsol Multiphysics GmbH*. The software is divided into different modules, such as structural dynamics or electromagnetic fields. The module for electromagnetic simulations offers the analysis of static and dynamic systems. Special submodules for magnetic, electric, electromagnetic and rotating machinery analysis are available. Throughout this thesis, the electromagnetic and the rotating machinery module are used. The static analysis is used for system initialisation of the dynamic analyses. The dynamic analysis is the main focus of this work.

A major benefit of *Comsol Multiphysics* is the ability to run and control *Comsol Multiphysics* models as a *Java* class. This facilitates the interfacing to other simulation software. A dynamic parameter adaptation for the model and the control of simulations is possible without direct access to the solver. This feature is used as complement to the *Simpack User Routine* to couple *Comsol Multiphysics* and *Simpack*.

The implementation of the developed coupling between the software is explained in detail in Chapter 3. The *Comsol Multiphysics* and *Simpack* models to investigate EmeIs in WTs are presented in Chapter 4.

2.3. Literature overview for electro-mechanical wind energy research

To investigate EmeIs in WTs, the different aspects of WT technology and modelling methodology summarised before have to be combined. The interface thereby depends on two major definitions:

- Definition of the system boundaries
- Definition of the model fidelity of the included sub-systems

The decision about the system boundaries and the model fidelity is driven by the research focus and the required computational effort. The modelling determines the interactions that can be represented accurately. The choice of system parameters, in contrast, influences the actually occurring interactions. Research has investigated various combinations of modelling and system boundaries. In the following, the development of the research focus is outlined. The literature is categorised by the system boundary definitions. For each category the model fidelity, the computational effort and the system parameters are discussed.

The smallest system to investigate EmeIs is the electrical machine as an isolated system. In this case, deformations and structural loads are analysed on the mechanical side, and electromagnetic characteristics on the electrical side. These studies are mostly independent of the application of the electrical machine, and neglect excitations from and interactions with any system outside the electrical machine. The main focus of EmeIs here are vibrations resulting out of electromagnetic loads, called unbalanced magnetic pull. In [39] different aspects, causing such vibrations, are categorised into mechanical and electromagnetic sources. They can be summarised to:

- non-uniform air gap distribution due to shape deviations, i.e. manufacturing tolerances and structural deformations (mechanical)
- non-uniform air gap distribution due to axis displacements, i.e. shaft tilting or shifting (mechanical)
- non-uniform magnetic forces due to short circuit or open circuit (electromagnetic)
- non-uniform magnetic forces due to uneven magnetization of material (electromagnetic)
- non-uniform magnetic forces due to asymmetries in the winding topology (electro-

magnetic)

Models to describe the dependence of the electromagnetic characteristics and the mechanical vibrations range from generalised models, describing the global machine behaviour, as in [40–43] to high fidelity FEM models, resolving local effects, found in [44–46]. All these models have in common, that the interface between the mechanical and the electromagnetic side needs to be defined by coupling variables. The coupling variables determine the equations to solve. How these equations are solved depends on the coupling type. In [47] the coupling is divided in constrained coupling, unilateral coupling and full coupling. The solving procedure depends on the type of coupling. The first two solve the system equations of electrical and mechanical side sequentially, whereas the third one solves them simultaneously. Therefore, only the full coupling can represent feedback effects. Based on an exemplary machine, defined in the paper, it is illustrated that the definition of the coupling can influence the type and magnitude of visible self-excited oscillations. It is recommended to consider this when deciding for a coupling method. Besides the definition of the coupling method, the influence of the model fidelity influences the occurring vibrations and loads in the simulation, as shown in [48]. The analysis is conducted on a tilting shaft axis. To avoid 3D FEM models for the electromagnetic system, the electrical machine is reduced to a 2D model. The electrical machine is discretised into multiple slices between one and five. Per slice a 2D model is coupled returning the electromagnetic loads per slice. The higher the number of slices, the more the shaft axis is tilted and displaced in reaction to the calculated unbalanced magnetic forces. Additionally, the varying modelling depth of the mechanical system from a rigid body with deforming bearings up to FEM bodies or their modal representation are investigated comparatively. Especially, the bearing flexibility and the bending DoF of the shaft show a high impact to the calculated system reaction, evaluated based on the air gap distribution over the circumference. At the same time, the computational effort increases with the fidelity of the structure and the number of slices. Therefore, accuracy and computational effort need to be in balance, based on the specific problem. For a tilting shaft the minimum number of slices to be implemented is three, in combination with flexible bearings and a bending shaft, as recommended in [48].

The system design influence to the EmeIs is studied by [49]. It analyses the influence of the shaft stiffness on the machine behaviour and shows that a critical shaft stiffness exists where the system behaviour changes from being stable to unstable. In stable behaviour the air gap

can be maintained, whereas in unstable behaviour the rotor and stator approach each other over time until they clash, as the mechanical forces can not withstand the electromagnetic forces. This study exemplarily highlights the importance of a multi-physical system design for electrical machines.

When shifting the focus to EmeIs in WTs, the system boundary definition extends to account for excitations and possible feedback. Besides the description of the generator as electrical machine, also the WT and the electrical grid maybe of importance in this case. Various research has been conducted in the field of EmeIs in WTs. In general, the research can be divided into four major areas of research focus:

- Grid integration
- Grid interaction
- Wind turbine internal interactions
- Environmental excitations

The first two research areas require a detailed representation of the electrical grid, whereas the last two rely heavily on a detailed description of the WT. Nevertheless, a detailed WT model can be useful for research focused on the grid and vice versa. Historically, the fields of research have emerged in the order as listed above, and the corresponding literature will be outlined based on these categories in the following.

Grid integration: When wind energy was a new and emerging technology, the first question to answer was how to integrate of such variable energy production into the electrical grid without destabilising the grid. Therefore, the oscillations in the power output had to be studied. The level of detail for these studies varies, especially in terms of the WT model. To account for these different approaches, in the following, one representative reference for each of the found approaches is introduced. [50] focusses on the influence of the drive-train design and reduces the mechanical model of the WT to a two mass torsional spring damper. Characteristics from the aerodynamic behaviour or other structural components, e.g. blades, are neglected. Design parameters of the drive-train like its inertia or stiffness are studied. Their influence on the modal system behaviour is investigated. In contrast, [51] focusses on the aerodynamic influences to the power output, reducing the WT to a function of tip speed ratio and power coefficient. Structural properties of the WT are neglected. The resulting

voltage signal is compared to a higher fidelity WT model described in FAST. FAST accounts for the structural and aerodynamic characteristics of a WT, as explained in Section 2.2.5. Differences in the output signal are mainly found for above rated conditions. Another coupling using FAST to describe the WT is introduced by [52]. The grid is modelled with a tool called *RT-Lab*. The tool is proposed to be used for grid connected wind farm control analysis. Here, the focus is put on the ability of the coupling to simulate multiple WTs in parallel, forming a wind farm, with acceptable computational effort. All the introduced models use as coupling variables the rotational speed and the generator torque, and thus can only analyse the interactions between electromagnetic forces and the WT for the torsional DoF. To the best knowledge of the author, studies on the influence of unbalanced magnetic pull to the output signal do not exist on a WT level but only on an electrical machine level.

Grid interaction: After the first experiences with the grid integration of WTs, the focus shifted towards possible contributions of the wind energy to the grid stability. This leads to regulations about fault ride-through capabilities and other requirements for grid connected WT operation. In consequence, the behaviour of the WT under such conditions became of interest and the field of grid interaction research started. This field of research requires a description of the structural properties of the WT and a detailed representation of the electrical grid. The WT models range from a reduced model, focusing on the drive-train, e.g. [53], to a detailed multi-body representation in FAST, e.g. [54]. Thereby, the analysis of WT component loading is most interesting. [55] shows the influence of a voltage dip to the tower vibrations. A longer duration of the voltage dip significantly increases the excitation of Side-to-side (SS) vibrations. In [56] the increased loads of the gearbox bearings under grid and converter faults are demonstrated. Due to the general trend of increased loads in the WT components during grid or converter faults, potential design adaptations avoiding or reducing the loads are investigated. Special power electronics named unified power quality conditioner are tested in [57] and show promising results in load reductions. The impact of the torsional drive-train design parameters is analysed in [53]. The occurring level of oscillations of power output and rotational speed shows a sensitivity to the components' inertia, the shaft torsional stiffness and the shaft torsional damping. Additionally, a controller specifically tuned to reduce oscillations under voltage dip is developed. The importance of the model fidelity to the visible interactions is underlined by the study in [58]. The determined component loads are significantly higher, when using a detailed WT model. A

common characteristic of the studies presented is that only the torsional DoF is used as the coupling DoF.

Wind turbine internal interactions: With the further development of the wind energy technology and the increasing share in energy production, the importance of the reliability of the WTs increased. This opened another area of research, looking closer into the interactions of the WT sub-systems, i.e. controller, structural WT behaviour and electromagnetic behaviour of the generator. This research field usually does not take into account a detailed model of the grid. The fidelity of the coupled models for WT and generator varies significantly from study to study. One of the high fidelity examples is a multi-body representation of the WT using FAST, coupled to a FEM model in Ansys Maxwell to describe the electromagnetic field in the generator, as introduced in [59]. Others model the generator without resolving local effects, as presented in [60] coupling FAST with a combined model of electrical machine and grid in *Matlab/Simulink*. For these couplings, the computational effort ranges from real-time capability as presented in [61] to simulation times of a couple of hours per simulated second for the high fidelity couplings. [62] outlines the changes of the first natural frequency of the drive-train with different model fidelities. The natural frequency is shifted to lower frequencies with increasing fidelity, implying that an increase of the drive-train model fidelity can be of importance to the system design due to possible resonances. The impact to the main bearing fatigue is investigated in [63] showing an increase of up to 15 % in fatigue when including EmeIs. Similar conclusions are drawn in [64] pointing to a general increase of bearing loads under EmeIs. In [65] the WT controller influences on the vibrations, transmitted between mechanical and electrical side in the drive-train, has been analysed using the model developed in [66]. The controller design then is optimised to reduce the torsional vibrations, especially considering grid disturbance events. In [67] an active torsional damping strategy is investigated to reduce the drive-train vibrations. The analysis shows that the damping strategy is able to damp mechanical vibrations but with an increase of electrical component loading at the same time. In conclusion, a more system oriented design approach can be beneficial, as optimising each component separately may not lead to an optimal system behaviour.

The models and analysis introduced so far have focused on a coupling of the torsional DoF. Studies including also the transversal DoFs in the generator show a significant increase in computational effort and the need for model adaptations, as most available WT modelling

software do not include these DoF by default. Therefore, [68] models only the electrical machine to reduce the computational effort, using rotor assembly loads as input at the connection point to the hub. The generator was sliced along its axis of rotation, and 2D FEM generator models were coupled with each slice. Mechanically, the generator is modelled as a multi-body system in *Simpack* (see Section 2.2.5). The two models are coupled using co-simulation methods. The generator is simulated in normal power production operation conditions of a WT. The results show a significant increase in radial displacements, when including the electromagnetic forces, and consequently the bearing forces increase too. This increase in bearing loads of about 30 % is very significant for the design. Nevertheless, interactions with the whole WT can not be studied with the presented model. Therefore, [69] introduces an electro-mechanical model where the generator radial loads obtained from FEM are linearised and simplified to a function of the displacement giving the attraction force between rotor and stator. Similarly, the bearings are modelled as linear springs with a representative stiffness calculated with *Bearinx* [70]. In this study, the unbalanced magnetic forces increase the determined generator eccentricity. At the same time and in contrast to [48], the number of slices used to model the generator does not show significant influence on the results. This supports the assumption that the generator design and the DoFs included in the model determine, whether the number of slices of the generator plays a role or not. It is assumed, that the number of slices in the generator can be reduced to one, when the tilting DoF is neglected or the ratio of diameter to length of the generator is high.

A third way to reduce the computational effort to simulate a complete WT with EmeIs that includes also the transversal DoF is presented in [71]. There, the electromagnetic forces per pole pair are calculated for different air gap length and rotational speeds using a FEM model. The derived value pairs of air gap length, rotational speed and forces are combined into a look-up table, which is used as input to the WT model. The MB model of the generator calculates the air gap length around the circumference for each pole and determines the forces from the lookup table and applies them at the locations of the poles. The application of the forces per pole pair avoids both: the reduction of the electromagnetic forces to global machine behaviour, acting at the machine centre, and the FEM discretisation of the machine. This means that the distribution of the forces along the circumference can be kept, but the computational effort can be limited. In consequence, the resulting structural deformations of the flexible body of the generator can be calculated. Though, feedback of this deformation

that may influence the actual electromagnetic force is neglected. This model can be used to determine the acoustic behaviour of the investigated WT in operation, including the sound excited by the electromagnetic forces, as proven in [72–74].

So far, two conclusions can be drawn from the introduced research. First, the RQ decides about the needed coupling interface. And second, EmeIs in WTs significantly influence the dynamic loading of drive-train components.

Environmental excitations: Besides the interaction of the sub-systems also first investigations of the influence of environmental conditions like wind inflow were analysed, e.g. in [67]. Nevertheless, for studies on EmeIs it was not the focus. However, with the introduction of floating WTs, this field gained of interest. Onshore WTs experienced environmental loading such as the wind induced loads. Going offshore, hydrodynamic excitations from wave and sea current have to be added. For floating WTs, the floater motion and mooring lines' loading add additional dynamics to the system. Therefore, the computational effort, to compute the dynamic behaviour of a floating WT, even without EmeIs is higher than for onshore or offshore bottom fixed WTs. In consequence, the investigations of EmeIs in floating WTs use a two-step approach [75–77]. This means, they first calculate the dynamic behaviour of the whole WT, neglecting the EmeIs. From these results, the loads, accelerations, velocities, and positions at the system boundaries to the drive-train are extracted. Usually these are the loads at the shaft connection to the hub and the tower top motions interfacing the nacelle yaw system. Then in the second step, the EmeIs inside the drive-train are determined with a detailed mechanical model of the drive-train coupled to the generator's electromagnetic behaviour, as in [78]. A fully coupled electro-mechanical WT model is set up in *Simpack* for an onshore WT. Additionally, a *HAWC2* model without electro-mechanical coupling is implemented. The two model responses are compared based on pitch activity and generator torque. Mean values of the two measures are compared, and differences are found to be below 15 % for mean pitch angle and below 10 % for mean generator torque. Additionally, the torque variation relative to the nominal torque is below 0.5 %. From the results, it is concluded in that study, that the radial displacements are too small to cause feedback effects to the WT behaviour. Therefore, the chosen two-step approach is assumed to be valid for that study.

With this two-step approach, [75] shows a significant increase of the main bearing loading due to the floater dynamics, which can be reduced by an adaptation of the main bearing

concept. Similar conclusions are drawn in [77], where the results showed an increase of fatigue in the main bearings due to the floater dynamics and the influence of the floater type on fatigue is determined. [76] analyses how the structural design of the generator support structure and the Bearing stiffness (BS) interact with the floater dynamics. It is found that the BS and the support structure require a minimum stiffness to ensure a maximum local air gap reduction of 10 % during operation. This comes with additional tower top masses and costs due to higher manufacturing tolerance requirements. Additionally, it is shown, that the stiffer bearings can lead to unfavourable system behaviour. A second approach of system redesign is suggested by increasing the nominal air gap length. Here, the main drawback is the higher costs for permanent magnets, as they need higher magnetisation to compensate the increase of air gap length and to achieve the same nominal torque as the initial design. As a third approach, limiting the tower top acceleration through the floater design is suggested, which may increase the floater costs. These conflicting interests underline the necessity of a multi-physical system design approach to achieve a reliable and cost-effective WT design. The suggestion of limiting the tower top acceleration, that has become a common practice for floating WT designs, is questioned in [79]. Possible dependencies between nacelle acceleration and bearing loads are investigated, but only weak correlations are found. This supports further the assumption that a system design approach is recommended.

2.4. Conclusions from literature review and research questions

The outlined literature overview has shown that EmeIs have been investigated with changing research focus and system boundaries. The combinations of focus and boundaries, which are explained in detail in Section 2.3, are summarised in Figure 2.13. For new RQs, two aspects have to be considered when deciding about the needed system boundaries. First, the coupling method has to be chosen. Second, the fidelities of the component models of WT and generator have to be specified.

The available coupling methods can be divided into constrained coupling, unilateral coupling and full coupling. Only the full coupling allows for investigations of feedback effects between mechanical and electrical side. Additionally, the coupling method is connected with the definition of the interface variables. In the case of the EmeIs, these are the air gap

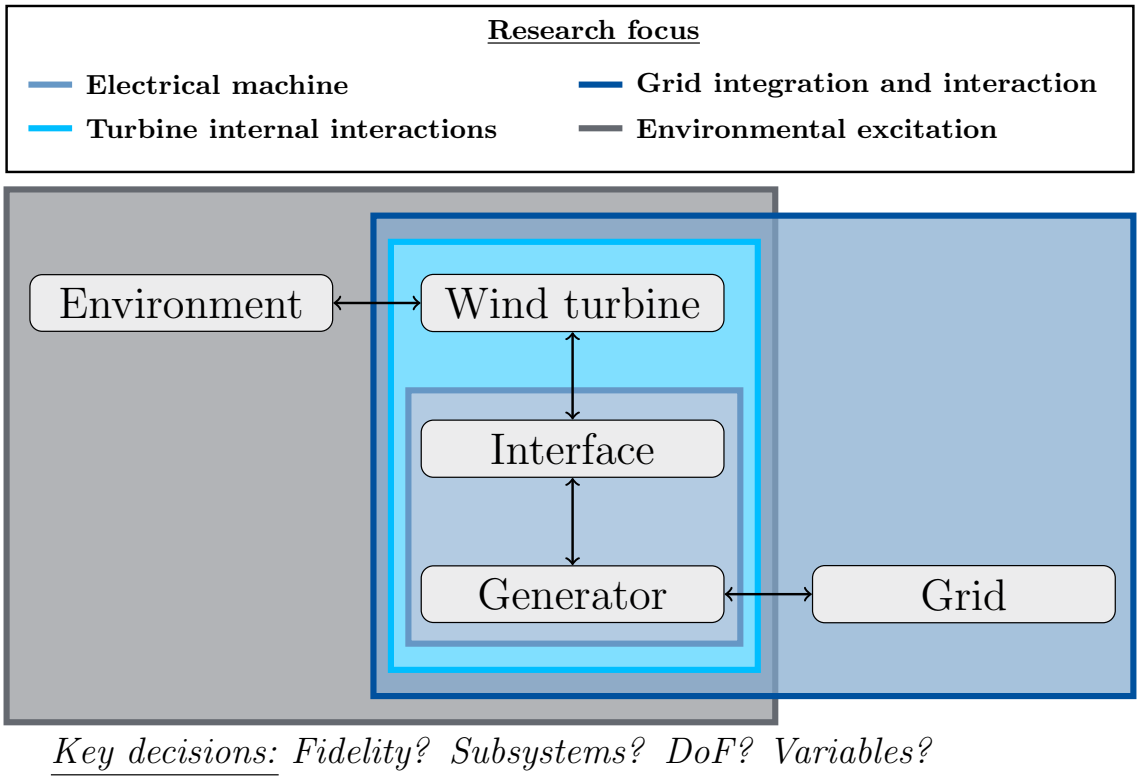

Figure 2.13.: Graphical literature summary of research areas with their included subsystems and the key decisions to take for each of the included subsystems.

distribution along the generator circumference due to displacements and deformations on the mechanical side and the electromagnetic loads acting on the generator components on the electromagnetic side. The possible displacements and deformations depend on the DoF included. Here, the coupling methods connect to the model fidelity, as the available DoFs depend on it. Two types of DoFs exist, inside one body, leading to deformations and between two bodies, leading to displacements. Deformations can only be taken into account when the generator structure is modelled as a flexible body. Displacements are rigid body movements and can vary from one to six DoF. In most literature, only the rotational DoF of the generator is included. In this case, the interface variables are limited to the rotational speed of the generator and the resulting generator torque. Nevertheless, investigations including up to six DoF were found in literature. In that case also descriptions of the bearings are needed. Similar to the mechanical side, the interface variables of the electromagnetic side depend on the model fidelity. The loads can be fed back as resulting loads at the centre of the rotor and stator, e.g. the resulting generator torque, or distributed over the surface, e.g. local forces at each pole. For the first option, a global description of the generator behaviour is sufficient. The latter requires a higher fidelity. The highest fidelity is achieved

using FEM to solve the electromagnetic field distribution in the generator.

Many combinations of component model fidelity have been found in literature. The influence of the fidelity to the visible interactions has been outlined. Three major takeaways are:

- The natural frequencies, especially of the drive-train, can change.
- The determined load distributions in surrounding components, e.g. bearings, can change and usually results in an increase.
- The needed model fidelity strongly depends on the research focus and the system design.

With respect to the required model fidelity, the conclusion found in [78] that the two-step calculation procedure for floating WTs is sufficient can be seen critically. The investigation was based on one system design of an onshore WT. It is expected that further studies are needed to revisit this assumption. When moving offshore, the number of DoFs increase due to the foundation, and it needs to be checked if system resonances can occur that impact the controller behaviour. Additionally, the system parameters like BS should be varied to confirm that shifts of natural frequencies in those cases still keep deviations of the controller behaviour small. Furthermore, the assumption that the controller behaviour can be used to evaluate the impact to the system is questioned as, component loading can be impacted without any controller reaction. Other literature, investigating the system parameters, has shown significant influence. Especially, the BS, the torsional spring damper properties of the drive-train and the chosen control strategy can impact the oscillations and load levels. Additionally, it was shown that uncoupled design optimisation can lead to unfavourable interactions.

All in all, the literature proves the importance of EmeIs in WTs and the need for multi-physical analysis and system design. Most of the literature focuses on the impact of EmeIs to the directly connected components, i.e. the power output of the generator or the mechanical loading of drive-train components like the main bearings or the shaft. Investigations on components' loading, e.g. tower or blades, were carried out only for grid fault conditions. An analysis of possible interactions with the aerodynamics of the WT has not been found.

At the same time, highly reliable, direct-drive offshore wind turbines with increasing rated power using PMSG generators are seen as a development trend. Due to the scaling laws

of the generator, this growth increases the tower top mass, which leads to an increase of tower and foundation cost. Generators of 10 MW and higher have a diameter of 10 m and more and weigh more than 300 t. Currently, it is assumed that EmeIs due to transversal displacements in the generator leading to non-uniform air gaps can be neglected for global system analysis. This is based on the current design approaches using conservatively stiff design parameter limits that require a high share of support structure mass. To reduce the drive-train mass, these design assumptions need to be re-evaluated. Design adaptations of the generator and the drive-train, applying lightweight design methods, are sought. These adaptations require models, which consider multi-physical interactions, especially for EmeIs, to account for changes of the modal system properties, and increasing interactions and avoid resonances or other excitations. In contrast to literature, which provides a deep understanding of the *local* system response, a more profound understanding of the *global* system behaviour, including EmeIs, is needed. This allows to concentrate the modelling on relevant interactions with minimal computational effort. To gain this better understanding of the global system behaviour due to EmeIs and find a representative model, three RQs are investigated in the present work:

- **RQ1:** Can electro-mechanical interactions have an impact on the aerodynamics of the wind turbine?
- **RQ2:** Can electro-mechanical interactions increase load levels outside the drive-train?
- **RQ3:** What is the needed model fidelity to represent the electro-mechanical interactions with limited computational effort?

To enable a more generalised answer to the three questions, the system parameters will be varied to find the design limits from a systems engineering point. The ultimate design limit is reached when stator and rotor touch, causing a magnetic short circuit. The system parameters to be studied are the BS and the assembly tolerance, responsible for the constant eccentricity. The WT will be modelled as a multi-body system with flexible blades and tower. The generator will be modelled with two fidelity levels: a quasi-static analytical model capturing the function of radial attraction force, depending on the air gap distribution, and a FEM model that includes local and transient effects. The coupling will only take into account the transversal DoF of the generator in radial direction. Axial movements will not be considered. As the torsional coupling has been studied extensively in the literature,

it is excluded in this study. Furthermore, shaft tilting will be excluded, and the shaft is assumed to be rigid, which means neglecting bending in the shaft. Therefore, the analysis focuses on the transversal DoF, which facilitates the understanding of its influence on the system behaviour. The reference WT described in Section 2.1.4 will be used. To limit the computational effort, hydrodynamic loads will be neglected. This thesis aims to contribute to the development of a multi-physical design approach, enabling mass reduction of the drive-train in the future and extend the WT design limits needed for turbine growth.

Chapter 3

Electro-mechanical two-way software coupling

The analysis of EmeIs in WTs is an interdisciplinary task. The state-of-the-art in Chapter 2 shows that first steps towards coupled analyses have been taken. However, the existing couplings are specific developments and need significant adaptations when dealing with generalised problems. For a generic analysis of EmeIs in WTs with their generators, a different software coupling is needed. Such a generalised coupling is presented in this section. If not stated otherwise, the content of this chapter is based on the author's publication in [34]. First, the workflow and implementation of the coupling are explained in Section 3.1, followed by the validation in Section 3.2.

3.1. Workflow and Implementation

As outlined in Section 2.1.2, electromagnetic forces are a function of the air gap distribution in the generator, non-linearly increasing with decreasing air gap length. In WT generators of 10 m diameter, δ is in the range of 10 mm [24, p. 29] and small changes of δ result in significant changes of F_{emag}. Therefore, a strong two-way coupling to determine the generator displacement and the resulting electromagnetic forces is needed. The basic workflow and its implementation are explained in Section 2.2.3 and Section 2.2.4. Further details are provided in the following. As this coupling focuses on the coupling of the

electromagnetic and the MB solver, all bodies in the following are assumed to be rigid. The

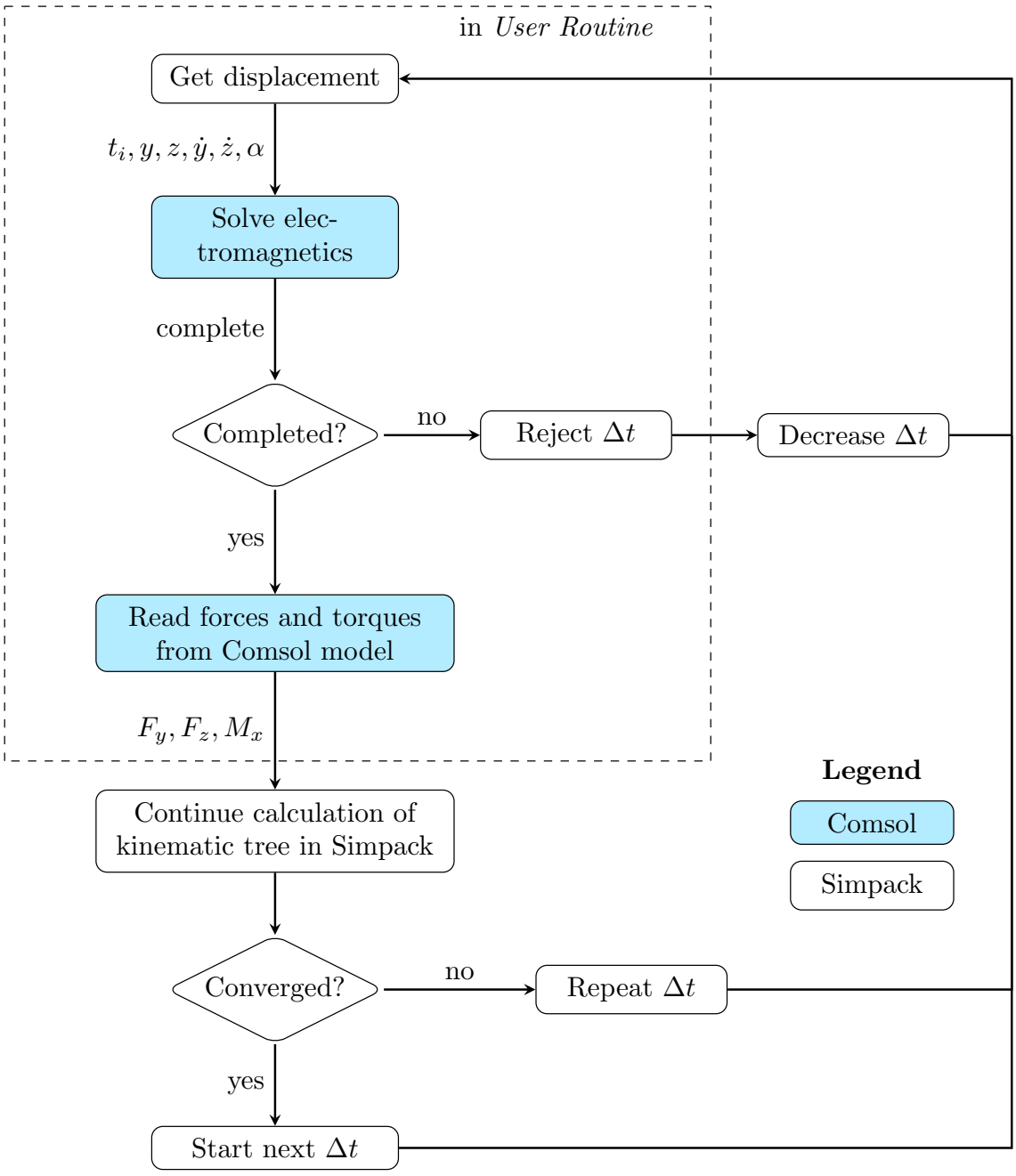

Figure 3.1.: Flow chart of the implementation of the software interface between *Simpack* and *Comsol Multiphysics* [34]

described workflow generally works with any MB and electromagnetic FEM solver. Here, *Simpack* has been used as MB solver. It offers to include so-called *User Routine*s, which allow the user to code customised functionalities into a model using *C* as coding language. *Comsol Multiphysics* has been used as electromagnetic solver. It is a commonly used solver in research in the field of electromagnetism and allows the user to script the simulation steps

in *Java* by loading the model as a *Java* class. The implementation of the workflow with these two software programs is shown in Figure 3.1. *Simpack* is implemented to take over the lead during simulation. This means, it controls the time integration by checking the convergence of the results. The coupling to *Comsol Multiphysics* is achieved with a *User Routine*. For communication, *Java Native Interface (JNI)* is used between the *User Routine C* code and the *Java* class of the *Comsol Multiphysics* model. At every call of *Comsol Multiphysics*, it checks for convergence of the electromagnetic solver. An integer that is returned from the *Java* class to the *User Routine* indicates, whether *Comsol Multiphysics* could converge for this time step. When convergence failed on the *Comsol Multiphysics* side, *Simpack* tries to reduce the time step and repeat the time interval. When this is not possible, the coupled simulation stops.

Inside the *User Routine*, *Simpack* hands over the needed inputs to *Comsol Multiphysics*. This includes the current simulation time t_i and the positions y and z of the moving body with the corresponding velocities $\dot{y}$ and $\dot{z}$. For rotating bodies, the angular position α is included too. If the solution from the electromagnetic solver run converged, the *User Routine* reads the forces F_y and F_z, and the torque M_x, acting on the moving body, from the *Java* class. The *User Routine* passes the forces on to the MB solver, which checks for convergence of the mechanical solution and continues the simulation run accordingly.

Simpack uses flexible time steps and dynamically decreases the time step, when convergence is poor. This can lead to a significant increase of computed time steps. However, *Comsol Multiphysics* is computationally very expensive, and simulation runs need to be limited. Therefore, interpolation and extrapolation methods are implemented as explained in Section 2.2.3 and a fixed communication interval is introduced.

The step function showed the need of very small communication intervals and was discarded. The instability of the step function can be explained by the discontinuity it causes at the step time to the electromagnetic solver. The other two interpolation schemes showed good stability and can be selected by a user input flag. Similarly, for extrapolation, the degree of the final polynomial can be defined with a user input flag in the coupling.

The calculation of interpolated and extrapolated values based on stored solutions is implemented into the *Java* Class. In consequence, the workflow shown in Figure 3.1 is not affected. *Simpack* only hands over an additional boolean value, indicating whether the function call

happens at a communication time step or at an intermediate time step. Depending on the boolean input from the *User Routine*, the *Java* Class switches between extrapolation or a new *Comsol Multiphysics* simulation run.

3.2. Validation of the generalised electro-mechanical coupling

Before applying the introduced software coupling for detailed WT simulations, the implementation needs to be validated. The following subsections explain the validation set up (Section 3.2.1), the performed measurements (Section 3.2.2), and the numerical simulations (Section 3.2.3) and discuss their comparison (Section 3.2.4 and Section 3.2.5).

3.2.1. Validation example

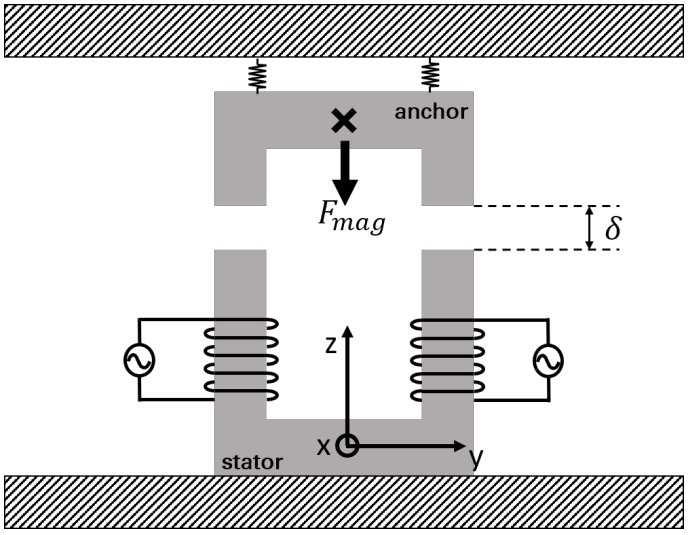

Figure 3.2.: Sketch of the test set up needed for the validation of the implemented interface [34]

For the validation of the coupling, a well known example from literature for electromagnetism is adapted to set up an electro-mechanical system. The system consists of two U-shaped iron cores, being a small air gap apart from each other, with one core passing through coils (stator). The core not passing through a coil is hung on two springs (anchor). A sketch of the idealised system is shown in Figure 3.2. The general behaviour of this system can be estimated from physical understanding and the set-up is easy to build and measure, which is beneficial for the validation.

The electromagnetic attraction force F_{emag} through the air gap δ follows Equation (2.4) and

acts as an excitation force in the system. Assuming that the iron cores are rigid and moving, the mechanical behaviour can be described by the equation of motion for the undamped system, as given in Equation (3.1) with the acceleration $\ddot{z}$ of the suspended mass m, the total stiffness of the spring c and the position of the suspended core z.

$$m\ddot{z} + cz = F_{\text{emag}} = F\left(\frac{1}{z^2}\right) \tag{3.1}$$

The system can be excited with direct or alternating current in the coils, leading to a constant or alternating attraction force between the two iron cores. The measurement equipment will be explained in the next subsection.

3.2.2. Experimental set up

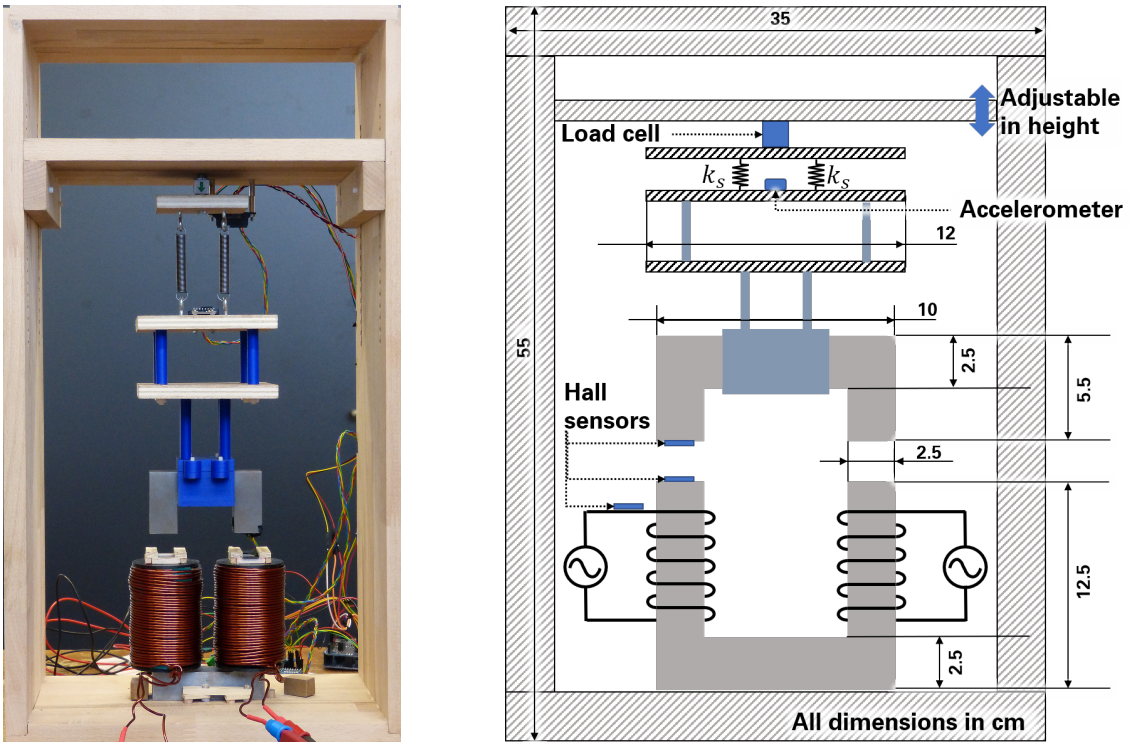

(a) **(b)**

Figure 3.3.: Illustration of the built test bench, showing a picture in (a) and a principle drawing with the relevant dimensions in (b); additionally, the measurement sensors are marked in (b)

A test bench according to the test case was built and equipped with measurement devices. The setup is shown in Figure 3.3 (a). Figure 3.3 (b) provides more detailed information on

the dimensions of the test bench. To enable different initial air gap lengths δ, the upper wooden plate, the suspension is connected to, is height-adjustable.

As the springs that have been used are made out of metal, they need to be kept out of the influential area of the magnetic field. Therefore, the setup was modified compared to the idealised system in Section 3.2.1, and a suspension was included, which is made of wood and 3D-printed plastics. The wooden plates introduce an aerodynamic drag force F_D in the system, due to their horizontally hanging area A. The aerodynamic force follows Equation (3.2) with the air density ϱ and the drag coefficient c_D. The drag coefficient for a flat plate perpendicular to the flow varies in literature and a value of 1.11 is assumed here. The air density is set to a value of $1.225\,\mathrm{kg/m^3}$, common in wind energy.

$$F_\mathrm{D} = \frac{1}{2}\rho A c_\mathrm{D} \dot{z}^2 \tag{3.2}$$

This needs to be taken into account for the numerical model too and adapts Equation (3.1) to Equation (3.3). Viscous damping of the springs' material is assumed to be negligible.

$$m\ddot{z} + \frac{1}{2}\rho A c_\mathrm{D} \dot{z}^2 + cz = F_\mathrm{emag} \tag{3.3}$$

To characterise the system behaviour, the test bench was equipped with different sensors. A Hall sensor parallel to the connecting wire measures the surrounding magnetic field and calculates the corresponding imprinted current. Two Hall sensors attached to the iron core legs measure the magnetic flux density at both sides of the air gap. The total force acting on the hanging iron core is measured with a load cell, placed between the springs and the test bench frame. To characterise also the dynamic behaviour, an accelerometer is placed on top of the suspension. All measurement values are logged with an *Arduino Uno*, a microcontroller board for measurement recording with a USB connection. An analogue-digital converter is interposed between the *Arduino Uno* and the load cell, and the Hall sensors. The *Arduino Uno* sampling rate of about 10 ms is an average value. In case, a constant sampling rate is needed, the measured time series needs to be interpolated.

To validate the introduced coupling with the given test bench, a virtual representation of the system is needed. Therefore, the mass of the hanging parts, the stiffness of the springs, and the magnetic material properties of the iron cores have to be determined. The mass is measured with a scale. To characterise the spring stiffness c_S, they are put into a tensile

test bench. All these measurements are repeated three times to account for uncertainties, and the resulting mean values are used in the following. The material properties of the iron core are identified according to IEC 60404-4 [80] and are given in the Appendix A. The derived parameters are given in Table 3.1. With the determined values, the undamped

Parameter	Value
m	$1.11\,\mathrm{kg}$
c	$2 \cdot 480\,\frac{\mathrm{Ns}}{\mathrm{m}}$
c_D	1.11
ρ	$1.225\,\mathrm{kg/m^3}$
A	$0.0144\,\mathrm{m^2}$

Table 3.1.: System parameters of the built test bench

natural frequency of the one-mass-spring-damper-system is given by Equation (3.4).

$$f_0 = \frac{\sqrt{\frac{2c_\mathrm{s}}{m}}}{2\pi} = 4.7\,\mathrm{Hz} \tag{3.4}$$

3.2.3. Numerical set up

For the virtual representation of the test bench, models were set up in *Simpack* and *Comsol Multiphysics*, following the principle drawing of Figure 3.3 (b) for *Simpack* and reducing Figure 3.2 to the electromagnetic components for *Comsol Multiphysics*. The springs are assumed to be linear. The aerodynamic force is modelled using the expression given with Equation (3.2), using the actual velocity of the suspended part in every time step as input. Furthermore, gravity force is acting on the suspended part. The electromagnetic force is included using the new *User Routine* described in Section 3.1. For the mechanical model in *Simpack*, all parts are modelled as three-dimensional bodies with a mass. The DoFs are reduced to movements in z-direction only, as this is the predominant direction of movement in the used test bench. This reduction of model complexity is sufficient for validation, but can be extended to more DoFs in the future if needed, using the same methodology. The electromagnetic model in *Comsol Multiphysics* is reduced to two dimensions, limiting the computational effort needed. The magnetic field formulation is used for the model setup, and the coils are modelled as surface boundary conditions at the core edges. To enable the dynamic movement of the hanging core during transient analysis, a moving mesh and a deforming mesh are included (compare Section 2.2.4).

Furthermore, the solvers' settings need to be chosen. For the MB solver on the *Simpack* side, the "SODASRT 2" was chosen, based on the implicit Backward differentiation formula (BDF) [81]. This is the standard *Simpack* solver, which is considered to be robust and computationally efficient. The electromagnetic FEM solver of the *Comsol Multiphysics* model is the "generalized alpha" solver [82]. It uses a fully coupled formulation with a constant Newton method for numerical damping, which was set to 1 over all iterations. The solver settings are problem dependent. Especially in the case of increasing system complexity, solver settings need to be adapted.

With the chosen solver settings, the next step for the electromagnetic modelling is a mesh convergence study. As the mechanical side considers only the z-direction as DoF, the magnetic attraction force in this direction is chosen as mesh convergence criteria. Additionally, the skewness of the elements as defined in [83] is used as a quality measure. The resulting triangle mesh with 2314 elements has an average element quality of 0.799.

For the robustness and accuracy of a transient analysis, the time step and the convergence tolerance need to match. For *Simpack* and *Comsol Multiphysics*, this reduces to the adjustment of the tolerance, as both software use adaptive time stepping. This means the time step is chosen depending on the user-requested tolerance and automatically increased or decreased. The convergence check in *Simpack* follows Equation (3.5) according to the documentation [38]. $\Delta s_i(t)$ is the effective tolerance of the current value $s_i(t)$ for the i^{th} element in the state vector. The chosen tolerances are included with $\Delta s_{\mathrm{abs},i}$ as absolute tolerance and $\Delta s_{\mathrm{rel},i}$ as relative tolerance. The time step is decreased until the changes of the values $s_i(t)$ are within $\Delta s_i(t)$.

$$\Delta s_i(t) = \Delta s_{\mathrm{abs},i} + |s_i(t)| \Delta s_{\mathrm{rel},i} \tag{3.5}$$

On the *Comsol Multiphysics* side, "scaled tolerance" is used, and the convergence check is done according to Equation (3.6). The scaled tolerance depends on the number of fields N_{F}, counted with j and the DoFs $N_{\mathrm{DoF},j}$ for each field, counted with i. The solver estimates the local absolute error of the scaled solution vector s_i, given with e_{s_i}. $\zeta_{\mathrm{abs},i}$ represents the scaled absolute tolerance criteria and ζ_{rel} the relative tolerance criteria. The time step is converged, if the condition of Equation 3.6 is fulfilled, otherwise the time step is decreased.

$$\sqrt{\frac{1}{N_F}\sum_j \frac{1}{N_{\mathrm{DoF}j}}\sum_i \left(\frac{|e_{s_i}|}{\zeta_{\mathrm{abs},i}+\zeta_{\mathrm{rel}}|s_i|}\right)^2} < 1 \tag{3.6}$$

The tolerances of both models need to be adjusted to each other and with the communication interval, to ensure an overall stable and converged solution. Therefore, a convergence study is performed. In a full factorial study, the tolerances, the communication interval and the methods for interpolation and extrapolation are varied to study the accuracy. The combination of the highest communication interval and the least strict tolerance values is chosen to achieve the highest performance. The resulting, problem specific parameters for the testing example are listed in Table 3.2.

Table 3.2.: List of optimal coupling configuration for investigated example

Investigated criteria	chosen method or value
Simpack tolerance	10^{-4} in general and 10^{-7} for positions
Comsol Multiphysics tolerance	10^{-4}
Communication interval	0.04 s
Interpolation method	spline
Extrapolation method	cubic

3.2.4. Validation cases

To validate the coupling, the system behaviour in static and dynamic cases need to be compared. The static system behaviour is studied with direct current, which is imprinted on the coils. The dynamic system behaviour is analysed by system excitation with alternating current. In addition to the current type, used for system excitation, the current amplitude and the initial air gap between the two iron cores can be varied. For alternating current, the alternating frequency can also be set. To avoid damage due to contact of the two iron cores and at the same time to ensure, that the attraction force is still high enough to excite the system, the current amplitude and the air gap length needed to be adjusted together. As current amplitude I, 2 A and 4 A are chosen. The initial air gap is set to δ_0 =23 mm and 42.5 mm, respectively. The alternating frequency for the dynamic analysis was chosen according to the natural frequency f_0 of the system. The magnetic attraction force has twice the frequency of the exciting alternating current. Hence, to maximise the excitation

of the system, the frequency of the magnetic attraction force should to be close to f_0. As given in Equation (3.4), f_0 is ca. 4.7 Hz. Nevertheless, fatal resonance needs to be avoided. Therefore, the excitation frequency of the force is set to 4 Hz, which results in a current frequency of $f = 2Hz$. The resulting load cases are listed in Table 3.3.

Table 3.3.: Measured validation cases with direct and alternating current, varying current magnitude I and initial air gap length δ_0

Case no.	type	I [A]	f [Hz]	δ_0 [mm]
1	static	2	-	23.0
2	static	2	-	42.5
3	static	4	-	23.0
4	static	4	-	42.5
5	dynamic	2	2	23.0
6	dynamic	2	2	42.5
7	dynamic	3	2	23.0
8	dynamic	4	2	42.5

3.2.5. Validation results

All measurements are initialised with the system in rest and without current. To account for measurement uncertainties, all measurements have been repeated three times. With the uncertainty of the measurement sensors, a tolerance band was calculated following Equation (3.7a) to Equation (3.7c). This procedure is applied to all the results, presented in the following. The measurement uncertainty was calculated to $\Delta_{\text{tol}} = 0.0264 \cdot F_i$.

$$\bar{F} = \text{mean}(F_1, F_2, F_3) \tag{3.7a}$$

$$F_{\text{min}} = \min(F_1 - \Delta_{\text{tol}}, F_2 - \Delta_{\text{tol}}, F_3 - \Delta_{\text{tol}}) \tag{3.7b}$$

$$F_{\text{max}} = \max(F_1 + \Delta_{\text{tol}}, F_2 + \Delta_{\text{tol}}, F_3 + \Delta_{\text{tol}}) \tag{3.7c}$$

Static analysis: For the static analysis, the direct current is ramped up to the target magnitude. During this process, the system behaviour is recorded until the system reached its new steady state. To validate the static system behaviour, the total force acting on the hanging part is used. The measurement results are included into Figure 3.4 as dark grey bars representing the mean value and the error bars showing the uncertainty. The blue bars show the simulation results as direct comparison to the measurement. The mean value of the measurements is compared to the simulation with the relative difference Δ_{rel}, which is

normalised to the mean value of the measurements. For all cases, the relative difference is below 4%, which indicates a good agreement. Additionally, the tolerance band is taken into account. Here, only case 3 exceeds the tolerance band. Case 3 is the case with the maximum magnetic force to the system, with the smallest initial air gap and the highest current magnitude. Errors of the modelling parameters are expected to be most influential here. All others stay within the uncertainty bandwidth and the static behaviour is seen as well captured.

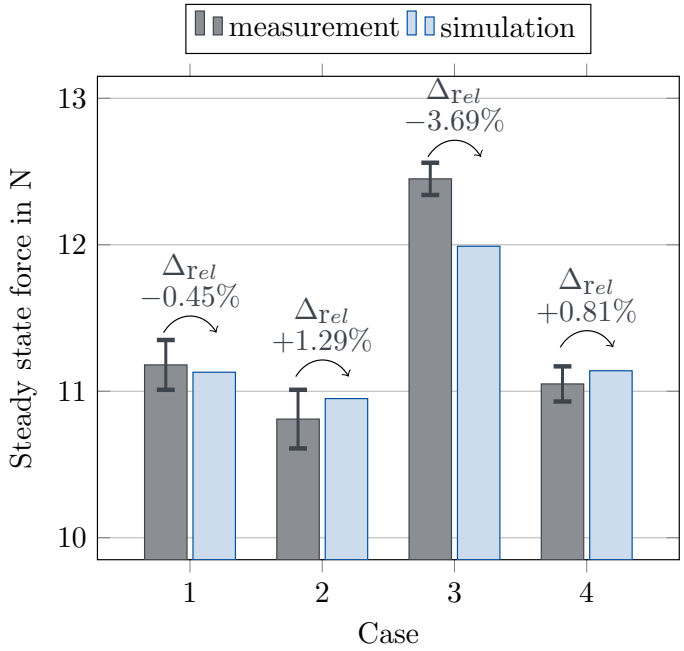

Figure 3.4.: Comparison of steady state force for the static analysis, between measurements and simulation for 4 different load cases, using direct current for system excitation [34]

Dynamic analysis: For the dynamic analysis according to cases 5 to 8 the alternating current is sent through the coils with a sinusoidal curve starting with 0 A at $t = 0$ s. Here, time series are analysed and compared. Therefore, the three measurements are synchronised and linearly interpolated to ensure equidistant time sampling. Then for every time step the mean, minimum, and maximum value from the three measurements are determined. In a first step, the resulting time series are directly compared to the simulation result. In a second step, the spectra of the signals are compared by applying a Fast Fourier Transformation (FFT). In a last step, the cross correlation of the mean measurement signal and the simulation result is determined as a measure of signal similarity. It calculates the correlation factor of two signals for all possible time shifts [84]. The results are shown and discussed in the

following exemplarily for cases 5 and 8. The other two cases are given in Appendix B.

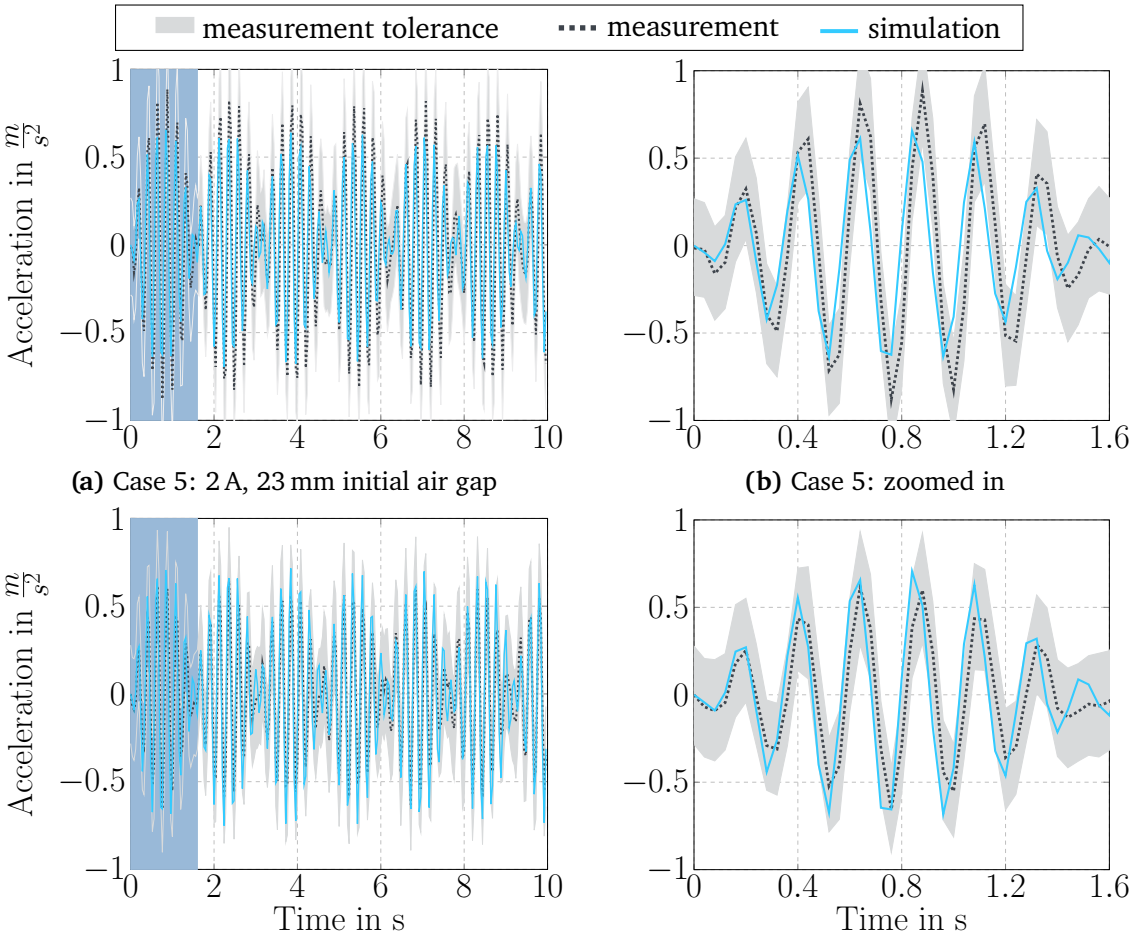

(a) Case 5: 2 A, 23 mm initial air gap

(b) Case 5: zoomed in

(c) Case 8: 4 A, 42.5 mm initial air gap

(d) Case 8: zoomed in

Figure 3.5.: Comparison of measured (black) and simulated (blue) dynamic response with AC current excitation between 2 A and 4 A and changing initial air gaps between 23 mm and 42.5 mm including measurement uncertainties (light grey). On the right-hand side, a zoom in of the first period marked on the left-hand side (blue shaded area) is shown. [34]

The comparison of the time series results for the cases 5 and 8 shows generally a good agreement. Figure 3.5 (a) and (c) show, that the systems' behaviour are similar. The magnified detail of the plot on the right of Figure 3.5 (b) and (d) show, that for both cases, the simulation results lie within the tolerance band of the measurements.

The frequency analysis further demonstrates this consistency. Figure 3.6 shows the power spectral densities of simulation and measurement mean value for both cases. The dominant frequencies are at 4 Hz and 4.7 Hz. Additionally, peaks at 8 Hz and 12 Hz are visible in the simulation, which are not as prominent in the measurement results. The peak at 4.7 Hz can be assigned to the natural frequency of the system, as it was calculated in Section 3.2.2.

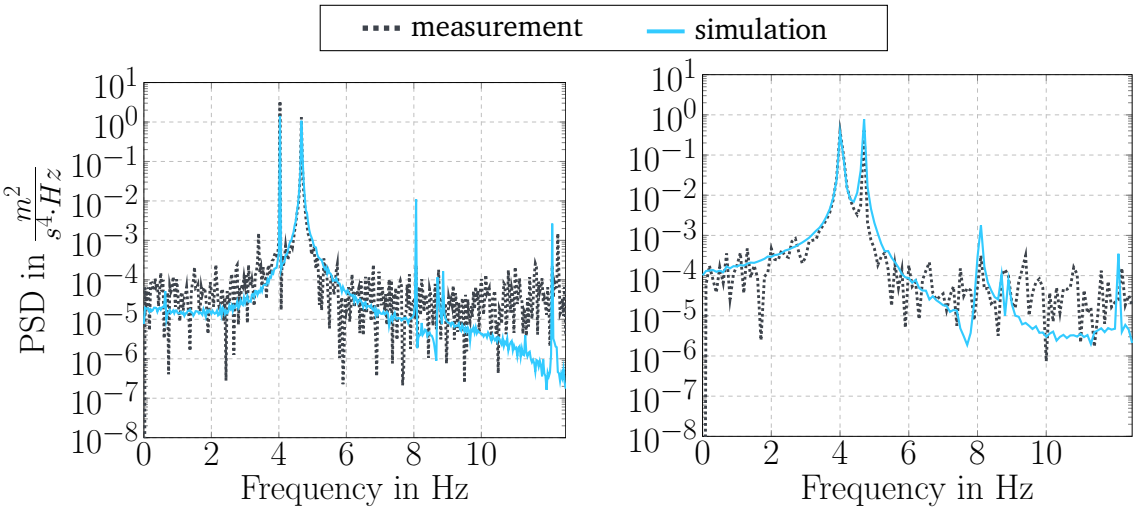

(a) Case 5: 2 A, 23 mm initial air gap

(b) Case 8: 4 A, 42.5 mm initial air gap

Figure 3.6.: Power spectral density (PSD) of measurements (black) and simulation (light blue) for the validation cases 5 and 8. [34]

The peak at 4 Hz corresponds to the excitation frequency, as the frequency of the magnetic attraction force is twice the current frequency, that was set to 2 Hz. The remaining two peaks at 8 Hz and 12 Hz in the simulation are exact harmonics of the excitation frequency. The damping effects for these frequencies, leading to less prominent peaks in the measurements, are not captured in the simulation model. Nevertheless, as their amplitude is significantly lower than the other two peaks, this is expected to be of minor importance, which correlates with the good agreement of the time series results.

In the last step, the cross-correlation further underlines the agreement of the measured and simulated signals, as shown in Figure 3.7. The highest peak of correlation factor is located close to the zero time shift. A magnified detail plot allows identifying the exact position of the maxima. In case 5 it is at 0.04 s time shift and for case 8 it is exactly at zero time shift. In both cases, the correlation factor is above 0.8. Generally, a boundary condition value for strong correlation does not exist and is assumed to be strongly case dependent. One value stated in literature as a proof of strong correlation is a value of 0.7 or higher[84]. Therefore, the signals in this study are considered as strongly correlated. The remaining differences can be attributed to the uncertainties of the model input values and the coupling can be considered as validated.

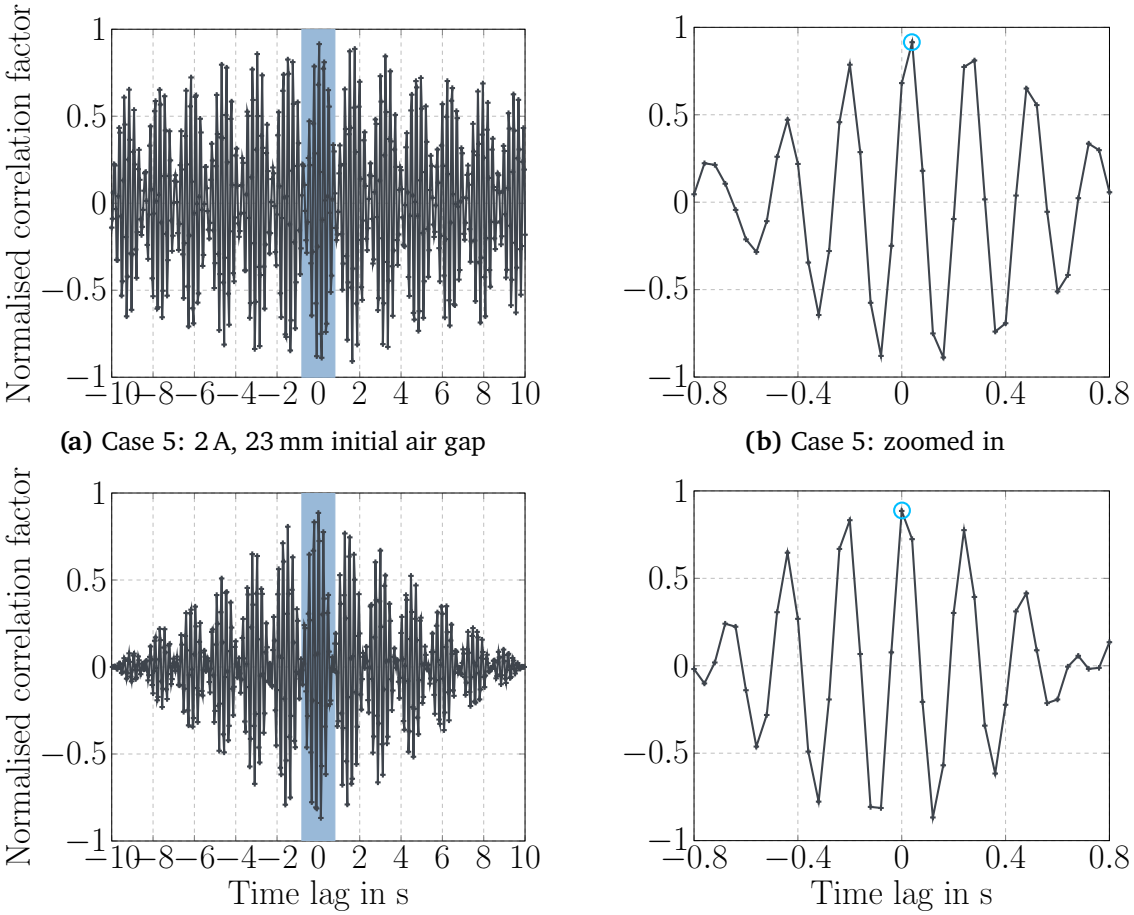

(a) Case 5: 2 A, 23 mm initial air gap

(b) Case 5: zoomed in

(c) Case 8: 4 A, 42.5 mm initial air gap

(d) Case 8: zoomed in

Figure 3.7.: Normalised cross-correlation factors of the comparison of measurement and simulation for the cases 5 and 8. The right-hand side shows a zoom of the blue shaded area on the left-hand side. A light blue circle marks the optimal correlation factor. [34]

Chapter 4

Modelling

As explained before in Chapter 2, one important method to check and develop new technical designs is modelling and simulation. It helps to reduce the effort and expenses for prototypes. Besides the use in the development phase, simulations allow analysing a single physical phenomenon that is difficult to isolate in experiments. Simulations can disregard phenomena that are unavoidable in reality, e.g. damping effects. This simplification can help to understand dependencies that can not be easily identified in a complex system.

This study uses the advantages of simulation models to investigate and understand possible EmeIs in WTs. Therefore, a model of the complete system, including the WT components from the blades to the generator, is needed. Section 2.2 outlines, that state-of-the-art WT models do not include electromagnetic models of the generator. As a consequence, two models, one for the state-of-the-art WT and one of the generator, are needed for this study. The WT model used for this work is described in Section 4.1. There is no state-of-the-art method for generator modelling readily available for coupled investigations. For this reason, two generator models of varying fidelity are used, i.e. one analytical and one FEM model. Details are given in Section 4.2. For the mentioned system analysis, the models of WT and generator need to be coupled. The implementation of the electro-mechanical coupling for the FEM electromagnetic model is based on the methods of Chapter 3. The setup of the couplings for WT and generator is explained in Section 4.3. Parts of this chapter have been included into the author's publication [85].

4.1. Wind turbine

To model the WT, this study uses the IEA 15MW reference WT with a monopile substructure, as described in Section 2.1.4. The open source model available in *OpenFAST* is transferred to *Simpack* that offers additional functionality, which eases the coupling. A detailed comparison of the two software programs is given in Section 2.2.5. After the transfer of the reference model to *Simpack* as a baseline model, a second *Simpack* model is implemented with a detailed drive-train model. This is needed to enable the electro-mechanical coupling. The steps of resolving the drive-train are outlined in Section 4.1.1. The influences of the additional DoF to the system behaviour are explained in Section 4.1.2. The model setup including the solver settings is given in Section 4.1.3. A code-to-code validation between the *OpenFAST* reference model and the two *Simpack* models is performed in Section 4.1.4.

4.1.1. Model definitions

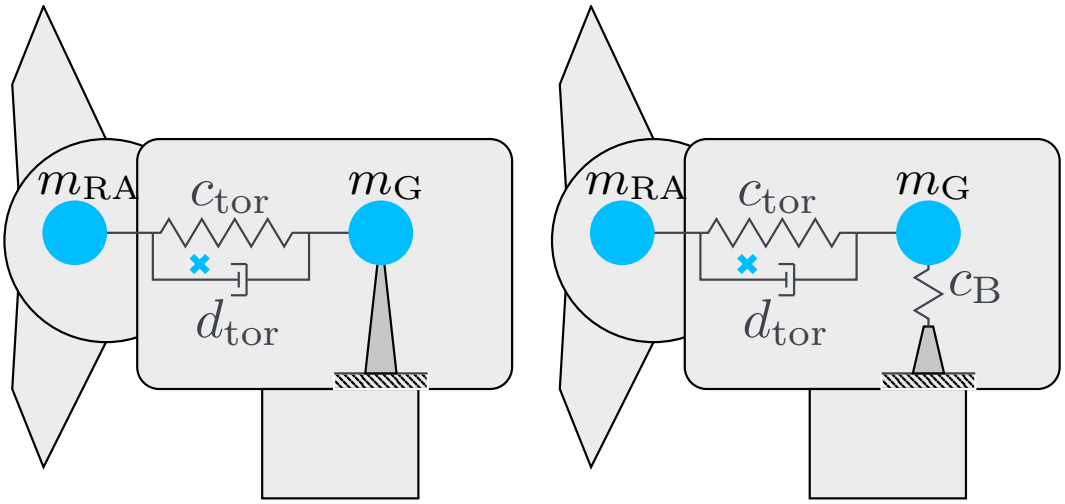

(a) baseline **(b)** detailed

Figure 4.1.: Illustration of drive-train fidelity, showing (a) the standard torsional spring damper representation named baseline model and (b) the resolved drive-train with transversal DoF of the generator to model generator eccentricity, named detailed model. The cross is marking the centre of gravity of the nacelle.

The *OpenFAST* model represents the state-of-the-art modelling of WTs. A sketch of the modelling approach is given in Figure 4.1 (a). The drive-train is modelled as a rotating point mass m_{G} with a mass moment of inertia around its rotation axis. This point mass is connected to the WT rotor with a torsional spring damper element, representing the

torsional stiffness c_{tor} and damping d_{tor} of the main shaft. Between the rotating and non-rotating components in the nacelle, only the rotational DoF is enabled. The mass m_{G} can only rotate around the shaft axis. Lateral movements in all directions are disabled. The non-rotating components are also reduced to a point mass with a mass moment of inertia around the three axis. This point mass includes all non-rotating tower top components like the nacelle housing and power electronic devices. The resulting centre of gravity of the nacelle, including rotating and non-rotating drive-train components, is marked with the little x.

As explained in Section 2.1.2, EmeIs are caused by non-uniform air gaps in the generator. In this study, the focus is put on eccentricity as reason for non-uniform air gap distribution. The introduced baseline model though is based on the assumption of a perfectly aligned generator rotor and stator. Lateral DoF allowing for eccentricity are not included. Therefore, a second model with additional DoF is needed for this study. A sketch of the resulting drive-train model is given in Figure 4.1 (b). The lateral DoF in the generator in vertical direction is illustrated with the changed support of the generator rotor. An equivalent implementation is used for the horizontal movement, in and out of the drawing plane of the figure. It can be seen from the figure that this leads to an additional force element, representing the main bearings, to keep the generator rotor and the attached WT rotor assembly at its location.

The modelling of bearings can be done with different level of detail. The simplest representation would be a radial spring. More detailed representations would include the rolling elements as rigid bodies, resulting in a MB model of the bearing. The highest level of detail could be achieved using the FEM. The capabilities to analyse load distributions and dynamic effects inside the bearing increase with the level of detail. At the same time, the computational effort of solving the equations grows significantly. For this study, only the supporting behaviour of the bearings is relevant and detailed analyses of the internal load distribution are not needed. Therefore, the simplest representation as a radial spring is considered sufficient and with limited computational effort.

The spring can be modelled by two approaches: a linear and a non-linear stiffness curve. The first is characterised by a constant stiffness value c, while the latter uses a displacement dependent stiffness curve. Commonly it is assumed to be sufficient to model a bearing as a linear spring with its spring stiffness constant c in $\frac{\text{N}}{\text{m}}$ [43, 78, 79, 86]. The WT

documentation lists as main bearings a fixed front bearing and a floating back bearing. Displacements along the shaft axis only decrease the effective length of the generator, which has minor effects to EmeIs. Thus, the axial DoF is neglected in this work, to keep the computational effort within reasonable bounds. Therefore, the floating back bearing in this study is also simplified to a fixed support. For both bearings, a stiffness value needs to be specified. State-of-the-art methods model the bearing as FEM model based on its geometry to derive the stiffness values. Details about materials and bearing components like rolling element geometry, needed for this approach, are not available. Therefore, the exact stiffness constants of the given bearing configuration of the reference WT can not be derived. However, the BS is essential for the occurrence of interactions (cf. Section 2.3 and Section 2.4). Because of the lack of BS values c, it is assumed as variable in a parameter study. Results are shown and discussed in Chapter 5.

Besides the BS, the eccentricity of a generator is expected to be influenced by the manufacturing and assembly tolerances. These tolerances can lead to constant misalignment between rotor and stator, leading to a constant eccentric excitation force. Effects of such tolerances to EmeIs will also be studied in Chapter 5. The implementation into the *Simpack* model is explained in the following.

The position of the joint connecting generator rotor and stator is defined by a local coordinate system. The position of this local coordinate system is defined relative to the centre of the generator stator. A constant eccentricity can then be achieved by an offset between the local coordinate system and the stator centre. This can be defined in y and z direction independently, as illustrated in Figure 4.2. To avoid that the bearings experience the assembly misalignment as loading, pushing the generator back into perfect alignment, also the reference marker of the bearings needs to be shifted with the rotor centre marker. Eccentricity due to mass imbalance at the generator rotor or shaft are not investigated in this study.

With the described modifications, the mechanical model is ready to be used in EmeI analysis. The steps to couple this model to the generator model are described in Section 4.3.

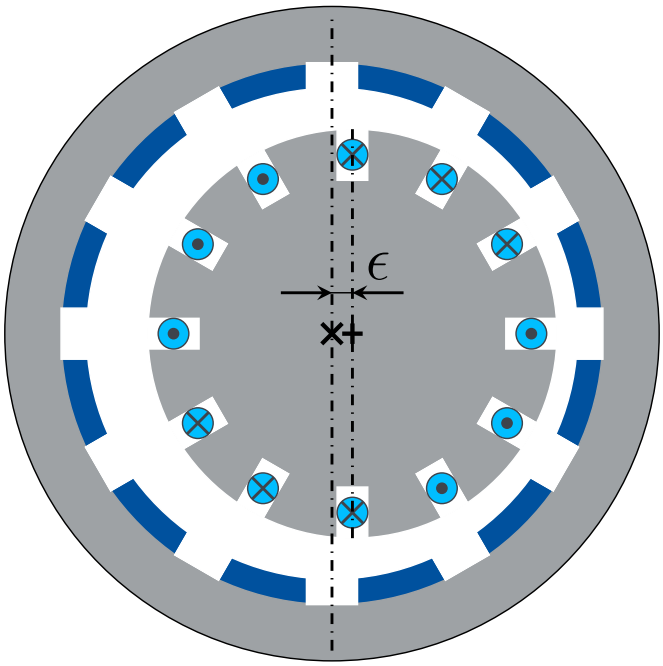

Figure 4.2.: Representative illustration of definition of constant eccentricity due to assembly tolerances as used in the WT model. The position of the reference coordinate system for the rotor and bearings (**x**) is defined relative to the centre of the stator (+) with the distance ϵ in both transversal directions. Here, the horizontal direction is shown exemplarily.

4.1.2. Influence of added drive-train degree of freedom

The added radial DoF, described in Section 4.1.1, changes the system's dynamic behaviour. A description of the resulting changes with their explanation is provided in this subsection.

The BS c_B adds a natural frequency f_B depending on the rotating mass m_{rot}, being the sum of the rotor assembly and the generator rotor. In case of a one-mass-spring-system, f_B can be calculated according to Equation (4.1).

$$2\pi f_B = \sqrt{\frac{c_B}{m_{rot}}} \tag{4.1}$$

Considering the position of the generator, this mode couples to two existing modes of the WT. Figure 4.3 illustrates the position of the generator: In sub-image (a) from the front (a) and in (b) from the top. The WT is reduced to point masses being connected with springs representing the stiffness of the included components.

The spring with the stiffness c_B represents the BS in all subplots. The point masses are the non-rotating mass of tower, foundation and nacelle as m_1 and the rotating mass of

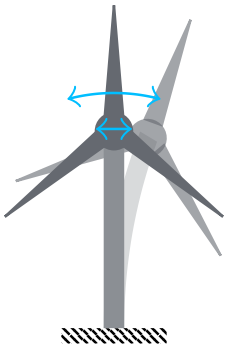

(a) front view

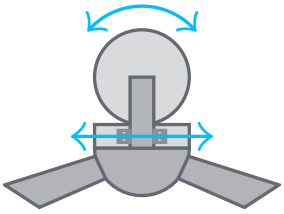

(b) top view

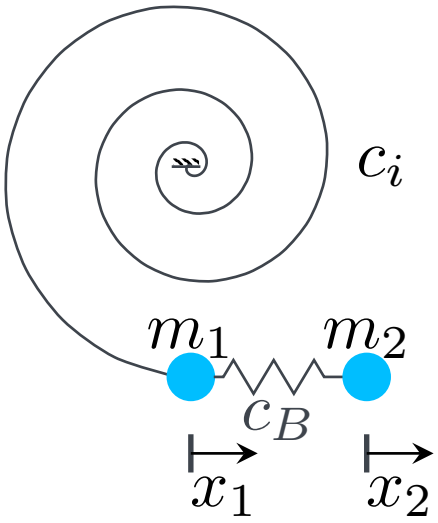

(c) circular tower stiffness

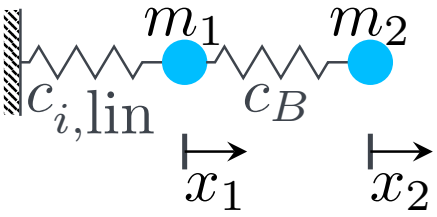

(d) linearised tower stiffness

Figure 4.3.: Representation of WT model as two DoFs system, including the main BS c_B and (a) the SS bending stiffness in the front view of the WT or (b) the Monopile torsion (MT) stiffness in the top view of the WT. From these views two simplified models are derived in (c) using a circular spring, which is linearised in (d).

WT rotor assembly and generator rotor as m_2. In (c) the rotation due to bending or torsion are considered as a circular spring, which is linearised in (d). The rotational displacements due to bending or torsion are expected to be small, keeping angles below 5°. Therefore, x_1 can be described based on the linearised sine-function as $x_1 = \gamma \cdot l$. The force acting on mass m_1 in the direction of x_1 on the example of torsion can then be written as $F_1 = c_\mathrm{tor} \cdot \gamma = c_\mathrm{tor} \cdot \frac{x_1}{l} = c_\mathrm{tor,lin} \cdot x_1$ with $c_\mathrm{tor,lin} = \frac{c_\mathrm{T}}{l}$.

$$\begin{bmatrix} m_1 & 0 \\ 0 & m_2 \end{bmatrix} \cdot \begin{bmatrix} \ddot{x}_1 \\ \ddot{x}_2 \end{bmatrix} + \begin{bmatrix} c_{i,\mathrm{lin}} + 2 \cdot c_\mathrm{B} & -2 \cdot c_\mathrm{B} \\ -2 \cdot c_\mathrm{B} & 2 \cdot c_\mathrm{B} \end{bmatrix} \cdot \begin{bmatrix} x_1 \\ x_2 \end{bmatrix} = 0 \qquad \text{with } i \,\epsilon\, [\mathrm{SS, tor}] \quad (4.2)$$

Therefore, the system matrices of the reduced order models can be given in both cases with Equation (4.2). The solution of such a system is well known, and the system has two modes. The first mode describes the in-phase oscillations of m_1 and m_2. It has a lower natural frequency and the frequency is close to the SS or MT modes of the baseline model. The second mode describes the case of m_1 and m_2 moving in opposite directions. This mode has a natural frequency closer to f_B. A first estimation of the stiffnesses' magnitude is obtained

Table 4.1.: Model parameters from *Simpack* baseline model to determine the representative stiffness for a two DoFs representation and the determined values with a mass $(m_1 + m_2) = 2.446 \cdot 10^6$ kg

mode	f_{base} in Hz	$c_{i,lin}$ in N/m
SS	0.190	$3.48 \cdot 10^6$
MT	5.138	$2.55 \cdot 10^9$

from the baseline model: The representative stiffnesses of the tower monopile assembly are calculated after rearranging Equation (4.1) to $c_{i,lin} = (2\pi f_{base})^2 \cdot (m_1 + m_2)$. The resulting stiffness parameters are listed in Table 4.1.

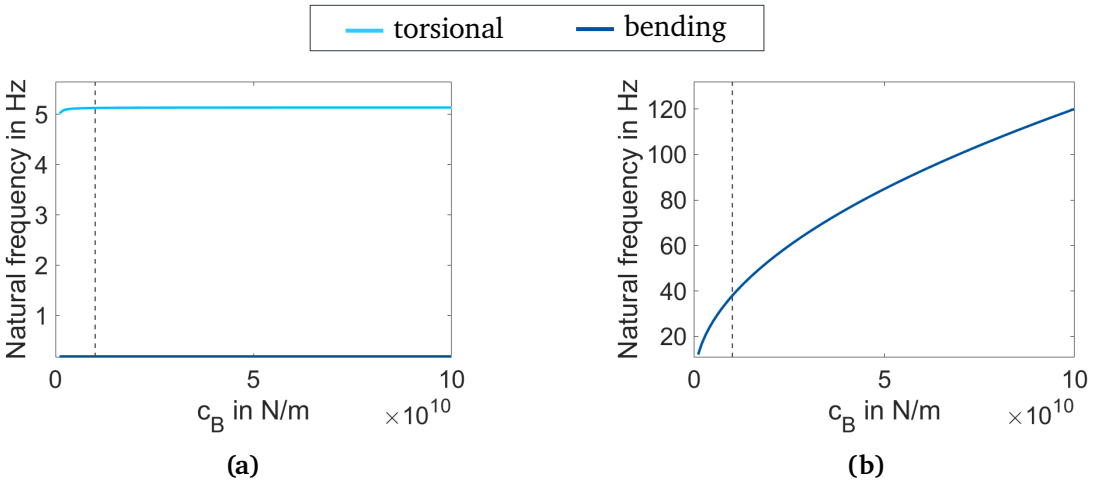

Figure 4.4.: Influence of the BS c_B on the two natural frequencies in (a) to the first system mode and in (b) to the second system mode of the simplified systems with two DoFs for torsion (light blue) and bending (dark blue) of the tower.

After deriving two reduced models of the WT, an isolated analysis of the influence of the additional DoF to these modes can be performed. In the following, all parameters of Equation (4.2) are varied and their isolated influence to the natural frequencies of the modes is studied. First, the BS c_B is analysed for a range of stiffnesses from $10^9 \frac{N}{m}$ to $10^{11} \frac{N}{m}$. Figure 4.4 shows the influence of the BS on the two modes for each system. The influence on the first mode in both systems is insignificant, whereas the second natural frequency

increases from 10Hz to 120Hz. Here, the torsional and bending frequencies are equal for all BS.

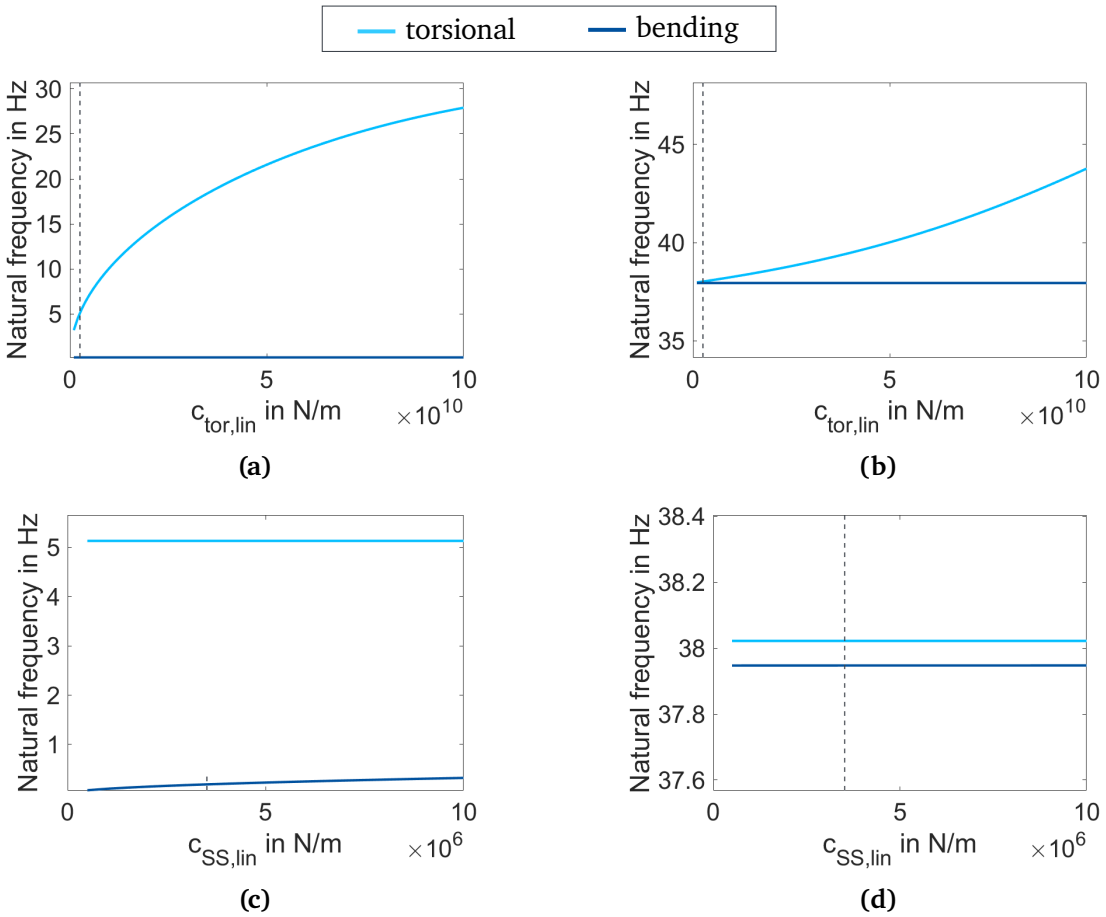

Figure 4.5.: Influence of the tower stiffness $c_{i,\text{lin}}$ to the two natural frequencies of the simplified systems with two DoFs in (a) and (b) for torsion and in (c) and (d) for bending of the tower with a constant BS $c_\text{B} = 10^{10}\frac{N}{m}$.

Then, the influence of the stiffness parameters $c_{\text{SS,lin}}$ and $c_{\text{tor,lin}}$ of the tower-monopile assembly on the two modes with a constant BS of $c_\text{B} = 10^{10}\frac{N}{m}$ are presented in Figure 4.5. Here, (a) and (b) show the influence of the linearised torsional stiffness in a range of $c_{\text{tor,lin}} \in [10^9\frac{N}{m}, 10^{11}\frac{N}{m}]$ on the system. For this parameter variation, the bending modes stay constant, as indicated with the horizontal lines. Figure 4.5 (c) and (d) show the influence of the bending stiffness in a range of $c_{\text{SS,lin}} \in [10^6\frac{N}{m}, 10^7\frac{N}{m}]$, respectively, with constant torsional modes. Again, (a) and (c) show the natural frequency of the first system mode and (b) and (d) show the natural frequency of the second system mode. From this figure, it can be seen, that the torsional stiffness influences both modes, i.e. both light blue curves in (a) and (b) increase with the stiffness. The bending stiffness only influences the first

mode's frequency, as only the dark blue curve in (c) changes with the stiffness, but not in (d). Looking at the magnitudes of the stiffnesses investigated in this study, the torsional stiffness is of the same magnitude as the BS ($c_T \approx c_B$), but the bending stiffness is several magnitudes smaller than the BS ($c_{SS} << c_B$). This causes the difference in their influence to the second system mode.

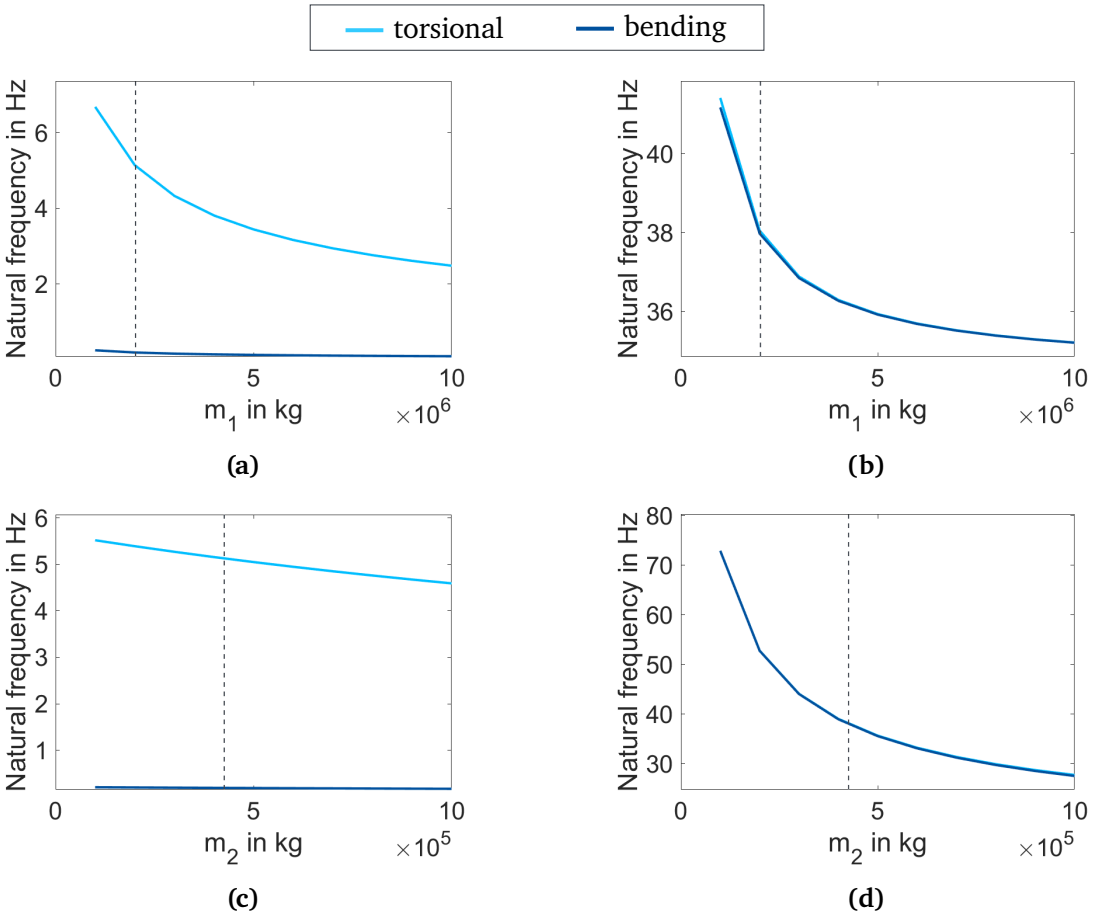

Figure 4.6.: Influence of tower top masses in (a) and (b) for non-rotating mass m_1 and in (c) and (d) for rotating mass m_2 on the two natural frequencies of the simplified systems with two DoFs for torsion and bending of the tower with a BS $c_B = 10^{10}\frac{N}{m}$. (a) and (c) show the first system mode, and (b) and (d) show the second system mode.

The last parameters studied are the rotating and non-rotating masses m_1 and m_2. Their influence to the modes is shown in Figure 4.6. The influence of the non-rotating mass m_1 in (a) and (b) is dominant in the first mode (a), whereas the rotating mass m_2 in (c) and (d) dominates the second mode (d). In all cases, increasing the masses reduces the natural frequency. This is expected according to Equation (4.1). The influence of the analysed parameters on the three system modes are summarised in Table 4.2.

In summary, the BS does not influence the first bending mode and the tower bending

Table 4.2.: Summary of the influences of the SS stiffness $c_{SS,lin}$, the MT stiffness $c_{tor,lin}$, the non-rotating system mass m_1, rotating system mass m_2 and the BS c_B on the system modes of SS bending f_{SS}, MT f_{tor} and bearing vibration f_B as increasing (+), no influence (o) or decreasing (-)

Parameter	f_{SS}	f_{tor}	f_B
$c_{SS,lin}$	+	o	o
$c_{tor,lin}$	o	+	+
m_1	-	-	-
m_2	-	-	-
c_B	o	o	+

stiffness does not influence the second system mode. This supports the state-of-the-art design procedure, i.e. that the transversal DoFs can be excluded from the drive-train. At the same time, the MT stiffness influences the second system mode, though the BS does not influence the first MT mode. Therefore, a coupled system design approach can be relevant to avoid torsional vibrations in the WT tower.

4.1.3. Mechanical solver settings

Besides the definition of DoF parameters of the WT components like masses and stiffnesses, settings of the numerical solver need to be specified. This includes communication intervals between different modules, like the aerodynamics and the elastic solver, or the general convergence criteria.

The communication interval to the aerodynamic solver was set to 0.02 s. This setting was found by running test simulations with *OpenFAST* and *Simpack* and compare the results. With the chosen interval, the solver behaved robustly and is computationally efficient. The controller was initially also called every 0.02 s in accordance with [24]. However, this interval showed resonance behaviour for the model with the detailed drive-train. The resonances were caused by the natural frequency of the added DoF, as this frequency was close to the controller's Nyquist frequency of 25 Hz. Therefore, the communication interval was decreased to 0.01 s. This communication interval is a trade-off between the Nyquist criteria and the computational effort, as the natural frequencies of the main bearing for high BS were still above the Nyquist frequency. However, the high BS reduced the oscillation amplitude and avoided significant interactions with the controller.

The solver tolerances in *Simpack* were set to $\Delta s_{\text{abs},i} = 10^{-7}$ for the absolute tolerance and $\Delta s_{\text{rel},i} = 10^{-5}$ for the relative tolerance. The tolerance for positions has been adapted to $\Delta s_{\text{abs,pos}} = 10^{-9}$ for absolute tolerance. This results from the expected scale for generator eccentricity. The maximum of allowable eccentricity, including electromagnetic forces, is 2 mm according to the WT definition. Furthermore, the generator size of 10 m diameter needs to be considered. This limits the assembly tolerances to the lower end. Nanometres are expected not to be feasible without unreasonably high cost. At the same time, the maximum allowable eccentricity should occur only in extreme cases and not during normal operation. Therefore, the expected mean eccentricity is assumed to be in the range of μm. Excluding the electromagnetic forces, the range of occurring eccentricity decreases further. To ensure trustworthy results also for the calculated eccentricity, the chosen tolerance needs to be significantly smaller. Choosing the tolerance for positions with $10^{-9}m$ - a factor of thousand smaller than the assumed mean eccentricity of $\mu m = 10^{-6}m$ - is expected to be sufficient.

As a last step, the tolerance of the MB and the electromagnetic solver need to fit to ensure overall system convergence. This requires a more elaborate study, and thus more details about the interactions of the solvers are presented in Section 4.3.

4.1.4. Code-to-code comparison of OpenFAST and Simpack models

The derived models in *Simpack*, baseline and electro-mechanical, are compared to the reference model in *OpenFAST* in a code-to-code comparison. This code-to-code comparison is done in two steps. At first, the system natural frequencies are identified and compared. Section 4.1.2 showed that the dynamic behaviour of the system will differ, when including an additional DoF. Nevertheless, the natural frequencies of the isolated components need to agree. Therefore, all DoF except for one are set to rigid and then the according frequency is identified from a simulation. The procedure is repeated for each of the DoF. The comparison is given in Table 4.3. The first natural frequencies of blades and tower match with the reference model. The higher frequencies show a higher deviation, which is considered acceptable, as the major contribution to the dynamics come from the first natural frequencies.

As a second step, the steady state behaviour of all models is compared. The results are

Table 4.3.: Comparison of isolated component natural frequencies in Hz of the reference model in *OpenFAST* and the implemented *Simpack* model, with the percentage difference relative to the *OpenFAST* reference model. The main components compared are the blade with its first three natural frequencies in flap and edge direction, the first four tower modes in Fore-aft (FA) and SS direction and the monopile in FA, SS and MT direction. The last column gives the used modal damping coefficients in percent for both models.

mode	*OpenFAST* [Hz]	*Simpack* [Hz]	Δ_{rel} [%]	modal damp. [%]
1st flap	0.547	0.555	+1.46	3
1st edge	0.649	0.632	-2.62	3
2nd flap	1.585	1.667	+5.17	3
1st FA	0.244	0.246	+0.82	1
1st SS	0.244	0.244	+0.00	1
2nd FA	0.688	0.807	+17.30	1
2nd SS	0.728	0.775	+6.46	1
1st MFA	0.261	0.293	+12.26	1
1st MSS	0.261	0.293	+12.26	1
1st MT	2.705	2.833	+4.73	1
2nd MFA	4.358	6.837	+56.88	1
2nd MSS	4.362	6.837	+56.74	1

summarised into three characteristic curves. These include the power curve in Figure 4.7 (a), the pitch curve in Figure 4.7 (b) and the generator moment over rotational speed curve in Figure 4.7 (c). All models agree in steady state behaviour. With the presented code-to-code comparison, the implemented *Simpack* models are considered validated and can be used for further analysis.

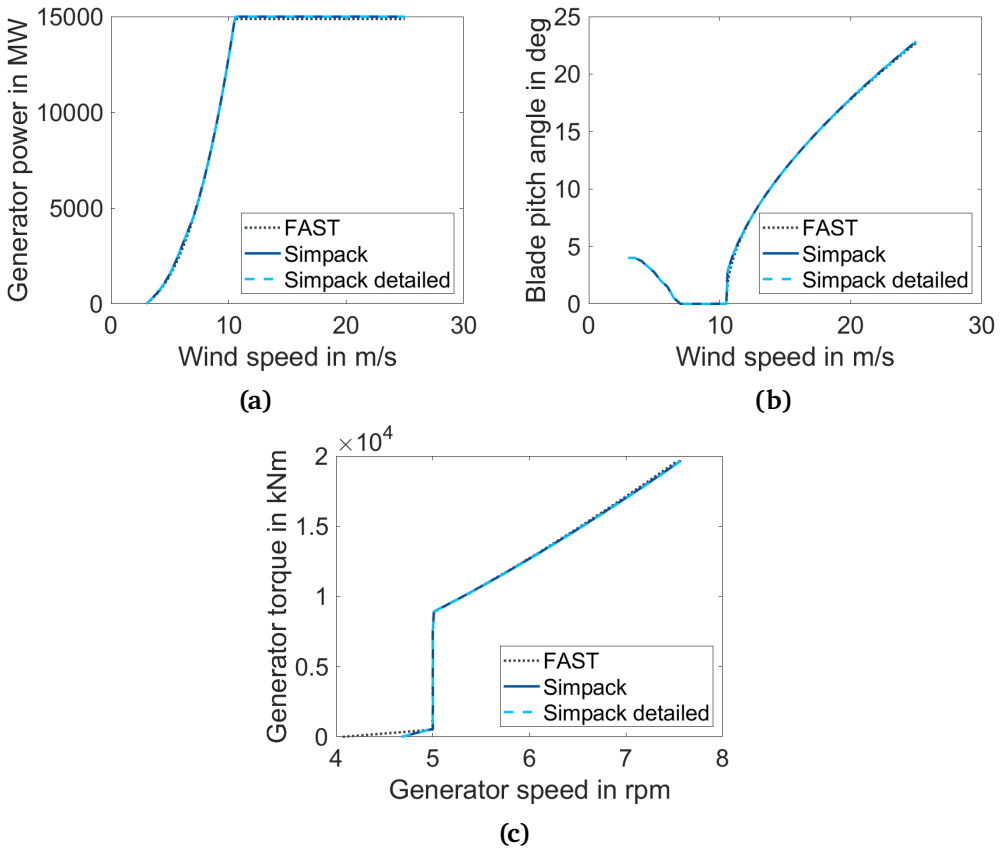

Figure 4.7.: Code-to-code comparison of steady state behaviour of the *OpenFAST* reference (black dotted), *Simpack* state-of-the-art (blue solid) and *Simpack* detailed (light blue dashed) with (a) power curve, (b) pitch curve and (c) speed torque curve

4.2. Generator

Besides the WT model, a description of the generator is needed to analyse EmeIs. This study includes two approaches to model the generator, an analytical description of the quasi-static behaviour and a FEM model including transient phenomena. The analytical approach allows a fast and broad investigation of possible interactions, including parameter studies. The second approach is significantly more expensive in computation and only allows a limited number of simulations. Therefore, it is used to check whether the analytical model is able to represent all the phenomena that are relevant for EmeIs in WTs. The analytical representation is introduced in Section 4.2.1 and the numerical implementation is described in Section 4.2.2. The two models are compared in Section 4.2.3. A validation of the analytical model against the numerical model for coupled simulations is presented in Chapter 5.

4.2.1. Analytical model

The analytical model is taken from [33]. It represents the electromagnetic forces as classical

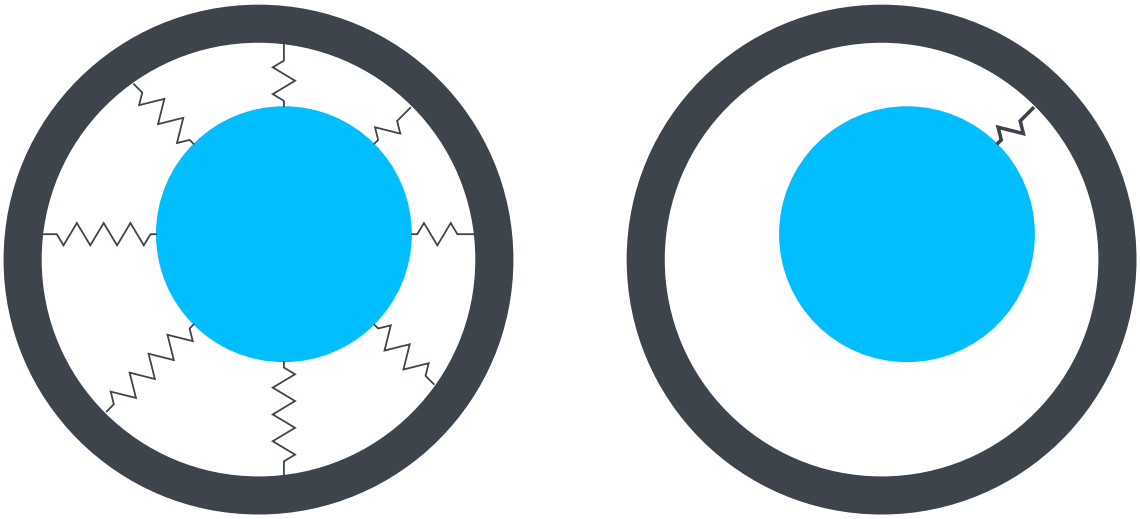

(a) distributed forces **(b)** integrated force

Figure 4.8.: Illustration of (a) the distributed stiffnesses and (b) the resulting stiffness being the coordinate transformed sum of the distributed ones

springs distributed over the circumference, as shown in Figure 4.8 (a). Each spring represents the resulting force over one of the N sectors. [33] defines several types causing unbalanced electromagnetic forces. The type describing eccentricity due to rigid body displacements is called mode 1. The analytical equation for mode 1, representing the stiffness per sector for eccentricity c_{PM} is given in Equation (4.3) to Equation (4.5). The equations depend on the azimuth angle θ_i, the sector width β, the mean eccentricity $\bar{\epsilon}$ and the eccentricity amplitude over the circumference $\hat{\epsilon}$ (cf. Figure 4.9). After integrating over each sector, θ_i is discretised, running from $\frac{\beta}{2} : \beta : 2\pi - \frac{\beta}{2}$ to include each sector's spring force only once. All other values are constants of the generator and listed with their definition in Table 2.2.

The equations show, that the spring stiffness at each position of the circumference depends on the local air gap length $\delta(\theta_i)$. The implementation in *Simpack* needs a resulting force in the direction of the smallest air gap only (compare Figure 4.8 (b)).

To derive the resulting force from the local stiffnesses, the procedure of Figure 2.4 is used. Equation (4.3) is multiplied with the local air gap length given by Equation (4.6). The equation for local radial forces is evaluated for each sector θ_i. The resulting local forces are split into the global y and z components using the cosine and sine component of the local

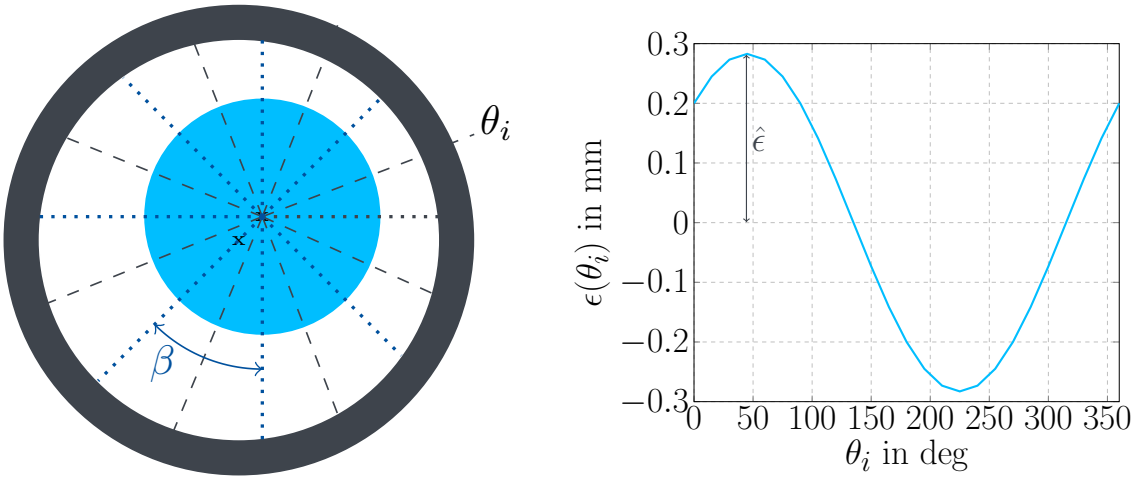

(a) angle definitions **(b)** eccentricity definition

Figure 4.9.: Parameter definitions of the analytical model for the sector width β, the discrete azimuth angle θ_i and the local eccentricity $\epsilon(\theta_i)$.

radial force. The forces are added for the y and z directions and combined to the resulting radial force using the Pythagorean equation.

$$c_{\mathrm{PM}}(\theta_i) = \frac{F_{\mathrm{PM}}^2 \cdot l_{\mathrm{S}} \cdot R \cdot \mu_0}{4 \cdot (\delta_0 + \frac{h_{\mathrm{PM}}}{\mu_{\mathrm{r}}} - \bar{\epsilon})^4 (\delta_0 - \bar{\epsilon} - \hat{\epsilon} sin(\theta_i))} \kappa_{\mathrm{PM}}(\theta_i) \tag{4.3}$$

$$F_{\mathrm{PM}} = \frac{4 B_{\mathrm{r}} h_{\mathrm{PM}}}{\pi \mu_0 \mu_{\mathrm{r}}} \sin\left(\frac{\pi b_{\mathrm{PM}}}{2\tau_{\mathrm{p}}}\right) \tag{4.4}$$

$$\begin{aligned} \kappa_{\mathrm{PM}}(\theta_i) = & 2\hat{\epsilon} \cdot \\ & \left[\left(\delta_0 + \frac{h_{\mathrm{PM}}}{\mu_{\mathrm{r}}} - \bar{\epsilon} - 0.25\hat{\epsilon}\sin(0.5(\beta - 2\theta_i))\right)\cos(0.5(\beta - 2\theta_i))\right. \\ & \left. - \left(\delta_0 + \frac{h_{\mathrm{PM}}}{\mu_{\mathrm{r}}} - \bar{\epsilon} + 0.25\hat{\epsilon}\sin(0.5(\beta + 2\theta_i))\right)\cos(0.5(\beta + 2\theta_i))\right] \\ & + \beta \cdot (0.5\hat{\epsilon}^2 + \delta_0 + \frac{h_{\mathrm{PM}}}{\mu_{\mathrm{r}}} - \bar{\epsilon})^2 \end{aligned} \tag{4.5}$$

$$\delta(\theta_i) = \delta_0 - \bar{\epsilon} - \hat{\epsilon}\sin(\theta_i) \tag{4.6}$$

This force is the radial attraction force between the rotor and the stator, acting like a single spring at the location of the shortest air gap, as in Figure 4.8 (b). For a uniform air gap length, the force is zero. Due to the discretisation of the generator into N sectors, the resulting force is not exactly zero. Assuming one spring per pole (i.e. $N = 200$) the remaining radial force is below $10^{-9}\,\frac{N}{m}$. This is considered sufficiently small and the discretisation of $N = 200$ is used.

4.2.2. Finite element model

For the FEM model, the generator was build in *Comsol Multiphysics*. The same IEA *GitHub* repository as for the WT model provides a CAD file in the STEP, which is imported into *Comsol Multiphysics*. The parameters used for the model are stated in Table 2.2.

The stationary solver was set to a relative tolerance of 10^{-5} and the dynamic solver was set to a relative tolerance of 10^{-4}, with an absolute tolerance factor of 1. The direct *Pardiso* solver was used with the *Constant Newton method* as the non-linear solver, combined with a Jacobian matrix evaluation at each iteration. The magnetic vector potential is used unscaled (scaling factor of 1) and the spatial mesh displacement is scaled with a factor of 10^{-6} as the expected eccentricities will be between μm and mm. The time stepping method for the dynamic solver is the BDF solver with a free time step width.

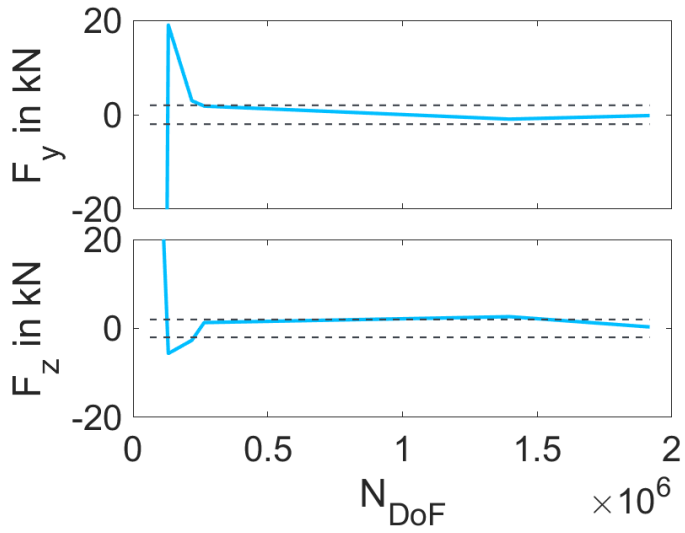

Figure 4.10.: Mesh convergence study, investigating the convergence of the attraction forces in y and z direction depending on the number of DoFs in the mesh, based on a global mesh refinement.

The accuracy of the numerical model is achieved with a classical mesh convergence study. The model accuracy is quantified by the attraction forces in y and z direction, as these values are used by the WT simulation. Figure 4.10 shows the two attraction forces (F_y and F_z) over the number of DoFs (N_{DoF}) of the investigated, globally refined meshes. Rotor and stator are perfectly aligned. Therefore, the expected solution without mesh error for either of the forces is zero. The bending forces in the WT drive-train due to aerodynamics are in the magnitude of $100\,kN$ to $1\,MN$. Therefore, a remaining mesh error of up to 2 % is

deemed as acceptable, indicated by the horizontal dashed lines.

The converged mesh, based on global refinement, shown in Figure 4.10, consists of 1.9 million DoF. This mesh is computationally very expensive. To reduce the number of DoFs, the mesh was optimised by giving problem specific boundary conditions to the meshing solver. This includes restrictions to the number of elements on certain edges. This enforces small element sizes on edges that are most relevant to the force calculation. Edges with only little influence to the force calculation are forced to be meshed with larger elements. The resulting, locally refined mesh consists of 233,574 elements, giving a residual attraction force in the y direction of 1,021 N and in the z direction of 2,192 N. Based on the skewness factor, the mesh has a minimum element quality of 0.141 and an average element quality of 0.7234.

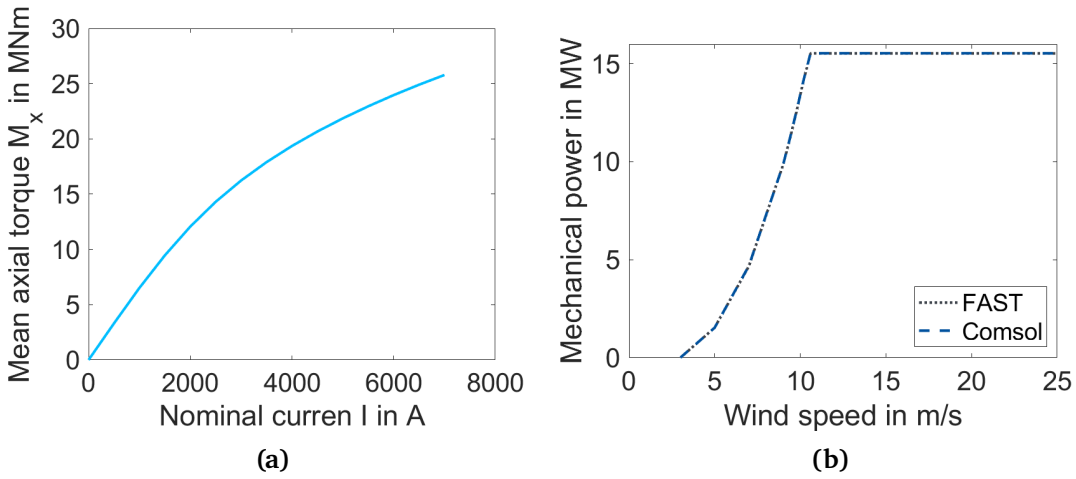

Figure 4.11.: Implementation of variable speed and torque generator showing in (a) the Torque (M) depending on the nominal current (I) input to the coils and in (b) the resulting power curve of *Comsol Multiphysics* in comparison to the *OpenFAST* reference model

The analytical model only depends on characteristics of the permanent magnets and is independent of the operating point defined by the winding current and rotational speed. In contrast, the influence of the winding current for electromagnetic forces is included in the numerical model. In WTs, the winding current has to be adapted for each operating point below the rated power to achieve the needed generator torque. The dependency of the generator torque on the winding current is shown in Figure 4.11 (a). This dependency is included in the numerical model as a look-up table, and the needed torque according to the WT controller is given as input from the MB model to the electromagnetic model.

To test the implementation of the variable speed and torque, the power curve as product

of torque and speed was derived. The comparison of the power curve to the steady state solution of the *OpenFAST* reference model is given in Figure 4.11 (b). It shows very good agreement over all operating points. Therefore, the derived Torque current correlation in Figure 4.11 (a) is considered validated.

4.2.3. Model comparison

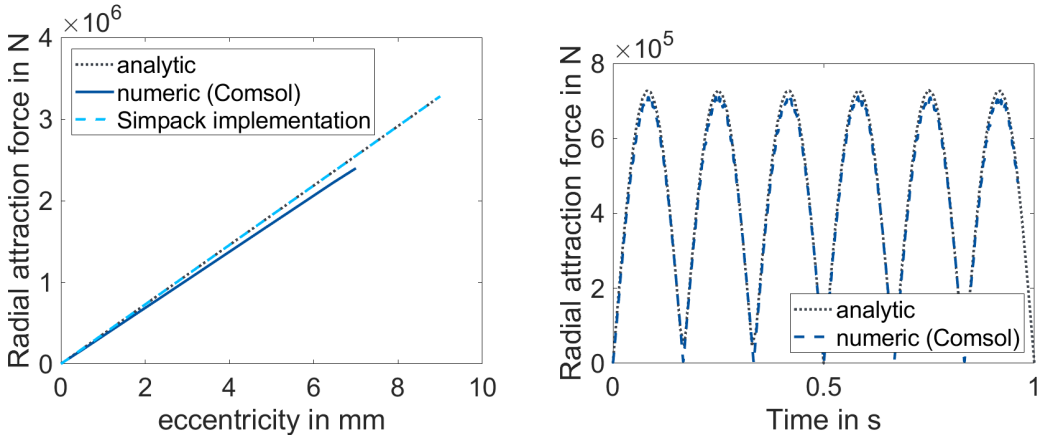

Figure 4.12.: Comparison of numerical and analytical generator model (a) showing the dependency of effective, static eccentricity and radial attraction force for the analytical standalone model (gray dotted), the implementation of the analytical model in *Simpack* (light blue dashed), and the stationary solutions in *Comsol Multiphysics* (dark blue) and (b) showing the radial attraction force for the analytical standalone model (gray dotted) and the numerical *Comsol Multiphysics* solution with dynamic solver (dark blue dashed) for a sinusoidally changing eccentricity

After setting up the electromagnetic models, their implementation is compared, which is explained in detail in this section. First, the behaviour under eccentricity is analysed. This means, the dependency of the resulting radial attraction force in the direction of the smallest air gap over the eccentricity is analysed. For the analytical model, this means, the resulting equation is evaluated for several eccentricities. To check the implementation of the derived equation in the *Simpack* model, the forces under constant eccentricity in steady state simulations is analysed. For the numerical simulations in *Comsol Multiphysics*, stationary simulations for each eccentricity at the rated operating point are performed. The comparison of the three solutions is given in Figure 4.12 (a) and shows a good agreement in general. The *Simpack* implementation of the analytical model agrees exactly with the standalone solution. Compared to the numerical solution, the analytical solution overestimates the attraction force and the absolute error increases with increasing eccentricity. In general,

the analytical solution can be considered a conservative estimate of the more accurate numerical solution. The error with respect to the numerical solution ranges between 6 % and 7.2 % with a mean error of 6.2 %.

A similar conclusion can be drawn from a comparison of a sinusoidally changing eccentricity varying around zero, as shown in Figure 4.12 (b). Here, the analytical solution is compared with a numerical simulation, at the rated operating point. The eccentricity is a sinusoidal function of time, with a frequency of 3 Hz and an amplitude of 2 mm. The two solutions agree in general, but the analytical solution overestimates the radial attraction force at the peak eccentricities. The mean error with reference to the numerical solution is 4.3 %.

In the last step, the implementation of the analytical model in *Simpack* was used to analyse the radial attraction force under dynamic loading, due to a turbulent wind field. The calculated dynamic eccentricity, the demanded torque and the rotational angle of the rotor are given as input to the *Comsol Multiphysics* model and a simulation is performed to determine the numerical, dynamic solution of the radial attraction force. The radial attraction force from the *Comsol Multiphysics* and from the *Simpack* solution are compared. The comparison is shown in Figure 4.13. The upper two plots, (a) and (b), show the unfiltered numerical results compared to the analytical solution. The numerical solution contains high frequency components. These high frequencies can be explained with the rotating magnetic field and the generator geometry that lead to oscillations of the magnetic forces, which are known to cause the torque ripple. In a coupled simulation according to Chapter 3, this frequency will be removed by the communication interval. Therefore, for this comparison, the signals of the numerical solution are low-pass filtered with a passing frequency of 10 Hz. The comparison of the filtered numerical results to the analytical result are presented in Figure 4.13 (c) and (d). The filtering emphasises low-frequency components of the signals.

Due to the displacement resulting out of gravity, the attraction force in the z-direction has to be higher than in the y-direction. The results follow this expectation, as the attraction forces in the z-direction are two magnitudes higher than in the y-direction. For both directions, the magnitudes of the forces between analytical and numerical solution agree well.

In y-direction, the analytical solution of the force remains smaller than the numerical solution, whereas in z-direction the opposite is true. The observed differences between the

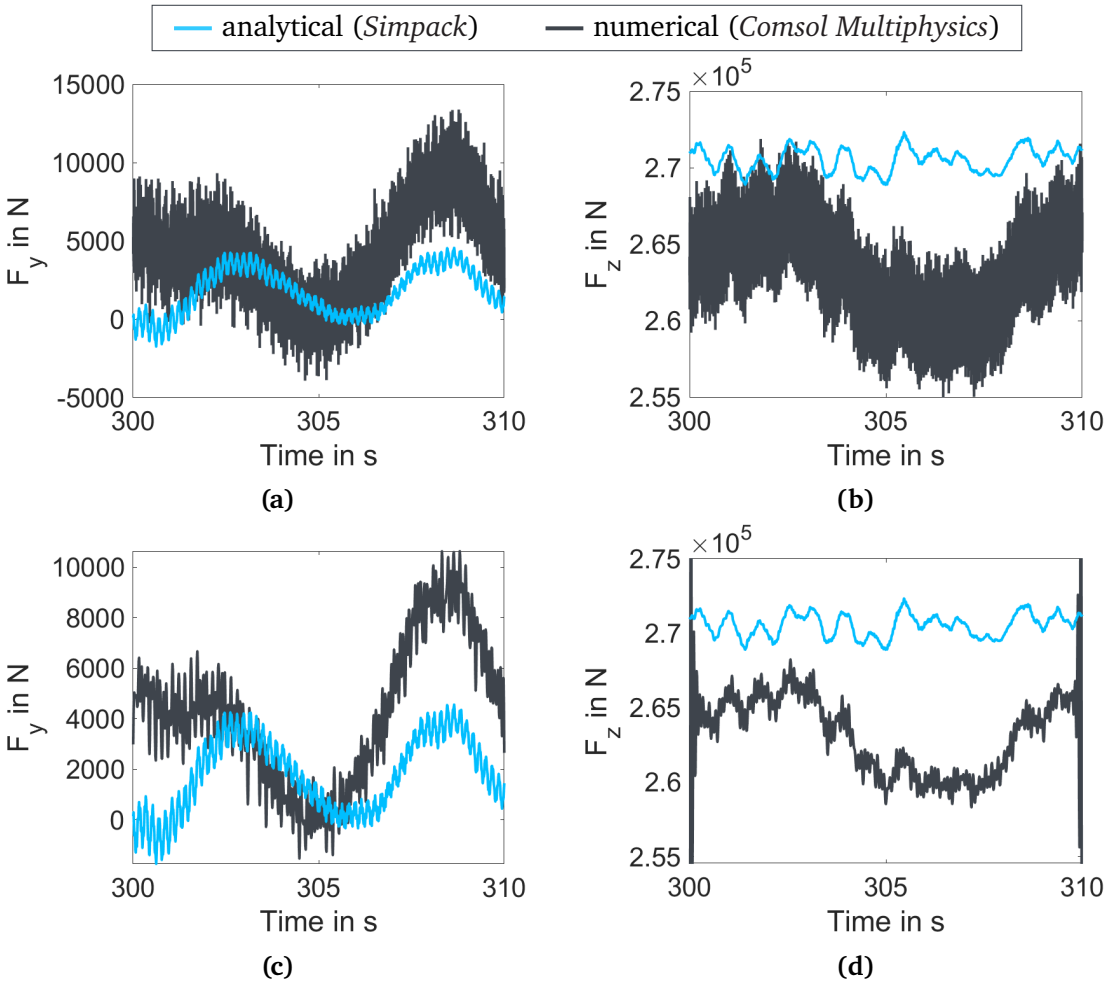

Figure 4.13.: Comparison of analytical model implemented in *Simpack* with the numerical solution of *Comsol Multiphysics* for a dynamically changing eccentricity

two directions can be explained by the remaining numerical error for zero eccentricity and the overestimation error of the analytical model for high eccentricities (compare Figure 4.12). For small eccentricities the numerical error dominates the solution, whereas for higher eccentricities the overestimation of the analytical model dominates. This is also reflected in the mean differences of the compared signals. The mean difference in y-direction with respect to the numerical solution is -17.6 % and in z-direction is 2.8 %. Due to the lower magnitude of the force in y-direction, the difference can be tolerated. For z-direction, the difference is considered as sufficiently small.

The shape of the filtered numerical solution and the analytical solution match to a certain degree. The differences are probably due to numerical errors. The z-direction is showing two prominent frequencies in the numerical solution. The higher frequency with lower

amplitude matches with the fluctuations in the analytical solution. The low-frequency component of the numerical solution, resembling one sinusoidal period, can not be directly explained. In summary, the two models deliver similar results and for higher eccentricities the analytical model is a conservative estimation compared to the numerical model. The comparison will be useful to interpret the differences, when comparing the models in coupled simulations in Chapter 5.

4.3. Coupling set up

After setting up the needed models for the WT and the generator, the models need to be coupled. The coupling methods for the two introduced electromagnetic models are different. Section 4.3.1 explains the coupling of the analytical model and Section 4.3.2 explains the coupling of the numerical model, based on the method presented in Chapter 3.

4.3.1. Analytical model

To couple the analytical generator model from Section 4.2.1 to the WT model, a radial spring force element, using the equation from Section 4.2.1 for the resulting force as *Input function*, was chosen. This function gets the radial distance of the two centres as input and returns the resulting force in the direction of the smallest air gap. The force element was attached to the centres of the generator rotor and stator. To represent the attracting force of rotor and stator, the two centre points need to repel each other in the direction of the smallest air gap. Therefore, the sign of the calculated force needs to be reversed. This implementation models the generator as a non-linear spring with negative stiffness. This additional force element is all that is needed, to couple the analytical generator model to the WT model.

4.3.2. Numerical model

The numerical model of the generator is coupled to the WT model based on the method in Chapter 3. The force element is applied between the centres of the generator rotor and stator, similar to the implementation in Section 4.3.1. Therefore, the distance of the centres of rotor and stator in y-direction and z-direction of the stator coordinate system are handed

over to the numerical generator model. Additionally, the rotation angle of the rotor relative to the stator and the demanded generator torque are passed to *Comsol Multiphysics*. The *Comsol Multiphysics* solution is returned to the WT model and applied to the generator rotor centre after the coordinate transformations from stator coordinates to rotor coordinates.

The generator FEM model is a 2D model, similar to [48, 68]. In this work, the DoFs for tilting around the axes perpendicular to the axis of rotation are excluded. Therefore, one slice, representing the complete generator, is sufficient.

After including the force element of the coupling in the WT model, the co-simulation parameters need to be defined. This means, that the communication interval, and the parameters for interpolation and extrapolation method have to be chosen. A parameter study was conducted, varying the three parameters, to determine the settings with high robustness that are computationally efficient. The interpolation and extrapolation method only influence the computational performance and need to be adapted to the chosen communication interval. The communication interval itself though influences the frequencies transferred from one model to the other. The maximum frequency that can be transferred equals half of the communication frequency, i.e. $f_{\max} = \frac{0.5}{\Delta t}$.

Excitation frequencies on the generator side result from the rotating electric field. The electric field of the generator rotates at 12.6 Hz under rated conditions, corresponding to a communication interval of 0.04 s. Higher harmonics of this frequency can be seen in the output torque and depend on the number of pole pairs and their geometry. These overlaid variations of the torque are called torque ripple and can go above 100 Hz. To analyse the influence of the generator to the WT extensively, a high communication frequency is needed. However, the higher the chosen communication frequency, the higher the computational effort. Reducing the communication frequency increases the simulation error. Therefore, a balance between the two influencing factors needs to be found. The maximum mechanical frequency in the baseline model occurs around 15 Hz, which equals a communication interval of 0.03 s.

To determine the needed communication interval, test simulations are performed. The communication interval is varied between 0.01 s and 0.08 s, which are equivalent to $f_{\max} = 50\,Hz$ and $f_{\max} = 6.25\,Hz$. The results with the 0.01 s communication interval are used as reference results. Multiples of the electrical field frequency, i.e. communication intervals

of 0.04 s and 0.08 s show high fluctuations in the attraction forces leading to a high error compared to the reference result. Therefore, these communication intervals need to be avoided. The remaining communication intervals only show minor differences in the resulting simulation error. Therefore, a high value is chosen, namely the 0.06 s, to minimise the needed computation time.

Investigating the other two coupling parameters, the combination, that showed the best performance was using spline interpolation in combination with constant extrapolation and the communication interval of 0.06 s. These parameters are used in all following coupled simulations.

Chapter 5

Electro-mechanical interactions in wind turbines

The analysis of EmeIs in WTs by numerical simulations, requires accurate physical models, which are used for extensive parameter studies. While the models in this work have been introduced in Chapter 4, this chapter outlines the conducted studies.

The aim is, to better understand the dynamic interactions by simulating different situations. In this study, the state-of-the-art model has been extended, including an additional radial DoF (see Section 4.1.1). In order to distinguish between the introduced changes in the model behaviour due to this DoF and effects from the EmeIs, a model fidelity study is required. First, the fidelity assumptions for the electromagnetic models need to be reviewed. Then simulations with and without electromagnetic forces need to be compared.

Two electromagnetic models for the generator have been introduced and compared in their basic behaviour (see Section 4.2): a numerical and an analytical model. The numerical model enables detailed analyses but is associated with high computational costs. Therefore, extensive studies, including parameter studies, have to be performed with the analytical model. To understand the limitations of such a parameter study, a comparison of the fully coupled dynamic WT simulations with both generator model fidelities is conducted. The results are outlined in Section 5.1.

The new radial DoF introduces two new parameters to the system, i.e. the BS and the

assembly tolerance. To understand their impact on the system behaviour, their values are varied in a parametric study. Additionally, the different operating points of the WT, e.g. different wind speeds, need to be simulated. The investigated parameter space of this work is defined in Section 5.2 together with the evaluation methods. The influence of all the investigated parameters on the system behaviour is analysed in Section 5.3. The first RQ about the interactions of the changed system with the aerodynamics is addressed in Section 5.4. Based on these findings, a more detailed load analysis is performed. Here, the simulation results are analysed with two different foci. First, the effects to drive-train components are investigated in Section 5.5. Then, the effects to the WT components outside the drive-train are studied in Section 5.6. Parts of this chapter have been included into the author's publication [85].

5.1. Influence of electromagnetic model fidelity

Numerical simulation studies of physical phenomena depend on the accuracy of the models used for the study. In this work, two models for the electromagnetic behaviour of the generator, an analytical model and a FEM model, have been introduced in Section 4.2. A first comparison of them was conducted in Section 4.2.3. There, the FEM model was used in stand-alone mode. This section compares the results of both models in a fully coupled simulation with the aero-servo-elastic WT model. From the comparison, advantages and shortcomings of the analytical model are identified.

Two cases, a constant, uniform wind field and a turbulent wind field, are used for the analysis. To ensure, that the two models have comparable initial conditions and to reduce numerical transients, a set of initial states was derived from a pre-processing simulation. These states are positions, velocities, and accelerations of blade and tower sections and the shaft. This set of states was determined using the analytical model of the generator and running a simulation of 800 s with uniform wind inflow of 10 m/s. The states of the WT at the end of this simulation were then used as input for the compared simulations. The comparison is based on sensors at the location of the generator, namely the electromagnetic forces of the generator, the forces of the main bearings and the resulting eccentricity of the generator. The results are split into y- and z-component in a non-rotating coordinate system, where the x-axis is aligned with the shaft axis. Additionally, the generator torque demand of

the controller, the generator speed, the pitch demand of the controller and the tower top SS displacement are investigated. With these signals, the numerical transients and feedbacks of the models to the controller and WT dynamics can be studied. The available simulation results are limited to 15 s of simulation time due to the available computational power.

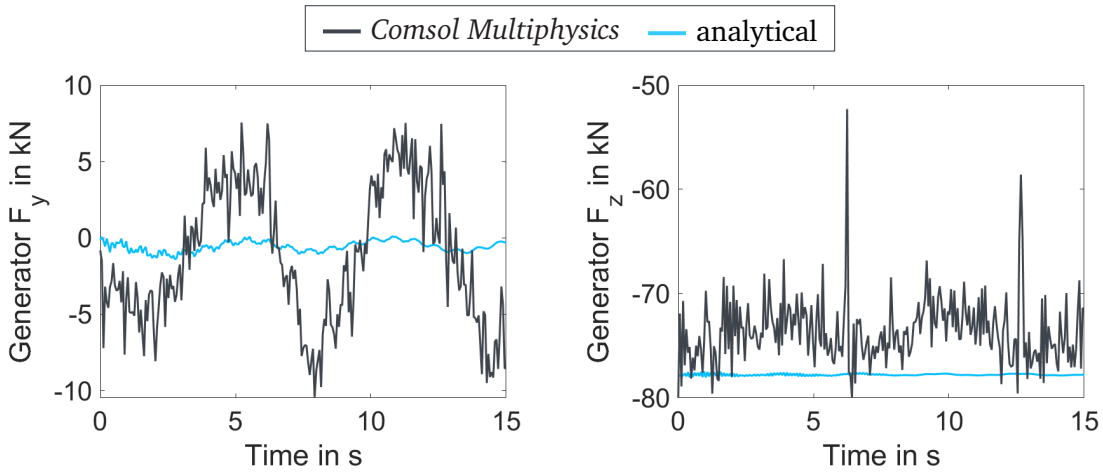

(a) y-direction **(b)** z-direction

Figure 5.1.: Comparison of the forces calculated by the high fidelity FEM solver *Comsol Multiphysics* (dark grey) and the analytical model (light blue) under eccentricity in (a) y-direction and (b) z-direction of the non-rotating coordinate system at the generator centre in a fully coupled WT simulation with uniform wind of 10m/s.

First, the uniform inflow with a constant wind speed of 10 m/s is analysed. Figure 5.1 shows the comparison of the electromagnetic forces calculated by the two models. The calculated generator forces have the same magnitude for the analytical and FEM models for both directions. However, the FEM model shows significantly higher fluctuations. This is consistent with the results seen in Section 4.2.3. High-frequency oscillations, though, reduce due to the communication interval between the MB WT model and the FEM generator model, compared to the stand-alone solution. The analytical model represents the mean force over one period of imprinted current, whereas the FEM model provides the transient, instantaneous values. This difference leads to the higher fluctuations in the FEM model. Besides the oscillations, the force in y-direction shows the impact of the numerical meshing error, leading to higher absolute forces for the FEM model. The force in z-direction confirms the conservative behaviour of the analytical model, leading to lower absolute forces for the FEM model. In summary, the comparison confirms the findings of Section 4.2.3 also for fully coupled simulations including the dynamics of the WT.

Figure 5.2 shows the calculated reactions at the bearing, i.e. forces and displacements.

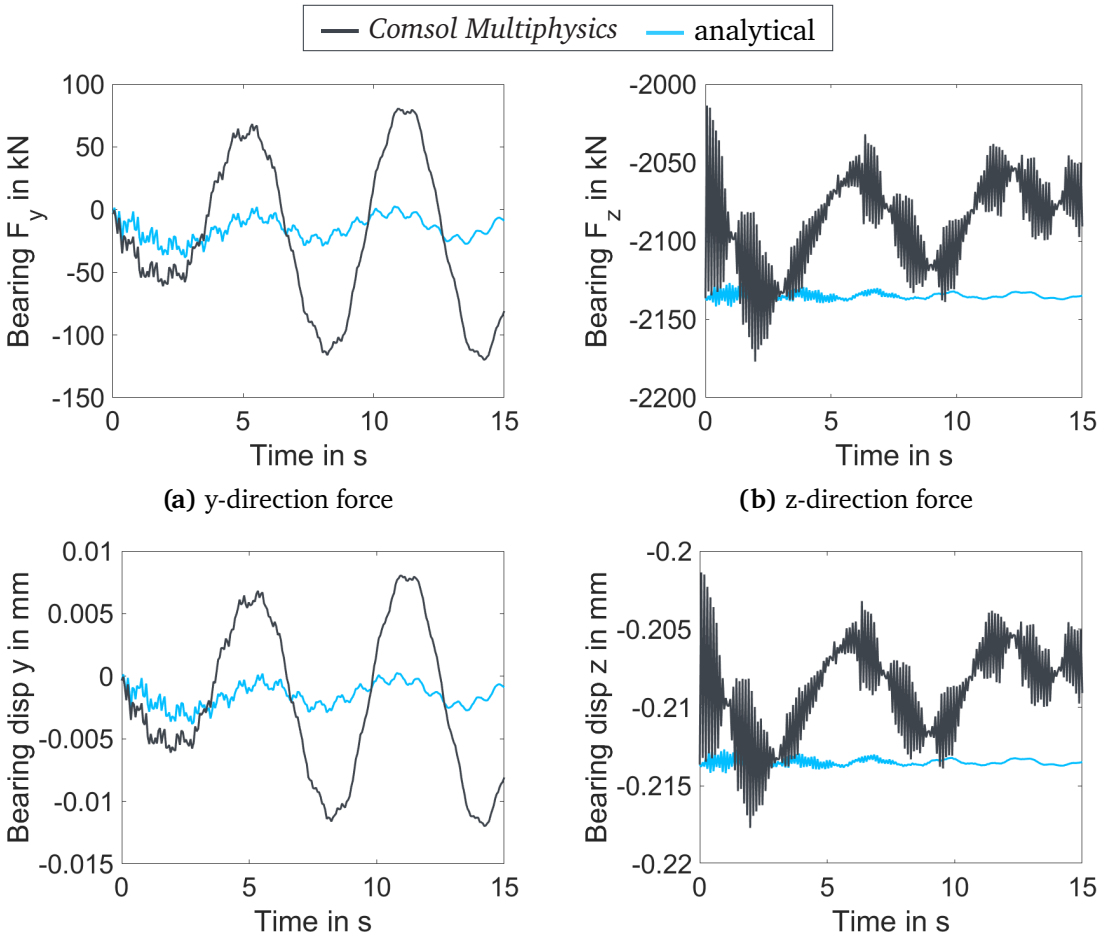

(a) y-direction force

(b) z-direction force

(c) y-direction displacement

(d) z-direction displacement

Figure 5.2.: Comparison of the forces and displacements at the bearing using the high fidelity FEM solver *Comsol Multiphysics* (dark grey) or the analytical model (light blue) in (a) and (c) in y-direction and in (b) and (d) in z-direction of the non-rotating coordinate system at the generator centre in a fully coupled WT simulation with uniform wind of 10m/s.

The graphs in (a) and (b) visualise the restoring forces of the bearing. The plots of (c) and (d) show the displacements of the generator in y and z direction from the neutral position, where bearing forces would be zero. For all sensors, the FEM and the analytical model have the same magnitude. However, the effects of the higher fluctuations of the FEM generator model can be seen in the bearing reaction forces. Especially in y-direction (plots (a) and (c)), a significant increase in amplitude can be observed. Peak to peak, the low frequency oscillation has a period of about 5 s, i.e. 0.2 Hz. This corresponds to the first SS frequency and indicates that the FEM model shows an excitation of a system mode, which does not occur in the analytical model. Considering the differences of the generator forces in y-direction, the increased displacement in this direction is assumed to be the reaction.

In z-direction, a high frequency oscillation can be seen, which is overlaid to a base frequency that again is close to the first tower frequency. The movement in z-direction can only couple to the FA modes. Here, the decreased generator force in z-direction can be the cause for the decreased displacement in this direction.

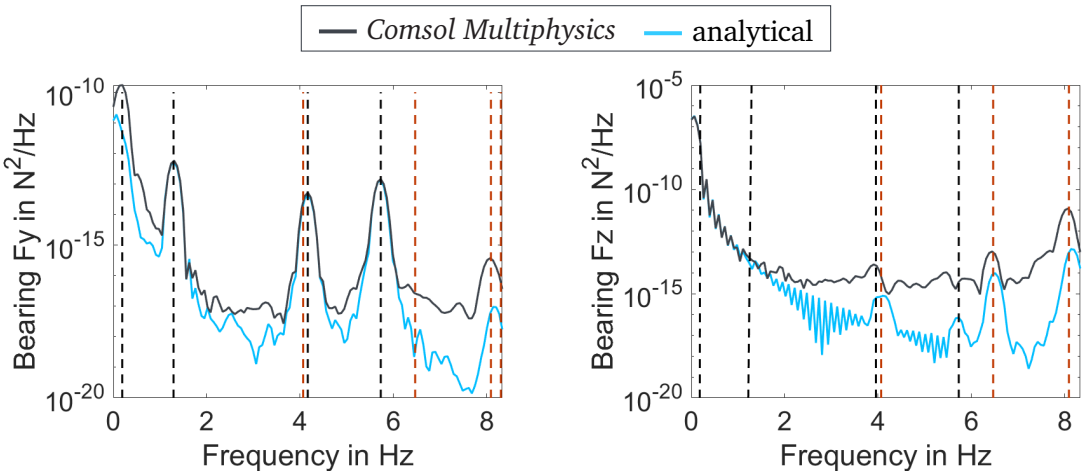

(a) y-direction **(b)** z-direction

Figure 5.3.: Comparison of the frequency spectra of the bearing forces (a) in y-direction and (b) in z-direction of the non-rotating coordinate system at the generator centre in a fully coupled WT simulation with uniform wind of 10 m/s, using the high fidelity FEM solver *Comsol Multiphysics* (dark grey) and the analytical model (light blue). The vertical lines mark expected system frequencies (black lines from left to right: first and second SS frequency, the first monopile bending frequency and the first MT frequency; red lines (expected aliasing frequencies) from left to right: frequency of the electrical field of 12.6 Hz, the second monopile bending mode at 10.2 Hz and the bearing frequencies in z-direction of 41.91 Hz and in y-direction of 50.03 Hz).

To identify the frequencies in the bearing forces, the frequency spectra of the signals are derived and given in Figure 5.3. The natural frequencies of the system modes in this range (black) and potential aliasing frequencies (red) are marked with vertical dashed lines. The black lines from left to right mark the frequencies of the first SS mode, the second SS mode, the first monopile side-to-side mode and the first MT mode. The aliasing frequencies result from frequencies above half of the communication frequency with the generator of 16.67 Hz. From left to right the red lines mark the aliasing frequency of the electrical field (12.6 Hz aliasing to 4.1 Hz), the second monopile side-to-side frequency (10.2 Hz aliasing to 6.5 Hz) and the bearing mode frequencies (41.9 Hz and 50.03 Hz aliasing to 8.1 Hz and 8.3 Hz).

In y-direction, the tower and monopile frequencies in both models are clearly present. As expected from the time series analysis, the first SS frequency of 0.19 Hz is highly visible in the *Comsol Multiphysics* model and less in the analytical model. The aliasing frequencies at

above 8 Hz, which correspond to the bearing mode frequencies of 41.91 Hz and 50.03 Hz are present in the spectra. The electrical field frequency is close to the first monopile bending mode around 4 Hz and for the peak around these frequencies it can not be distinguished where it comes from.

The peaks of the frequencies, seen in y-direction, are less prominent in the analytical model in z-direction and not present in the results using the *Comsol Multiphysics* model. At about 6.5 Hz a frequency peak can be found in the spectrum, which does not occur in y-direction and corresponds to the aliasing frequency of the FA bending mode at 10.2 Hz of the tower-monopile assembly. This frequency could explain the higher order fluctuations visible in the bearing force in z-direction.

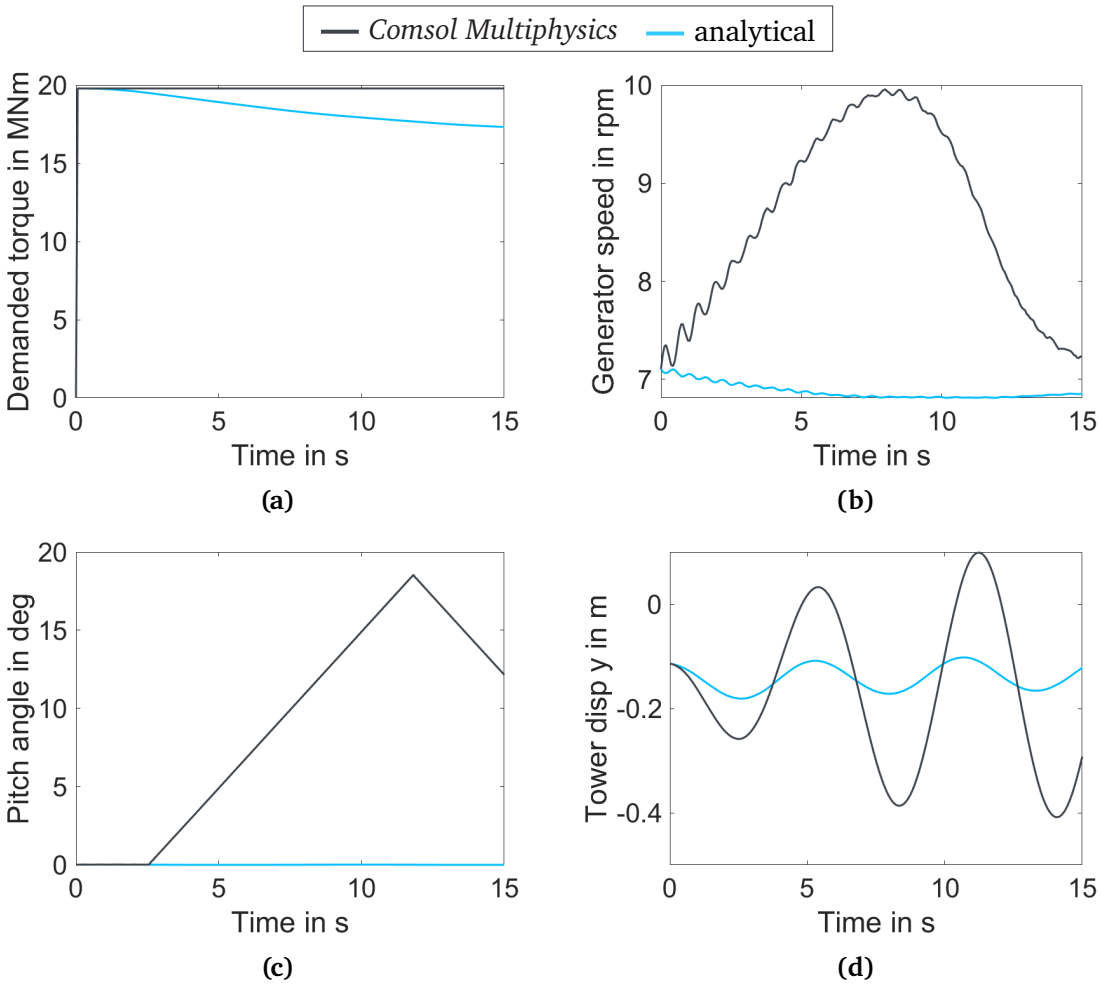

Figure 5.4.: Comparison of the WT dynamic reaction based on (a) the controller demanded torque, (b) the resulting generator rotational speed, (c) the blade pitch command and (d) the tower top displacement in crosswind direction, calculated with the high fidelity FEM solver *Comsol Multiphysics* (dark grey) and the analytical model (light blue) in a fully coupled WT simulation with uniform wind with a wind speed of 10m/s.

Knowing the behaviour of the generator and bearing forces, their impact on the WT components is studied. Figure 5.4 visualises the dynamic WT reaction. Figure 5.4 (a) and (c) display the controller behaviour based on demanded torque and pitch. Figure 5.4 (b) and (d) illustrate the WT's dynamic reaction for generator rotational speed and tower top SS displacement. The initial conditions clearly match and for the first one to two seconds, the results for pitch, torque, and tower top displacement are similar. However, the *Comsol Multiphysics* based simulation increases the rotational speed from the beginning of the simulation, running into over speed. The controller pushes the rotational speed back to the nominal speed only shortly before the end of the simulation. By then, pitch angle and torque differ significantly from the results using the analytical model. Checks of the aerodynamic torque show that the results of the analytical and FEM model are similar and can not explain the over speed, as they are lower than the generator torque. Therefore, the over speed is assumed to be a numerical transient without physical explanation.

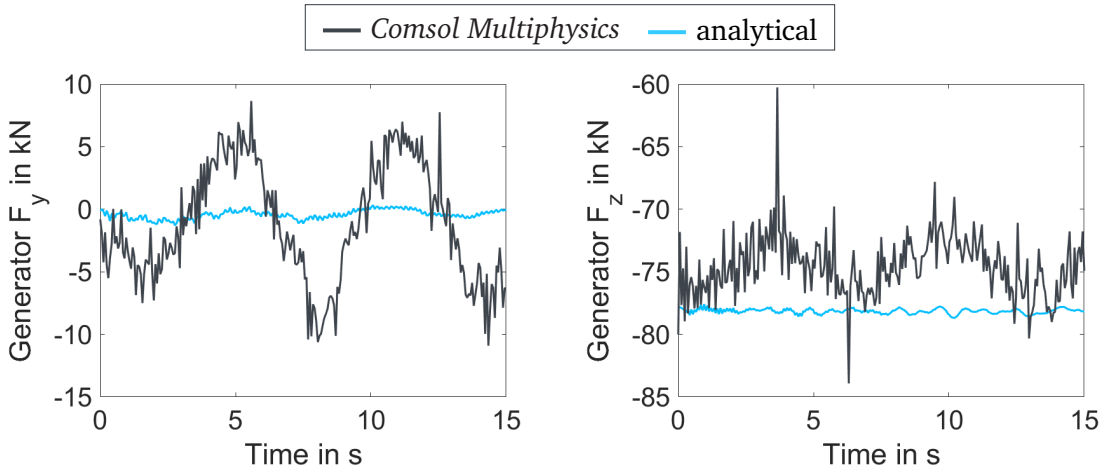

(a) y-direction **(b)** z-direction

Figure 5.5.: Comparison of the forces calculated by the high fidelity FEM solver *Comsol Multiphysics* (dark grey) and the analytical model (light blue) under eccentricity (a) in y-direction and (b) in z-direction of the non-rotating coordinate system at the generator centre in a fully coupled WT simulation with turbulent wind with a mean wind speed of 10 m/s and normal turbulence model for class A1.

Besides the over speed, the results show the excitation of the SS mode by the *Comsol Multiphysics* model with increasing amplitude. The increased eccentricity in y-direction, that is caused by the numerical error of the generator force in this direction coming from the FEM model, can explain the increasing tower displacement in the first 2 s. The high rotor assembly mass leads to a high tower top moment, even for small displacements. At the local minimum of the tower displacement after 2 s, the pitching starts. This leads to

the assumption that the interaction with the controller and the transients of the rotational speed excite the tower side-to-side mode, causing the increase of the amplitude of tower top displacement after 2s.

All in all, the analysis of the WT reaction shows that the initial conditions can not avoid numerical transient effects and the resulting transients are as long as the simulated 15 s. Therefore, the comparison of the impact of the couplings on WT loading would require longer simulations, requiring higher computational power.

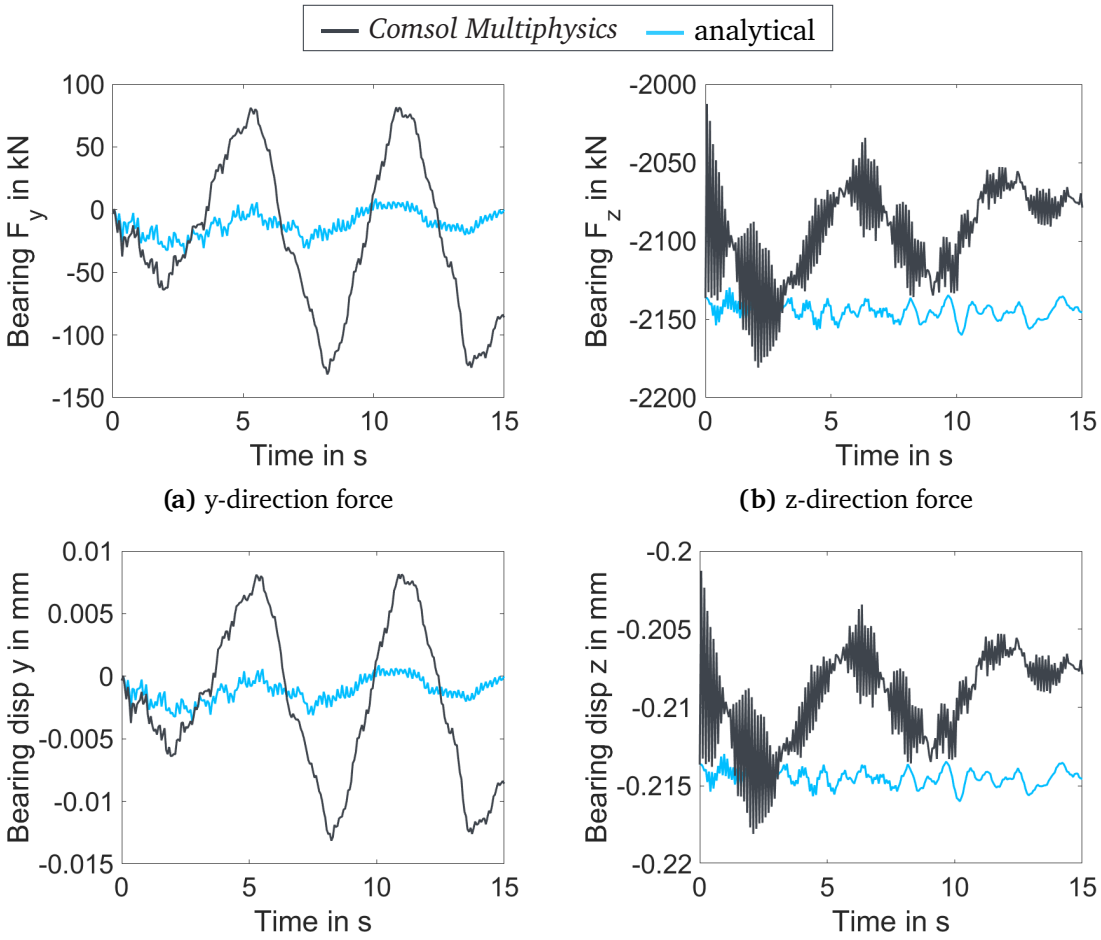

(a) y-direction force

(b) z-direction force

(c) y-direction displacement

(d) z-direction displacement

Figure 5.6.: Comparison of the forces and displacements at the bearing using the high fidelity FEM solver *Comsol Multiphysics* (dark grey) or the analytical model (light blue) in (a) and (c) in y-direction and in (b) and (d) in z-direction of the non-rotating coordinate system at the generator centre in a fully coupled WT simulation with turbulent wind with a mean wind speed of 10 m/s and normal turbulence model for class A1.

Uniform wind inflow does not occur under real operating conditions. To check whether the system behaviour remains comparable under more realistic conditions, turbulent inflow has to be used. Figure 5.5 shows the comparison of the electromagnetic forces calculated by the

two models using a wind field with 10 m/s mean wind speed and normal turbulence for WT class A1 according to the IEC standard. The time series of the generator forces is similar to the one with uniform inflow. Only the amplitude of the higher frequency fluctuations increases.

Looking at the reaction forces at the bearing (cf. Figure 5.6), similar behaviour can be observed for turbulent and uniform wind fields. This is also proven by the WT reaction, shown in Figure 5.7.

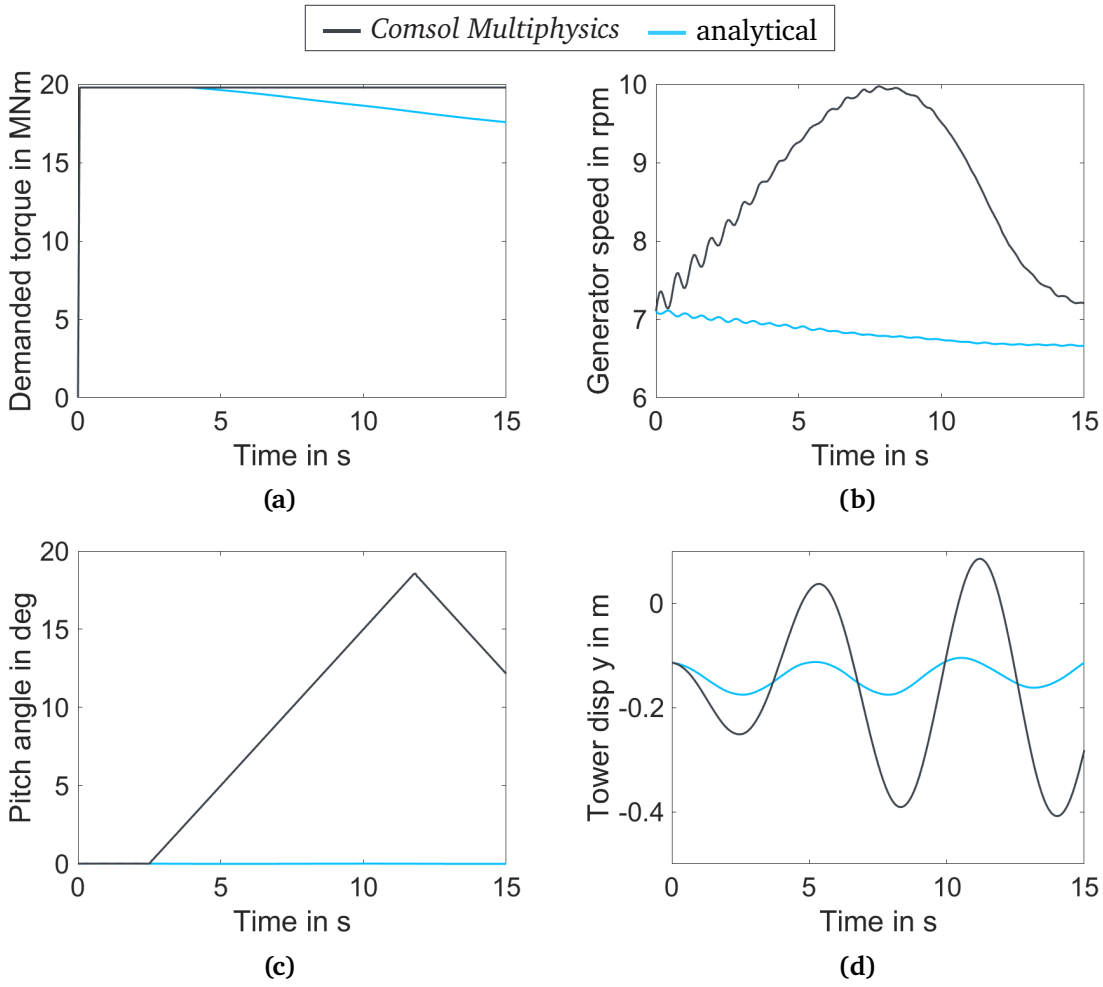

Figure 5.7.: Comparison of the WT dynamic reaction based on (a) the controller demanded torque, (b) the resulting generator rotational speed, (c) the blade pitch command and (d) the tower top displacement in crosswind direction, calculated with the high fidelity FEM solver *Comsol Multiphysics* (dark grey) and the analytical model (light blue) in a fully coupled WT simulation with turbulent wind with a mean wind speed of 10 m/s and normal turbulence model for class A1.

In consequence, it can be assumed that normal turbulence affects the forces in the generator only slightly during numerical transients. Furthermore, the comparison of the analytical and

the *Comsol Multiphysics* based model in fully coupled, dynamic WT simulations showed that both models lead to similar magnitudes of electromagnetic forces. The numerical meshing error leads to SS excitations and for future analyses, a reduction of the meshing error is recommended. The high frequency interactions of the FEM model, though, can not be captured correctly by the analytical model. To capture the high frequency components, the analytical model needs to be adapted, which is out of scope of this work. It can be concluded that the analytical model provides a good representation of the generator forces to study the EmeIs in general. Once the interactions are identified, their sensitivity to higher frequency interactions with the electromagnetic field may become of interest. Besides a high fidelity FEM model, improvements on the analytical model can be an alternative for such investigations in future work.

5.2. Study setup

Knowing now the capabilities and limitations of the analytical model for electromagnetic forces, it is used to investigate EmeIs in WTs. To understand the complex physical connections, an extensive parameter study is conducted. The investigated parameter space and evaluation methods need to be defined prior to the study, in order to address the RQs. This section summarises the aspects that need to be considered to set up the parameter study. First, Section 5.2.1 outlines the investigated parameters and their value range. Second, Section 5.2.2 explains the used evaluation methods.

5.2.1. Parameter space

The parameter study needs to consider two aspects. First, the operating range of the WT over different wind speeds needs to be covered. Second, the influence of the parameters, i.e. BS and assembly eccentricity, has to be analysed. Moreover, the unchanged parameters and components need to be specified. An overview of the definitions made in this study is outlined in the following.

First, the simulation settings are summarised: The study is based on 600 s simulations using turbulent wind with extreme turbulence model. To account for numerical transients, the total simulation time is 650 s and the first 50 s are removed. The *TurbSim* [87] wind fields

used, are periodic, which means they repeat after 600 s.

The WT operation ranges from 3 m/s cut-in wind speed up to 25 m/s cut-out wind speed. Extreme turbulence leads to wind fields with high amplitudes of wind speed oscillation. Therefore, to cover the operating range, the chosen mean wind speeds of the turbulent wind fields are 6 m/s to 20 m/s. To reduce the number of simulations, the wind speeds bin size is 2 m/s. The extreme turbulence according to the International Electrotechnical Commission (IEC) standard 61400-1 [88] for WT class 1 and a site of class A with the Extreme turbulence model (ETM) is used. It is expected that this will provoke more extreme EmeIs, which are easier to recognize.

EmeIs are expected to be caused by radial eccentricity of the generator, which is a reaction to unbalanced forces in the bearings. Besides excitations from the wind, one possible reason for such unbalanced forces could be Blade imbalance (BI). Possible influences of such an excitation are studied in this work, making one blade 10 % heavier by scaling the mass of the blade equally over all sections. Again, an extreme value is chosen to ease the detection of interactions.

The controller is an important part of the WT to ensure a safe operation and avoid excessive vibrations. This is achieved by tuning the controller gains on the WT simulation model. In this work, though, the intention is, to find possible interactions and resonances. Therefore, the reference controller, tuned based on the state-of-the-art model, will not be changed in this work. The understanding gained in this work may be the basis to retune the controller in future work.

For the choice of the BS, a first estimation of the stiffness range can be determined by the mass of the WT rotor assembly and the generator rotor. This is a constant load that the bearings have to carry. The WT's rotor assembly weighs 274.9 t and the generator rotor 151.8 t. This means, the two bearings need to carry together 4.186 MN. By design, the maximum radial eccentricity of the generator is 2 mm. Assuming, that the gravity loading should cause only a maximum of 10 % of this eccentricity, the two bearings need to have a BS of 10.465 GN/m each. To study the influence of the BS, this parameter is varied from 3 to 60 GN/m. The influence on the maximum radial eccentricity occurring in dynamic simulations with turbulent wind under consideration of the electromagnetic field are shown in Figure 5.8. The increase of the maximum radial eccentricity is non-linear. This results

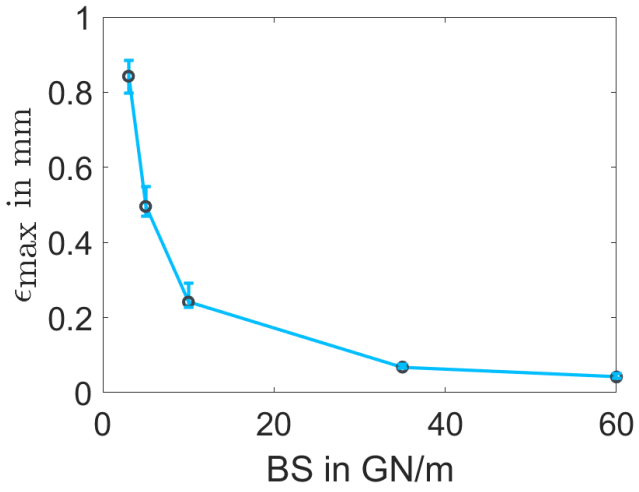

Figure 5.8.: Maximum occurring eccentricity in the generator depending on the chosen BS as mean value (circle) and with the spread (bars) for varying assembly eccentricity, BI and wind speeds.

out of the dependency of $\epsilon = \frac{F}{C}$, when the force causing the eccentricity stays constant, and the BS is increasing. Air gap closing occurred for a BS of 1 GN/m per bearing. For high stiffnesses, above 60 GN/m per bearing, the maximum eccentricity barely changes. The parameter variation of the BS per bearing in this study is $C \in [3, 5, 10, 35, 60]$ GN/m. The non-equidistant distribution of the values accounts for the non-linear relationship between BS and eccentricity.

When assembling the generator, the eccentricity can be influenced by the assembly tolerance. This may affect the maximum radial eccentricity. In this work, the influence of an assembly tolerance of 5 % of the maximum allowable radial eccentricity is investigated and compared to an ideal assembly. For the y-direction, the direction of misalignment is not expected to influence the interactions. For the z-direction, a negative assembly eccentricity increases the eccentricity caused by gravity, while a positive assembly eccentricity decreases it. Therefore, in y-direction a positive misalignment and in z-direction a negative misalignment are investigated.

All parameters defining the parameter space of this work and the simulation setup are summarised in Table 5.1.

A first impression of the impact of the different parameters is gained with the analysis of their influence on the maximum radial eccentricity. Figure 5.8 shows that the BS has a high impact to the maximum eccentricity. Figure 5.9 visualises the impact of the mean

Table 5.1.: Summary of investigated parameter space and simulation setup

Parameter	Value	Unit
simulation time	650	s
pre-simulation time	50	s
usable simulation time	600	s
wind speed range	6:2:20	m/s
BI factor for blade 1	1 or 1.1	-
BS per bearing	3,5,10,35,60	GN/m
assembly eccentricity in y-direction	0 or 0.1	mm
assembly eccentricity in z-direction	0 or -0.1	mm

wind speeds (v), the BI and the assembly eccentricities (ϵ_y and ϵ_z). In general, all these

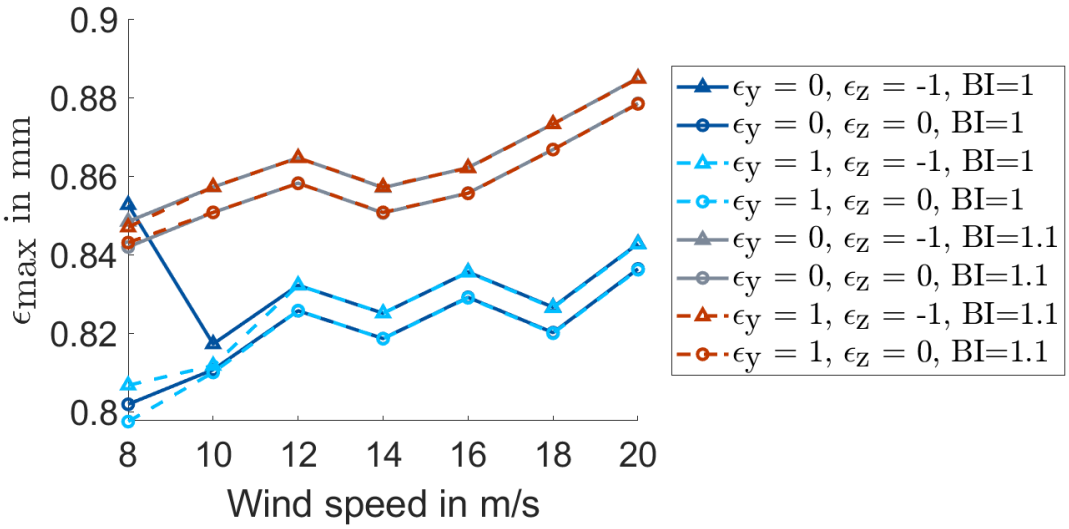

Figure 5.9.: Influence of wind speed, BI and constant eccentricity (ϵ_y and ϵ_z) due to assembly tolerance on the occurring maximum eccentricity in dynamic operation under turbulent wind conditions.

parameters have less impact on the maximum eccentricity than the BS, comparing the eccentricity in Figure 5.8, which ranges from 0 to 1 mm and the eccentricity in Figure 5.9, which ranges from 0.8 to 0.9 mm. Nevertheless, all these parameters increase the maximum radial eccentricity if their value increases. The highest impact is caused by the BI, as the upper four curves (red and grey) all include BI, whereas the lower four (light and dark blue) have no BI. The wind speed is the second dominant factor. The assembly eccentricity is only of minor importance. In z-direction, where the gravity load already leads to a static eccentricity, the impact is visible. In both groups of four curves, the upper two (triangles) include constant eccentricity due to assembly tolerance in z-direction, the lower two (circles)

do not. In y-direction, the impact is insignificant. The dashed lines including eccentricity in y-direction overlap with the solid lines, which do not include constant eccentricity in y-direction for most of the parameter combinations. Only for the lowest wind speeds, below 10 m/s, an impact of ϵ_y can be found. In consequence, the assembly eccentricity in this range is only relevant for the maximum eccentricity if other factors have already caused an eccentricity.

5.2.2. Evaluation methods

To answer the RQs according to Chapter 2, evaluation methods are needed to analyse the simulations. Three categories are used for the evaluation: frequency spectra, statistical analysis and the direct comparison of time series.

To obtain detailed information on the spectral content of a time series, an FFT is performed on the time series. This allows the identification of natural frequencies of the system and the excitation frequencies. Conducting an FFT in different subsystems, e.g. drive-train and tower can reveal interactions between the subsystems, when natural frequencies of one subsystem appear in the spectrum of the other subsystem.

In a statistical analysis, the mean, minimum, and maximum value together with the standard deviation are calculated. Another measure, frequently used, is the 1 Hz Damage equivalent load (DEL) [27, p.240]. It describes a constant amplitude harmonic load of 1 Hz that causes damage that is equivalent to the damage caused by the analysed load time series. The comparison of the DEL of two different time series gives a clear indication of the relation of the severity of the loads. The calculation is based on the Rainflow Counting method [89] and the linear damage accumulation law, given by Equation (5.1).

$$\mathrm{DEL} = \sqrt[k]{\sum_{i=1}^{N} \hat{\hat{S}}_i^k \cdot \frac{N_{\mathrm{cy},i}}{N_{\mathrm{cy,max}}}} \tag{5.1}$$

It finds load cycles of different stress amplitudes $\hat{\hat{S}}_i$ and bins them into N bins. For each bin, the number of occurring cycles $N_{\mathrm{cy},i}$ is counted and divided by the number of 1-Hz-cycles $N_{\mathrm{cy,max}}$, the time series would have. The material defines the Wöhler exponent k. In this work, the values of $k = 4$ for the tower and $k = 10$ for the blades are used.

Besides the analysis of component interactions and long-term influences also short-term dynamic effects are of interest in this study. For this purpose, the time series are compared and the differences between them are quantified using the Root mean square difference (RMSD). The RMSD assumes one time series as reference and evaluates the difference of the other to this reference according to Equation (5.2).

$$\mathrm{RMSD} = \frac{\sqrt{\frac{1}{N} \cdot \sum_{i=1}^{N} (s_i - s_{i,\mathrm{base}})^2}}{P_{75}(s_{\mathrm{base}}) - P_{25}(s_{\mathrm{base}})} \tag{5.2}$$

Thereby, the difference of the value s_i of the evaluated time series at time t_i to the value $s_{i,\mathrm{base}}$ of the reference signal at the same time step is calculated. All N differences are squared, summed up and averaged over the time series length N. The error is normalised by the difference of the 75 % percentile of the reference time series $P_{75}(s_{\mathrm{base}})$ to the 25 % percentile of the same time series $P_{25}(s_{\mathrm{base}})$. The RMSD equals zero for exactly overlapping time series and increases with increasing deviations. The RMSD is always positive due to the squared differences.

The measures are applied to several sensors of the model. The OpenFAST convention of coordinate system definitions is used for the analysed sensors [36, pp. 7]. This means, the tower coordinate systems align their z-axis with the tower vertical axis and the x-axis is pointing in downwind direction. The blade root coordinate system is fixed to the blade root, with the z-axis pointing towards the blade tip and the y-axis pointing towards the trailing edge. The coordinate system at the generator aligns the x-axis with the tilted shaft axis and is rotating with the turbine rotor. For an azimuth angle of zero, the z-axis is pointing upward, aligning with the non-rotating coordinate system at the same position. All coordinate systems are right-hand coordinate systems.

5.3. Influences of the parameter space to the system characteristics

After the definition of the parameter space and the evaluation methods, a basic understanding of the influence of the parameters on the system characteristics is beneficial, before an in-depth analysis of EmeIs.

As shown in Section 4.1.2, the additional DoF in the WT model introduces new system modes with higher natural frequencies. Furthermore, the modes interact with the tower-monopile

bending and torsion modes. This section will give some general insights on how the chosen parameter space influences the system modes for the reference WT.

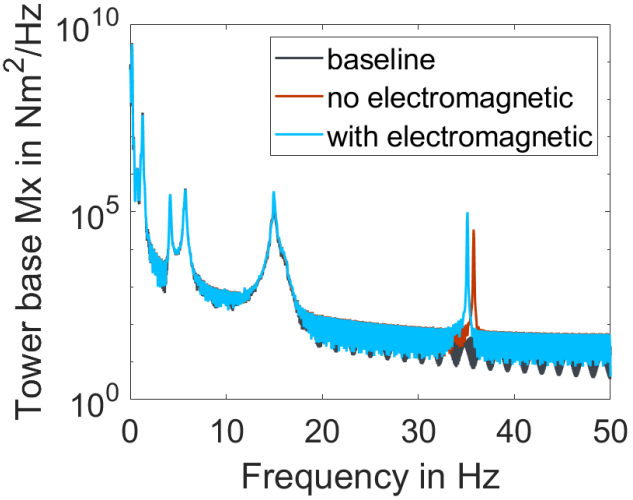

Figure 5.10.: Comparison of frequency spectra of the tower base bending moment around the x-axis for the baseline model (dark grey) to the extended model including the additional DoF with a BS of C=5 GN/m, neglecting (red) and including (light blue) the electromagnetic forces.

In the first step, the baseline model, equivalent to the state-of-the-art WT model, is compared to the extended model with the additional radial DoF in the generator (cf. Section 4.1.1). For this extended model, two fidelities are compared, the one without electromagnetic forces and the one, including electromagnetic forces. Figure 5.10 shows the frequency spectra of the tower base SS moment for these three model fidelities. From this figure, the system's natural frequencies can be identified. The comparison of the spectra shows the introduction of an additional mode with a frequency of about 35 Hz, for the extended model. The frequency of this mode decreases with the introduction of the electromagnetic forces (difference of red and blue peak above 30 Hz). It can be assumed that the electromagnetic forces act like a spring with negative stiffness.

In the next step, the influence of the parameters, describing the investigated parameter space introduced in Section 5.2.1, on the system properties is quantified. The first parameter analysed is the *BI*. The mass of one blade was increased by 10 % and the rotor assembly and the tower top mass increase accordingly. As a result, the system natural frequencies of the tower, monopile and the bearing decrease slightly. This can be seen in Figure 5.11 (a) for the bearing frequency at about 35 Hz and in (b) for the MT frequency at about 5.7 Hz, where the peaks of the light blue curve occur at 5.6 Hz and 34.75 Hz instead of 5.72 Hz and

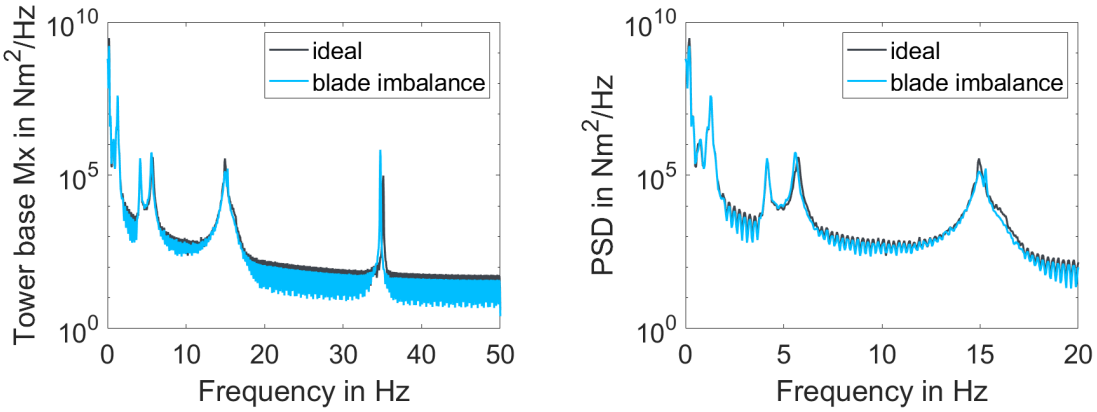

Figure 5.11.: Comparison of frequency spectra of the tower base bending moment around the x-axis for the extended model including the additional DoF with a BS of C=5 GN/m and including the electromagnetic forces: (a) for the frequency range up to 50 Hz and (b) zoomed to the frequency range up to 20 Hz.

35.11 Hz for the dark grey curve.

The *assembly eccentricity* does not show any influence to the system frequencies and therefore, no figure is shown here.

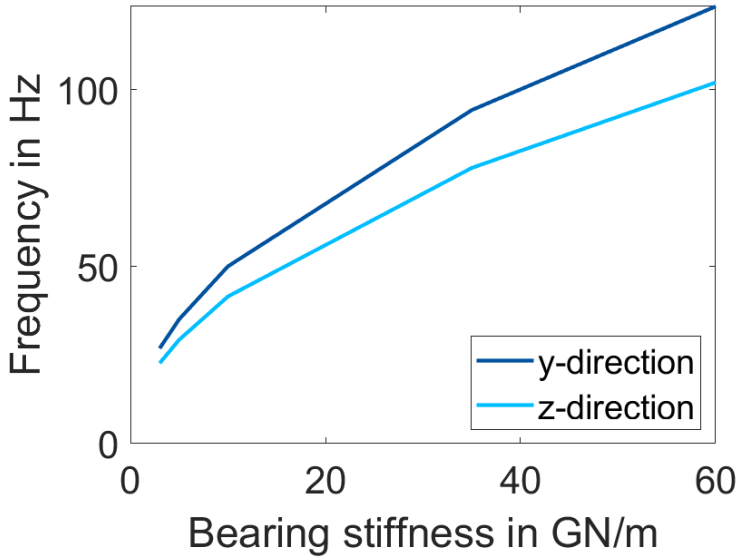

Figure 5.12.: Influence of the bearing stiffness on the natural frequencies of the bearing in y and z direction.

The *BS* influences only the natural frequency of the bearing mode, i.e. radial oscillations at the bearings. Other system modes, e.g. SS or MT mode, are not impacted. A comparison of the bearing frequencies in y- and z-direction over the BS is shown in Figure 5.12. The

difference between the curves for the frequencies in y- and z-direction results from the different coupling with the tower modes. The coupling with the MT and SS mode occurs for bearing oscillations in y-direction, while the z-direction couples only with the FA mode.

All in all, the BS has the highest impact to the natural frequency of the bearing mode. A summary of the system natural frequencies for the different parameter combinations is given in Table 5.2.

Table 5.2.: Summary of the influences, the investigated parameter combinations of varying BS C, including (+) and excluding (-) BI and including (+) and excluding (-) electromagnetic forces (Emag) have on the system natural frequencies of the bearing mode in y ($f_{B,y}$) and z-direction ($f_{B,z}$), the tower modes in SS direction ($f_{T,SS1}$ and $f_{T,SS2}$) and the monopile modes in side-to-side direction ($f_{M,SS1}$ and $f_{M,SS2}$) and MT direction ($f_{M,tor}$) in the coupled WT system.

Parameter combination			System natural frequencies in Hz						
	BI	Emag	$f_{B,y}$	$f_{B,z}$	$f_{T,SS1}$	$f_{T,SS2}$	$f_{M,SS1}$	$f_{M,SS2}$	$f_{M,tor}$
baseline	+		/	/	0.18	1.28	4.17	14.98	5.60
	-		/	/	0.18	1.29	4.17	14.99	5.72
C=3 $\frac{GN}{m}$	+	+	26.63	22.43	0.18	1.28	4.17	14.98	5.60
		-	27.48	23.08	0.18	1.28	4.17	14.98	5.60
	-	+	26.91	22.70	0.18	1.29	4.17	14.94	5.72
		-	27.74	23.37	0.18	1.29	4.17	14.94	5.72
C=5 $\frac{GN}{m}$	+	+	34.75	28.90	0.18	1.28	4.17	14.98	5.60
		-	35.40	29.47	0.18	1.28	4.17	14.98	5.60
	-	+	35.11	29.31	0.18	1.29	4.17	14.94	5.72
		-	35.75	29.86	0.18	1.29	4.17	14.94	5.72
C=10 $\frac{GN}{m}$	+	+	49.59	40.96	0.18	1.28	4.17	14.98	5.60
		-	50.07	41.32	0.18	1.28	4.17	14.98	5.60
	-	+	50.03	41.55	0.18	1.29	4.17	14.94	5.72
		-	50.52	41.91	0.18	1.29	4.17	14.94	5.72
C=35 $\frac{GN}{m}$	+	+	93.23	76.74	0.18	1.28	4.17	14.98	5.60
		-	93.50	76.95	0.18	1.28	4.17	14.98	5.60
	-	+	94.17	77.85	0.18	1.29	4.17	14.94	5.72
		-	94.41	78.06	0.18	1.29	4.17	14.94	5.72
C=60 $\frac{GN}{m}$	+	+	122.22	100.54	0.18	1.28	4.17	14.98	5.60
		-	122.42	100.70	0.18	1.28	4.17	14.98	5.60
	-	+	123.40	101.95	0.18	1.29	4.17	14.94	5.72
		-	123.58	102.10	0.18	1.29	4.17	14.94	5.72

5.4. Interactions of the electro-mechanical model with the aerodynamics

EmeIs can only lead to interactions with the aerodynamics if the WT rotor is affected in its position and velocity relative to the wind inflow. To investigate the interactions of the WT

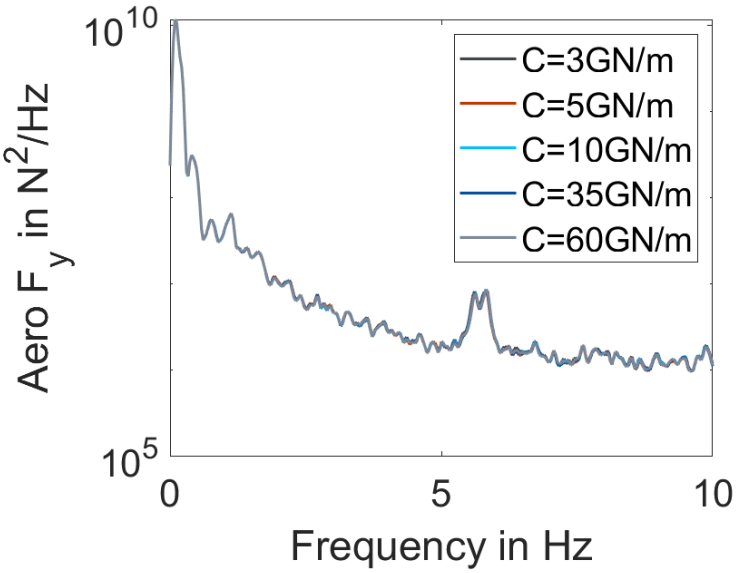

Figure 5.13.: Comparison of frequency spectra of the horizontal summary force in y-direction of the aerodynamic solver for different BSs for the frequency range up to 10 Hz.

with the inflow, the aerodynamic forces calculated by the aerodynamic solver are analysed. Specifically, the horizontal total force at the hub centre in y-direction of a rotating coordinate system is used for a spectral analysis. This force is directly acting in the radial direction of the bearing.

The spectral analysis of different BSs in the electro-mechanical model is given in Figure 5.13 for the frequency range up to 10 Hz. From this plot, a double peak around 5.7 Hz is visible. The mean value of both peaks is the MT frequency. The distance of the two peaks is twice the mean rotational speed, and they are located left and right of the 5.7 Hz. The reason for two peaks instead of one is that forces, acting in one direction in a non-rotating coordinate system of the bearings, lead to an oscillating force in the rotating coordinate system of the blades. The rotating force equals the product of the non-rotating force with $\cos(2\pi\omega t)$. The double peak indicates that the MT oscillation affects the relative position of the blades to the inflow so that the aerodynamic forces at the blades change.

In Section 4.1.3, the communication time step with the aerodynamic solver was chosen

with 0.02 s, based on the state-of-the-art WT model. However, considering the natural frequencies of the bearing being between 25 Hz and 125 Hz, this assumption needs to be reviewed for the detailed model as the communication interval could lead to aliasing effects.

To be above the aliasing frequency of all BSs, the communication interval needs to be double or more of the maximum frequency. For the investigated BS, this means a minimum communication frequency of 250 Hz, which equals a communication interval of 0.004 s. In this case, the aerodynamic solver (*AeroDyn*) receives two values per period of the high frequency fluctuation from *Simpack*. To be numerically more conservative, but also computationally more expensive, a communication interval of 0.0008 s is also tested. This equals ten times the highest bearing frequency, i.e. 1250 Hz.

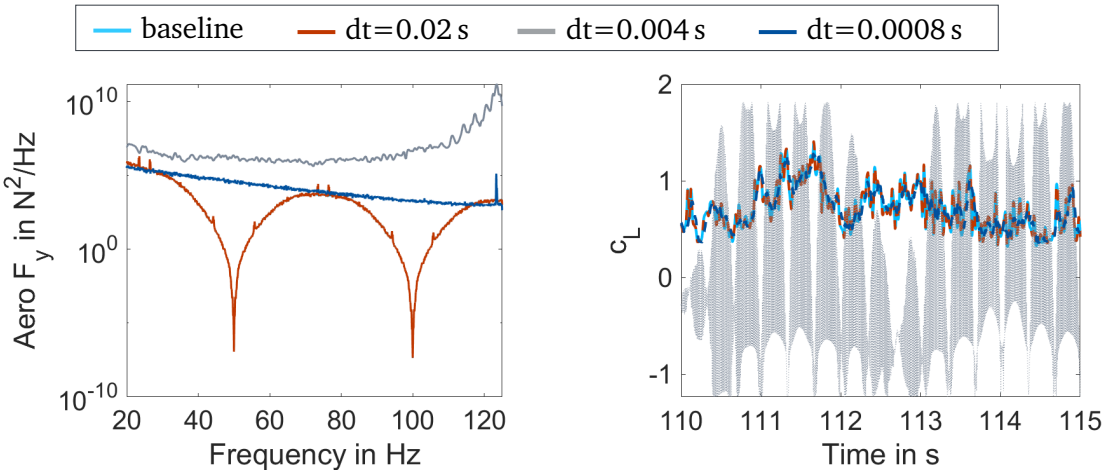

Figure 5.14.: Comparison of communication intervals to the aerodynamic solver (a) based on the frequency spectra of the aerodynamic rotor force in y-direction in the range of 20 Hz to 125 Hz and (b) based on the resulting lift coefficient at the blade section at 75 % of the blade length

A comparison of the three cases for the aerodynamic force in y-direction at the hub centre is given in Figure 5.14. Subplot (a) shows the comparison of the frequency spectra from 20 Hz to 125 Hz. The comparison shows that the communication interval of 0.02 s has two aliasing peaks around 25 Hz, i.e. 23 Hz and 27 Hz and the spectrum drops at 50 Hz and 100 Hz due to the chosen communication interval. The baseline solution (light blue) equals the 0.02 s-solution (red) and, therefore, is barely visible in the plot. When using the communication interval of 0.004 s (light grey), the peak occurs at the bearing frequency of 123 Hz. The amplitude of this peak is of the same magnitude as the low frequency

components below 20 Hz (cf. Figure 5.13). This communication interval is connected to handing over only two values per period of the bearing frequency to the aerodynamic solver. With the further decrease of the communication interval to 0.0008 s (dark blue), the peak at 123 Hz remains visible, but the amplitude drops by 6 magnitudes, from 10^{11} to 10^{5}. Thus, it appears as if the 50 Hz and the 1250 Hz communication frequency lead to comparable results, whereas the 250 Hz causes high-frequency oscillations.

In order to evaluate the differences of these solutions, the theory of unsteady aerodynamics needs to be considered. The changes of the angle of attack occur with a time delay due to inertia of the inflow [90, pp. 130]. According to [90, pp. 95] the inflow inertia limits the speed of change of the lift force and above a certain cut-off frequency it is assumed that the lift force can not react to changes, preventing any interactions at high frequencies. In this work, the default value of the unsteady aerodynamics module of *AeroDyn* for the cut-off frequency is chosen, i.e. 20 Hz. Therefore, the frequency of the bearing mode is well above the cut-off frequency for all investigated BSs, and no feedback to the aerodynamics should occur for this mode.

Thus, from the comparison of the spectra, the solution using 0.004 s should be excluded. It is assumed that the two values per period are insufficient for the unsteady aerodynamics filters to work, leading to numerical instabilities. This is supported by Figure 5.14 (b), which compares the time series of lift coefficients for the three communication intervals and the baseline model. This comparison shows that the lift coefficient for a communication interval of 0.004 s is highly fluctuating, which is not physically explainable. The other two communication intervals show solutions similar to the baseline with only minor deviations. As the computational effort of the planned parameter study is already high, the minimal computational effort for the aerodynamic solver is aimed for. Therefore, in this study, the communication interval of 0.02 s to the aerodynamic solver is used. However, future work needs to investigate this assumption in depth.

In summary, interactions can occur for the MT frequency, which is shown as a modulated peak in the aerodynamic forces (cf. Figure 5.13). Higher frequencies of the system can be excluded from interactions with the aerodynamic forces. Therefore, interactions of the EmeIs with the aerodynamics can be excluded.

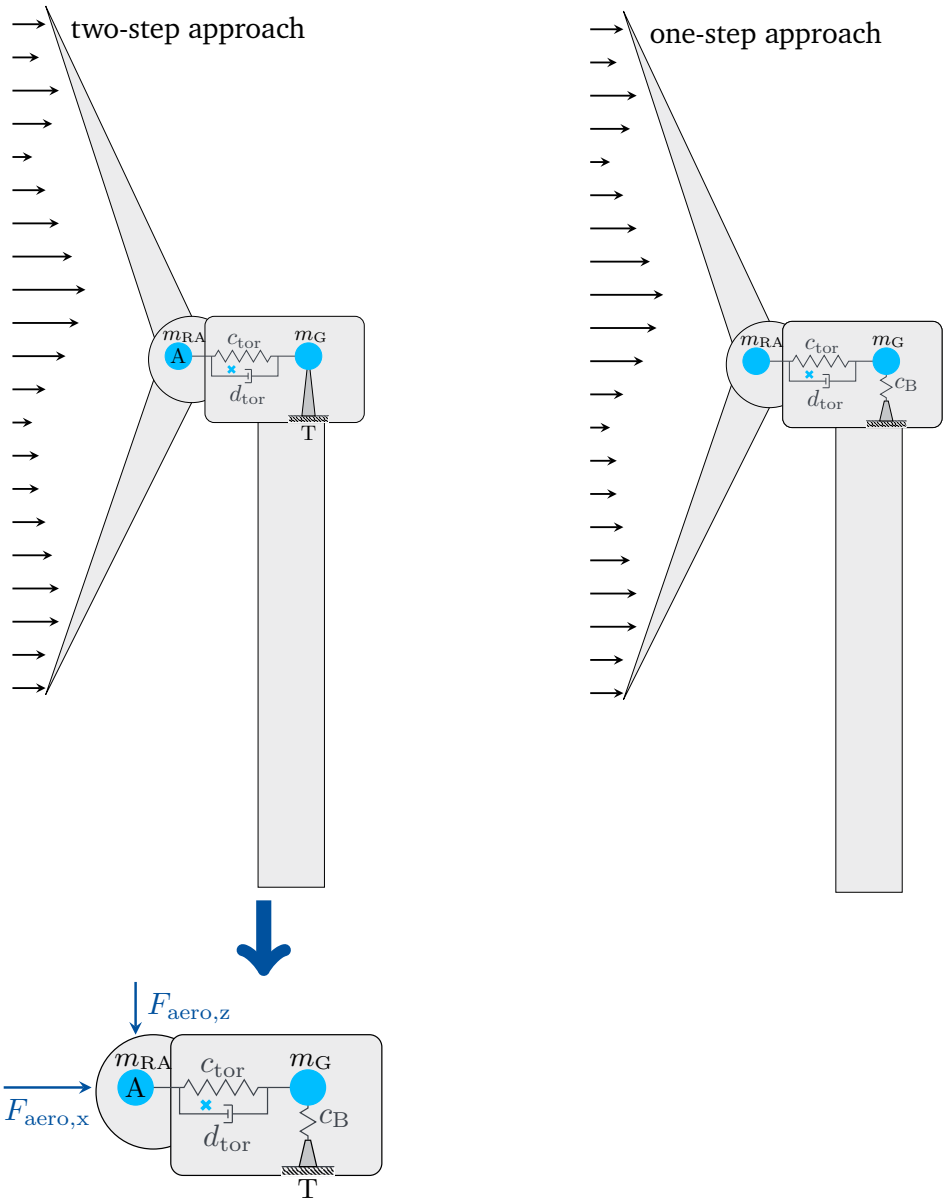

Figure 5.15.: Comparison of drive-train load calculation using (a) the state-of-the-art two-step approach and (b) the one-step approach based on the model developed in this work, including the DoF at the generator in radial direction

Traditionally, EmeIs have been investigated for drive-train design evaluation. This means, load evaluations focus on main bearing and shaft loads. To limit the computational effort for these analyses, a two-step approach is used, as shown in Figure 5.15 (a). In the first step, a state-of-the-art WT model, as the baseline model in this work, is used. With this model, the aerodynamic loads at the hub centre at point A and the tower top displacements at point

T are calculated. In the second step, a detailed model of the drive-train is used and the surrounding components of the WT are neglected. The calculated loads and displacements are imposed at the interface nodes A and T to the drive-train model. With this configuration, the load distribution within the drive-train is determined.

In [78] this approach has been checked for a 5 MW onshore WT, based on the controller signals of torque demand and pitch demand. It was concluded to be a valid approach. The WT in this work has a nominal power of 15 MW, leading to larger and heavier components. Furthermore, it includes additional components with the monopile, as it is an offshore WT. As outlined in Section 2.4, the validity of the two-step approach should be checked for larger turbines. This is done by comparing the results of the method according to literature to the results obtained with the newly developed model (cf. Section 4.1.1 and Section 4.2.1) in a one-step approach, as illustrated in Figure 5.15 (b).

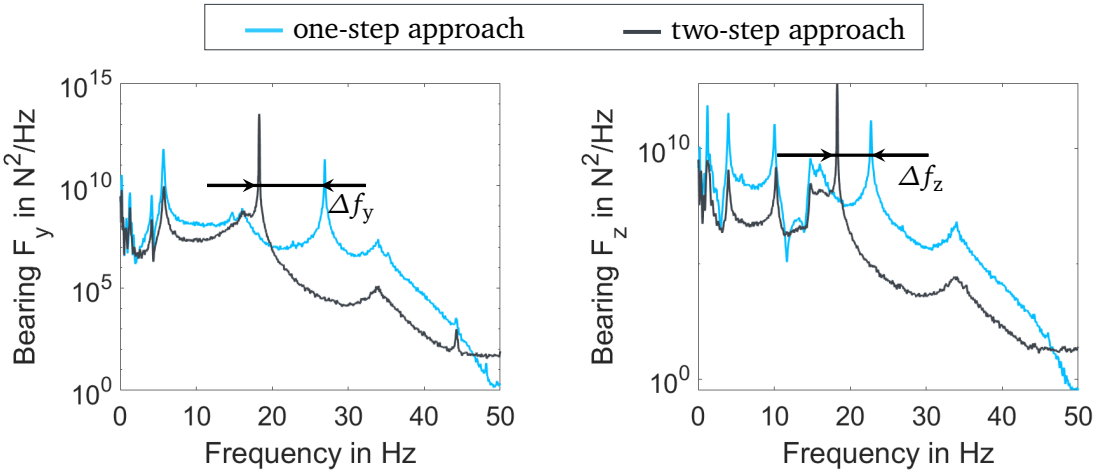

(a) y-direction **(b)** z-direction

Figure 5.16.: Comparison of frequency spectra of the bearing force (a) in y-direction and (b) in z-direction between the fully coupled WT model in a one-step approach (blue) and the state-of-the-art two-step approach (dark grey) (cf. Figure 5.15).

In Section 4.1.2, it is shown, that the DoF in the bearing leads to coupled modes in the system due to interactions with the tower and monopile modes. When using the two-step approach, these interactions can not be considered, as the main bearing is excluded from the WT simulation in the first step and the tower is excluded from the drive-train simulation in the second step. The changes to the system characteristics can be understood from the comparison of the frequency response of the bearing loads in Figure 5.16. Here, the frequency spectra of the one-step and two-step approach for a BS of C=3 GN/m are

compared. Neglecting the coupling of the modes, leads to an underestimation of the bearing frequency when comparing the peaks in both spectra between 20 Hz and 30 Hz, marked with Δf_y and Δf_z. The coupling of the mode in y-direction with the MT mode leads to a higher mismatch of the bearing frequencies than in z-direction, where the mode can only couple with bending modes of the tower. The difference between the frequencies of bearing modes increases from a minimum difference of 4.4 Hz for C=3 GN/m in z-direction to a maximum difference of 39 Hz for C=60 GN/m in y-direction. For all BSs, the mismatch in y-direction is twice the mismatch in z-direction.

To better understand the influence of the aerodynamic solver on the results, the coupling to the aerodynamic solver is switched off for the one-step approach. The aerodynamic forces in the hub centre, calculated with the baseline model (cf. Figure 5.15 (a)) for point A, are applied as excitation forces to the electro-mechanical model (cf. Figure 5.15 (b)) at the same location, while the *AeroDyn*-coupling is switched off. Thus, the influence of aerodynamic excitation and damping can be quantified by comparing the results of this approach in two steps, using a servo-elastic WT model with an additional excitation force at the hub centre, to the results of the initial approach in one step, using an aero-servo-elastic WT model. The results for the bearing force in y-direction, are shown in Figure 5.17, using the highest (C=60 GN/m) and lowest (C=3 GN/m) BS.

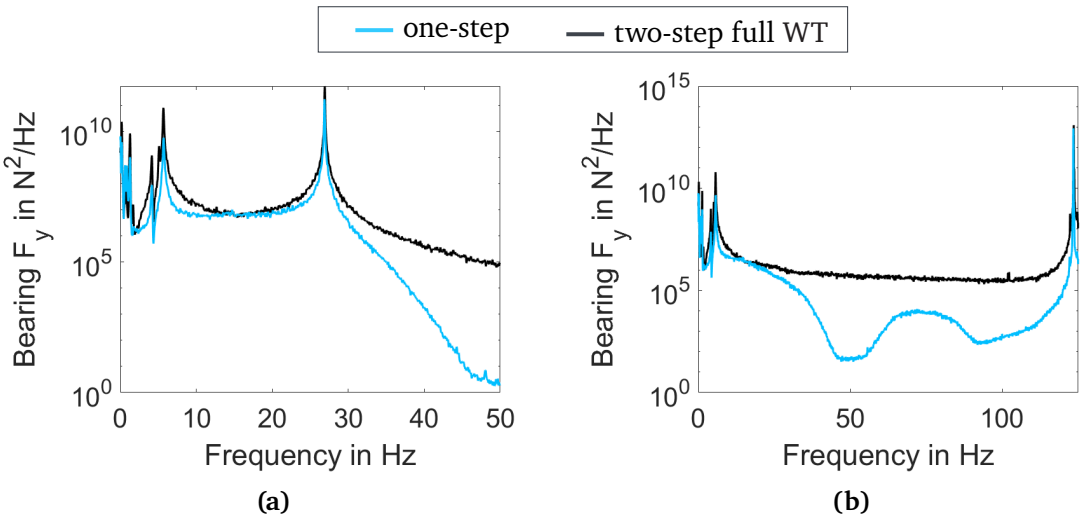

Figure 5.17.: Comparison of frequency response in the main bearings in y-direction with and without a coupled aerodynamic solver (a) for a bearing stiffness of C=3GN/m and (b) for a BS of C=60GN/m

Assuming a low BS, Figure 5.17 (a) shows a decreased amplitude of the bearing frequency

for the one-step approach. This effect is reduced for the high BS, as can be seen from Figure 5.17 (b). Here, the amplitudes of both curves around 123 Hz are equal. The intermediate BSs show a trend, reducing the difference between one-step and two-step solution with increasing BS. In addition, the amplitudes of the frequencies below 10 Hz are lower for the one-step approach than for the two-step approach. This is expected to result out of aerodynamic damping acting on blades and tower, which can not be represented with the two-step approach.

Figure 5.18 compares only the frequency spectra of the two-step approach using the full WT model for different BSs. It shows that the higher BSs lead to oscillations with a higher amplitude than those with the lower BS. These solutions could point to a mechanical resonance behaviour with increasing BS. However, no natural frequency is known above 125 Hz, and it remains unclear what could resonate.

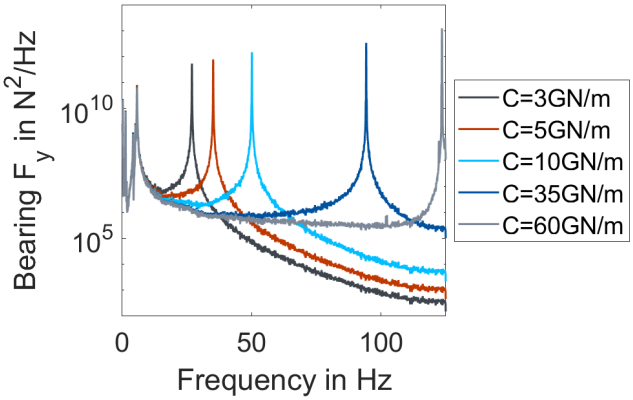

Figure 5.18.: Comparison of frequency spectra of bearing force in y-direction for different C, which are all excited with the aerodynamic loading calculated with the baseline model.

Knowing the differences of the two approaches in system natural frequencies and the influence of the aerodynamic forces on the excitation of the bearing mode, their impact on the design loads needs to be quantified. In this study, the bearing loads are compared directly, instead of the controller signals, which were used in [78]. Therefore, the equivalent dynamic bearing loads D according to Equation (5.3) are calculated [91, p. 206]. As the gravity causes a high non-rotating loading $\bar{F}$ to the bearings, a correction according to

Equation (5.4) is needed [91, p. 207].

$$D_1 = \sqrt[p]{\sum_{i=1}^{N} (F_i - \bar{F})^p \cdot \frac{\omega_i}{\bar{\omega}} \cdot \frac{\Delta t_i}{T}} \tag{5.3}$$

$$D = D_2 \cdot \left[1 + 0.5 \cdot \left(\frac{D_1}{D_2} \right)^2 \right] \qquad \text{with} \quad D_2 = \bar{F} \tag{5.4}$$

The calculation is based on the instantaneous loading F_i, the instantaneous rotational speed ω_i, the mean rotational speed $\bar{\omega}$ and the fraction of the time series $\frac{\Delta t_i}{T}$ for which these conditions are present in the system. The instantaneous loading conditions are summed over all time steps N. The exponent p is an empirical value that was chosen to be $\frac{10}{3}$ for rolling element bearings, based on literature [91, p. 206]. The analysis is conducted for two different wind speeds, with three seeds per wind speed. The BS was varied according to the parameter space of Section 5.2.1. BI and assembly tolerance have been neglected.

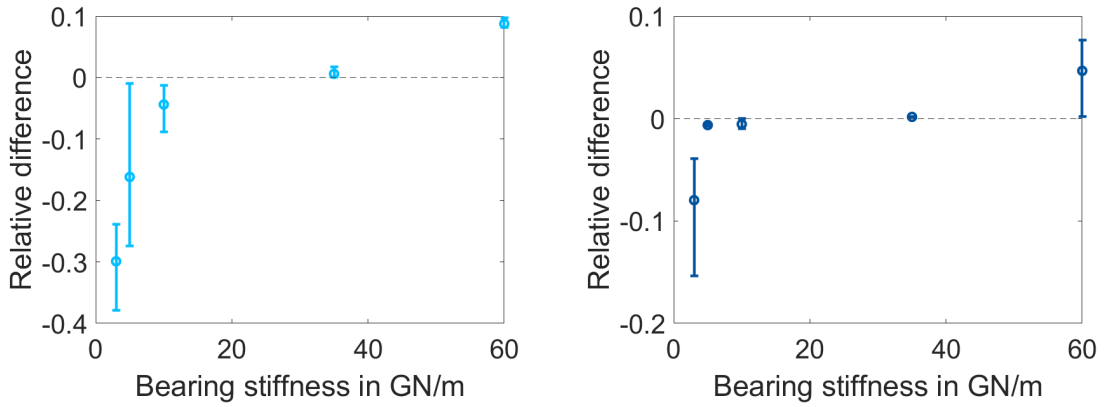

(a) 8 m/s mean wind speed **(b)** 14 m/s mean wind speed

Figure 5.19.: Relative difference of equivalent dynamic bearing loads between state-of-the-art two-step approach for calculation and one-step approach using the model developed in this work for (a) 8 m/s mean wind speed and (b) 14 m/s mean wind speed over the BS and normalised to the value of the two-step approach. Circles mark the mean over three seeds, and the error bars mark the spread of the difference over the three seeds.

Figure 5.19 (a) shows the mean relative difference of the equivalent dynamic bearing loads, marked with the circle, over the BS for 8 m/s mean wind speed. The error bars indicate the spread of the difference, as they mark the maximum and minimum difference. Figure 5.19 (b) shows the same parameter for a mean wind speed of 14 m/s. Both wind speeds (Figure 5.19 (a) and (b)) show a general trend of increasing mean values with increasing BS. This means that the equivalent dynamic bearing loads used for bearing design are underestimated for high BSs, when using the two-step approach. For low BSs, a

conservative overestimation happens with the two-step approach. For increasing BS and increasing mean wind speeds, the error bar range mostly decreases.

Section 5.4 has shown that the communication with the aerodynamic solver can lead to uncertainty in the simulation results. To exclude the coupling uncertainty from the evaluation, the two-step approach with the full WT model is used also for the load analysis. The adapted differences between the state-of-the-art two-step approach and the two-step approach using the full WT model are shown in Figure 5.20. The general trend of increasing mean values with increasing BS remains, and the mean differences generally increase. For $C = 60\,\mathrm{GN/m}$, the differences over three seeds is close to 10 %. Figure 5.18 shows the increasing intensity of the bearing mode oscillation for the increasing BS. In combination with the differences of the bearing mode frequencies (cf. Figure 5.17), this can be an explanation for the increasing relative difference of equivalent dynamic bearing loads.

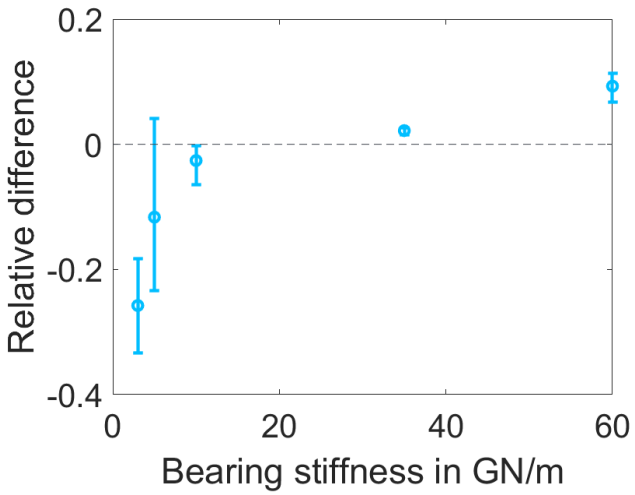

Figure 5.20.: Relative difference of equivalent dynamic bearing loads between the state-of-the-art two-step approach and a two-step approach using the full WT model in the second step, avoiding feedback into the aerodynamics for extreme turbulent inflow conditions with 8 m/s mean wind speed.

All in all, it can be expected that the introduced radial DoF and the electromagnetic forces may affect the bearing design loads. In consequence, the state-of-the-art two-step approach may be insufficient for drive-train design purposes.

5.6. Interactions with the wind turbine structure

So far, it has been shown that the WT model introduced in Section 4.1.1 coupled with the analytical model for the electromagnetic forces from Section 4.2.1 changes its dynamic behaviour compared to the baseline model. Interactions with the aerodynamic solver and impacts on the main bearing loads have been discussed. Beyond the drive-train design considerations in Section 5.5, this work aims to answer the RQ, if EmeIs can lead to changed loading of components outside the drive-train, i.e. blades and tower. Therefore, the following analysis focuses on load sensors at the blade root, the tower top and the tower bottom. Two analysis steps are required. First, possible interactions need to be identified. This is achieved through an extensive parameter study based on the defined parameter space (cf. Section 5.2.1) and the comparison of the simulation results to those of the baseline model. The results are analysed and discussed in Section 5.6.1. In the second step, it has to be checked whether the found interactions are caused by the additional, radial DoF or result from interactions of the electromagnetic forces with the dynamics of the WT. Therefore, in Section 5.6.2, a third model, including the radial DoF, but neglecting the electromagnetic forces, is included into the comparison.

5.6.1. Load analysis

To identify possible interactions of the generator with the WT system, the simulation results including the additional DoF of the drive-train and the analytical description of the electromagnetic forces are compared to the simulation results of the baseline model. This sections will focus on interactions with the control subsystem and the structural dynamics of the WT components, i.e. blades, tower, and foundation. Due to the large number of simulations, a one-to-one comparison of all simulations is not feasible. Therefore, the analysis starts with a statistical comparison over all results. Here, in the first step, only one seed for each wind speed is used. This was done due to the high computational effort. The full parameter study with one seed required 320 simulations, with four hours of simulation per parameter combination. Based on the analysis with one seed, hypotheses about the parameter influences are developed. These are tested with two more seeds per wind speed with a reduced parameter space, reducing the computational effort. After narrowing down to the results of interest, a direct comparison of the time series with the aim to understand

the causes for interactions is performed.

Controller: For the statistical comparison, the controller behaviour is investigated. Differences in the controller response would indicate a changed dynamic of the WT, caused by EmeIs. Therefore, the generator torque and blade pitch are compared and the resulting generator speed and generator power output are included into the analysis. The RMSD

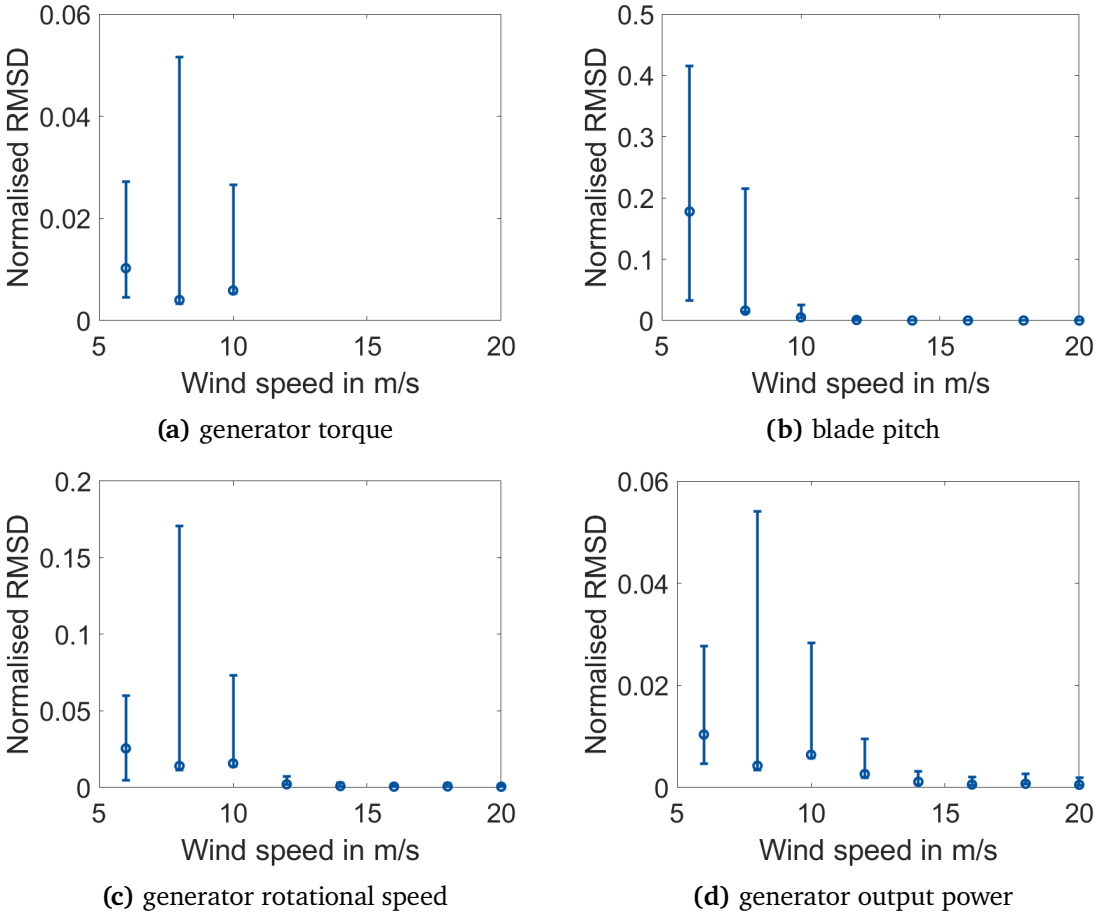

(a) generator torque

(b) blade pitch

(c) generator rotational speed

(d) generator output power

Figure 5.21.: Statistical test of controller signal differences for the full parameter space, plotting the normalised RMSD mean (circle) and extreme (upper and lower bar) values over the wind speeds with one seed per wind speed.

according to Equation (5.2) is used as measure for comparison. The baseline solution is used as reference solution. This measure is sensitive to short dynamic changes in the controller signals. The results are plotted over the mean wind speed in Figure 5.21. The circle indicates the mean value of the RMSD over all simulations with the given wind speed. The upper and lower error bars mark the minimum and maximum values that occurred. From Figure 5.21 (a) it can be seen that the RMSD of the generator torque signal for wind speeds of 12 m/s and higher are missing. This results from the behaviour of the WT above rated

wind speed (10.56 m/s), which aims to keep the torque constant. The RMSD is normalised over the difference of 25 % and 75 % percentile of the time series (cf. Equation (5.2)). In case these percentiles are equal, the RMSD is normalised over zero, leading to an infinite RMSD. This occurred for wind speeds above 12 m/s. At these wind speeds, the generator power (Figure 5.21 (d)) should be checked, as it results from the multiplication of generator torque and rotational speed (Figure 5.21 (a)+(c)). Generally, the RMSD mean value and spread decrease with increasing wind speed. The results show changes in the dynamic behaviour with implications for the controller and indications of possible EmeIs for below rated conditions.

The pitch control affects the aerodynamics, while the torque control is a mechanical system control. The aerodynamics do not show interactions with the EmeIs (see Section 5.4). The torque contributes to the tower top bending moment in side-to-side direction. Above rated, the pitch control is active, whereas below rated the torque control is active. In consequence, the results lead to the assumption that the EmeIs are mainly interacting with the torque controller.

Load statistics: In the second step, the analysis shifts towards the load sensors at the tower and the blades to check for interactions with the structural behaviour of the WT. To compare the impact on the loads, the 1-Hz-DEL, according to Equation (5.1), are used. The intensity of EmeIs, depending on the parameters of the investigated parameter space, is analysed. Results are presented, starting with the parameter wind speed and followed by BI, BS and assembly tolerance.

The influence of the *wind speed* on the EmeIs, without BI, can be studied from Figure 5.22. Above 14 m/s mean wind speed, the mean values and spread of the relative difference of the 1-Hz-DEL to the baseline model reduces significantly. This corresponds to the behaviour of the controller. Above rated, generator torque and rotational speed are nearly constant and mainly the pitch angle changes. Therefore, the results support the assumption that mainly torque and speed changes excite or amplify the EmeIs. The highest impact is found at the tower top, with an increase of up to 200 % in 1-Hz-DEL (cf. Figure 5.22 (b)). This is followed by the flapwise blade root loads (Figure 5.22(d)) and the tower base (Figure 5.22(a)). The edgewise blade root difference has a maximum of 10 % (Figure 5.22(c)).

The mean values of all blade loads are well below 10 %. The fact that the blades are affected

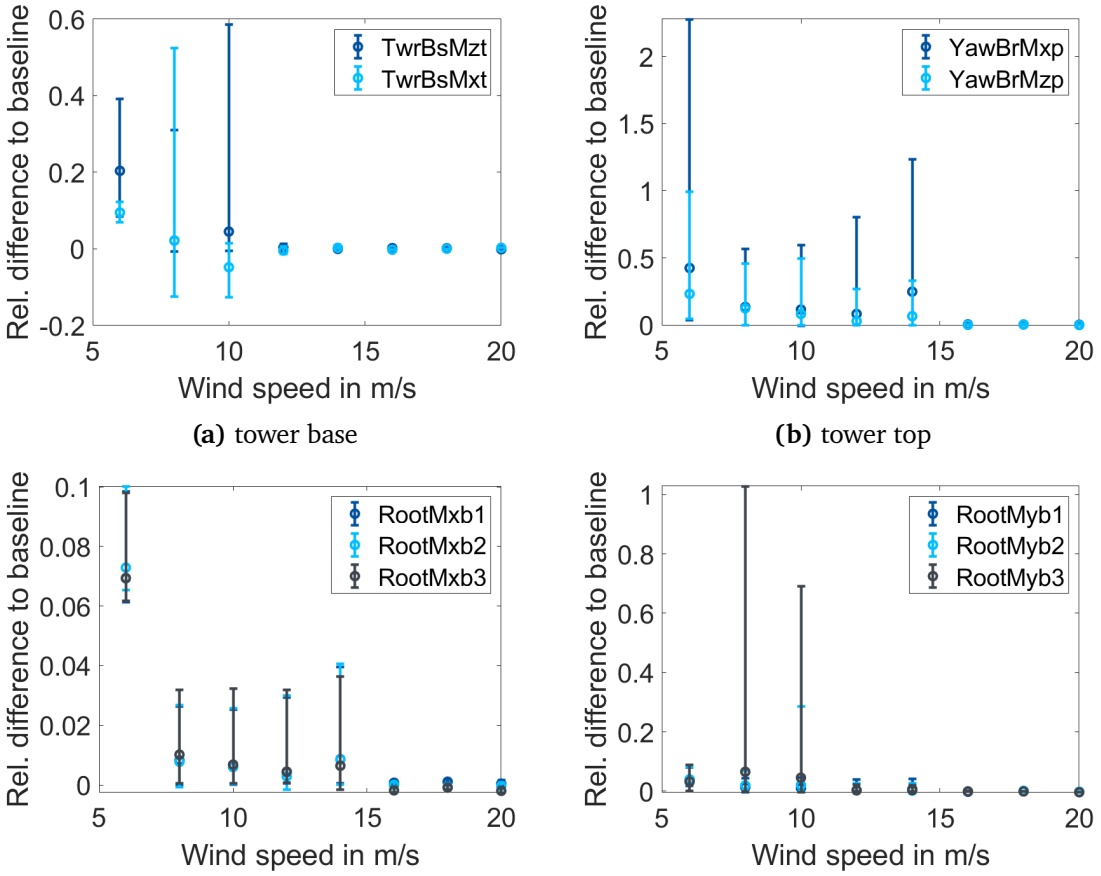

(a) tower base

(b) tower top

(c) blade root edgewise

(d) blade root flapwise

Figure 5.22.: Comparison of relative differences in 1-Hz-DEL between coupled model and baseline model over the wind speeds, for all parameter combinations with BI = 1.

only little, could mean that the whole assembly of WT rotor and generator rotor moves as a unit due to the changed support of the shaft, minimising additional loading to the blades. This agrees with the results from Section 5.4 showing interactions only for the MT mode and with limited intensity. The MT mode leads to a displacement of the blades relative to the inflow, which corresponds to a flapwise displacement. In cases, when this mode's excitation is increased for coupled simulations, this can explain the higher impact to the flapwise blade root loads than to the edgewise blade root loads.

In contrast, the loading at the tower top is highly affected by the additional DoF, as the mass of the rotor assembly is moving relative to the tower top, creating additional moments. Though the displacements are small (less than 1 mm), the large mass of the assembly (ca. 430 t) leads to significant load oscillations. The decreasing impact towards the tower bottom suggests that the structural deformation of the tower carries most of the load that is

propagated from the tower top. Furthermore, the torsional loads spread more and have slightly higher mean values, indicating a higher sensitivity to the interactions.

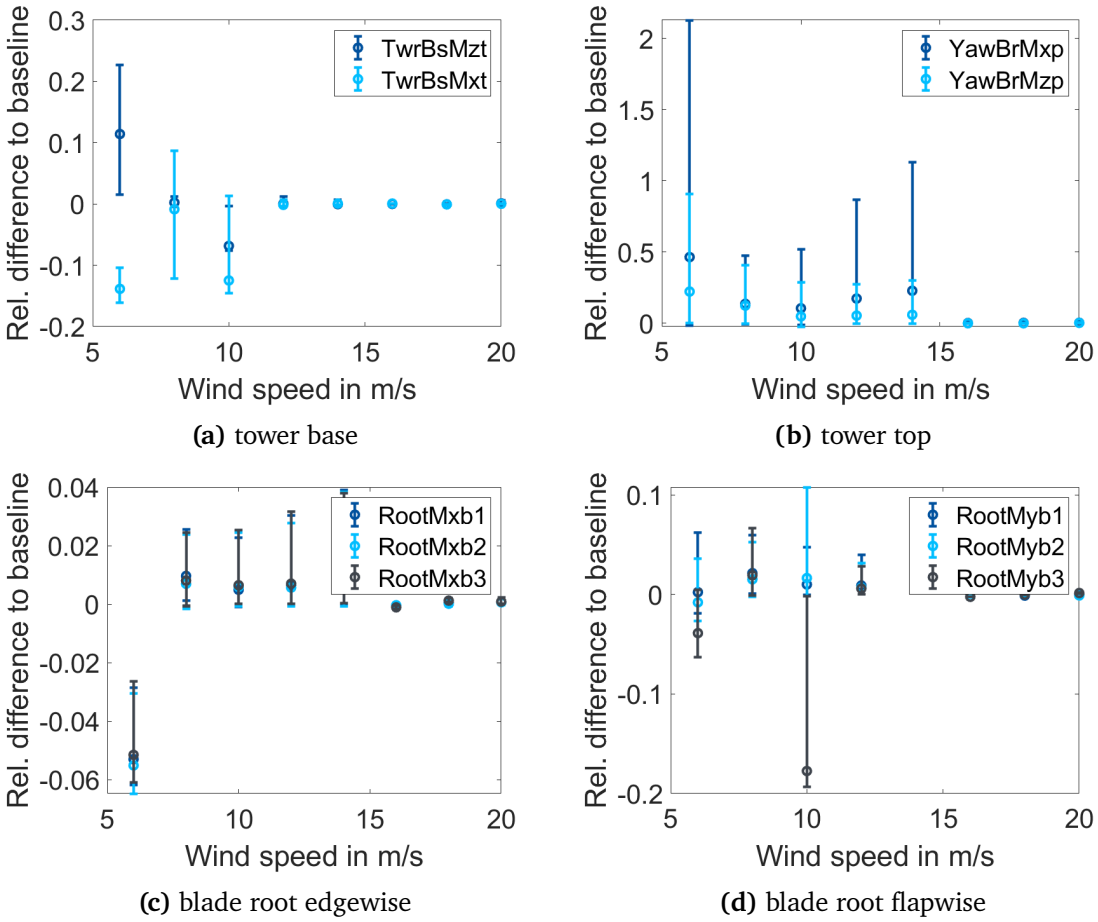

(a) tower base

(b) tower top

(c) blade root edgewise

(d) blade root flapwise

Figure 5.23.: Comparison of relative differences in 1-Hz-DEL between coupled model and baseline model over the wind speeds, for all parameter combinations with BI = 1.1.

The influence of *BI* to the interactions can be obtained from the comparison of Figure 5.22 to Figure 5.23, which summarises all simulations that include BI. For the tower base loads in Figure 5.23 (a), the maximum values of the relative difference decrease to about a third of those without BI in Figure 5.22. A similar effect can be seen for the blade root (Figure 5.23 (c)and (d)). The tower top loads (Figure 5.23 (b)) seem unaffected by BI, as the two plots look very much alike.

As the relative differences for 1-Hz-DEL, including BI, either decrease or are not affected, the BI is assumed to not contribute to EmeIs. BI adds to the SS loads in both models, baseline and electro-mechanical model. The results lead to the assumption that the changes due to BI are higher than those due to EmeIs, which would explain the reduced differences

between the two fidelities for tower base and blade root loads. The tower top loads are dominated by the oscillation of the rotor assembly mass and therefore, the differences in 1-Hz-DEL are unaffected.

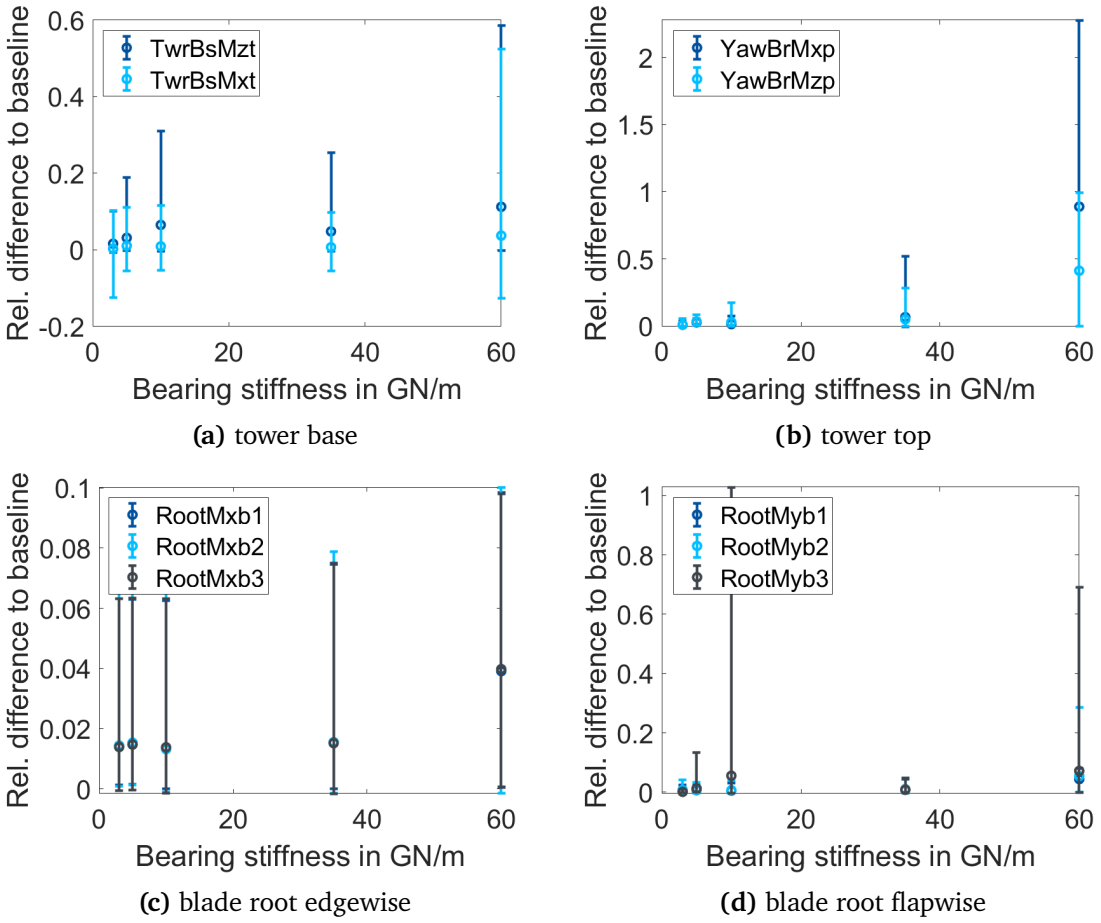

(a) tower base

(b) tower top

(c) blade root edgewise

(d) blade root flapwise

Figure 5.24.: Comparison of relative differences in 1-Hz-DEL between coupled model and baseline model over the BSs, for all parameter combinations with BI = 1 and wind speeds of 6 to 14 m/s.

The third parameter to analyse is the *BS*. It was shown with Figure 5.22 that wind speeds above 14 m/s are of minor relevance. That is why only simulations with wind speeds up to 14 m/s are considered for the BS analysis. BI is not considered in the simulations. The results are summarised in Figure 5.24. For the tower top loads (Figure 5.24(b)) a dependency of the BS can be observed. The relative difference increases with increasing BS. For the tower base loads (Figure 5.24 (a)) the spread of differences increases, also including load reductions. The mean values are less affected. Furthermore, the range of the relative difference at the tower top is more than twice that at the tower base. For the blade root, the flapwise moment (Figure 5.24 (d)) shows higher differences than the edgewise

moment (Figure 5.24 (c)). For the edgewise moment, the mean differences increase with the BS. For the flapwise moment, no clear trend can be established. The BSs of 10 GN/m and 60 GN/m show the highest spread for the used seed. Nevertheless, the highest mean value in all sensors occurs for the highest BS. Based on the results, the increasing differences with increasing BS can not be explained. A more detailed analysis based on time series comparison is performed after the parameter study, to obtain more insights.

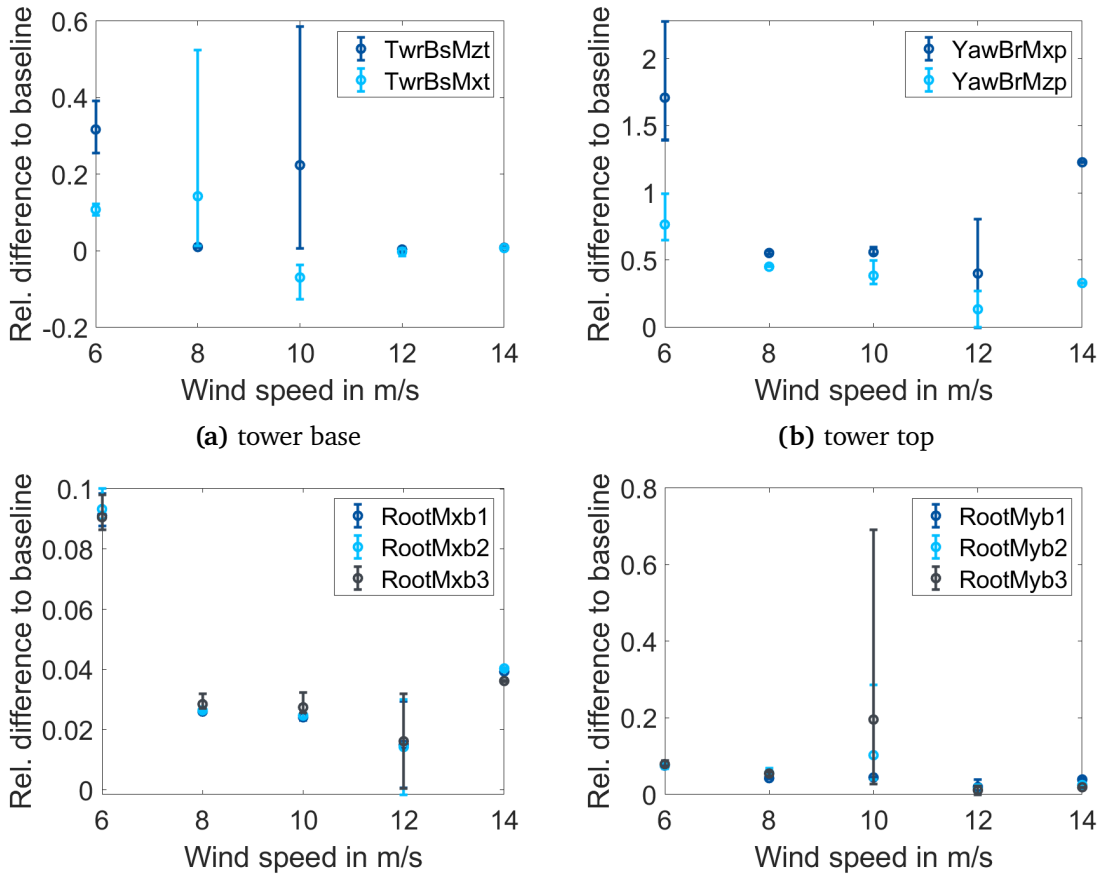

(a) tower base

(b) tower top

(c) blade root edgewise

(d) blade root flapwise

Figure 5.25.: Comparison of relative differences in 1-Hz-DEL between coupled model and baseline model over the wind speeds, for the parameter combinations with a BS = 60 GN/m and BI = 1.

The last parameter in the study is the constant eccentricity due to *assembly tolerances*. Section 5.2.1 showed that this parameter only has an influence on the maximum occurring eccentricity in cases where other effects have caused an initial eccentricity. In this part of the study, only simulations with a BS of 60 GN/m are considered. The spread and mean values of the relative differences are plotted over the wind speeds from 6 m/s to 14 m/s in Figure 5.25. Visible differences at the tower bottom occur for wind speeds of 6 m/s to

10 m/s. Here, the spread generally decreases, as this plot considers a subset of the reference plot in Figure 5.22. All wind speeds show a shift of the mean value to higher differences. For the highest two wind speeds, the spread at the tower base is so small that the subset has the same spread as the full set of simulations. This tendency of upwards shifted mean values and reduced spreads repeats for all sensors. Especially the tower top and the blade root edgewise bending moments reduce to a mean value close to the maximum value of the reference plot with minimal spread. It can be concluded that the constant eccentricity due to assembly tolerance has the highest impact at the tower bottom at 8 m/s and 10 m/s mean wind speeds, as these show the highest spread. For the tower top and the blade root edgewise bending moments, the wind speeds of 6 and 12 m/s show the highest impact. For the blade root flapwise bending moment, only the wind speed of 10 m/s looks influential. Nevertheless, the influence of the assembly tolerance to the component loading seems to be of minor importance compared to wind speed or BS. The assembly tolerance mainly introduces a constant offset to the electromagnetic forces. Therefore, no dynamic influences are expected. The results together with the fact that the electromagnetic forces are several magnitudes smaller than the forces from aerodynamics and structural dynamics, acting at the main bearing, lead to the assumption that small assembly tolerances do not have a significant impact on the loading outside the drive-train.

It can be concluded that low wind speeds and high BSs show the largest differences in 1-Hz-DEL to the baseline model. BI causes higher loads in general, which are more significant than the loads due to EmeIs and therefore, reduce the differences between the models. The assembly tolerance only adds up to eccentricities caused by other impacts and can be neglected as a reason for EmeIs.

So far, the study is based on one seed per wind speed. To test the dependencies obtained as relevant, two more wind seeds are simulated for each wind speed between 6 and 14 m/s. The statistical evidence with three seeds per wind speed is limited, as usually five to six seeds are considered necessary. Nevertheless, it is assumed to be a good trade-off between the needed computational effort and the identification of first indications for EmeIs. BI and constant eccentricity are excluded to reduce the computational effort and focus on the most relevant parameter space, leading to 100 simulations for the two additional seeds.

Figure 5.26 shows the statistical summary of all three wind seeds over the BSs. The strongest interactions for high bearing stiffnesses can be observed for the tower top loads.

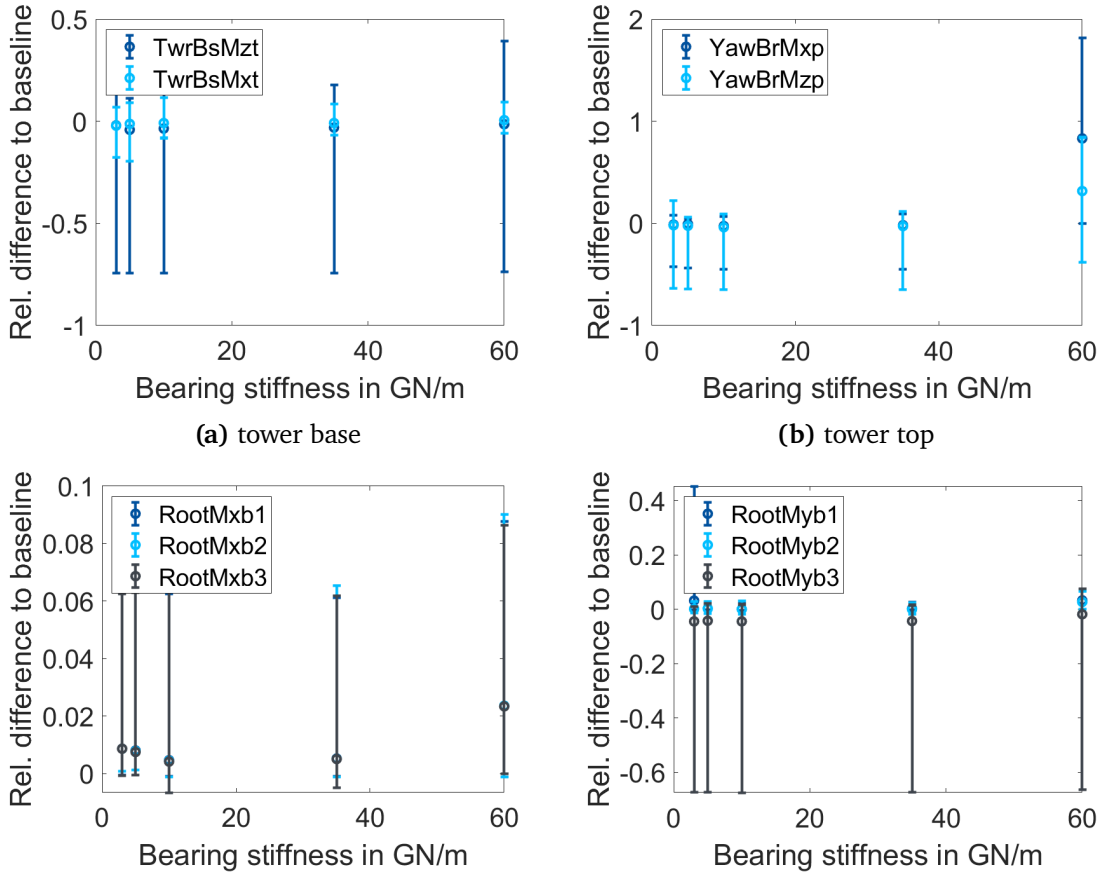

(a) tower base

(b) tower top

(c) blade root edgewise

(d) blade root flapwise

Figure 5.26.: Comparison of relative differences in 1-Hz-DEL between coupled model and baseline model over the BS with two additional wind seeds for wind speeds of 6 to 14 m/s, excluding assembly tolerance and BI.

The tower base loads show an increase in spread for the torsional moment, but mean values remain approximately constant. The blade root edgewise moment for three seeds remains statistically similar to one seed. The blade root flapwise moment reduces in its spread for all BSs except the lowest stiffness, where the spread increases. The reduction of spread can be explained with the exclusion of the cases with BI or assembly eccentricity for this comparison between seeds. The identified dependencies of loads to the parameters of BS for mean wind speeds up to 14 m/s is confirmed by the two added seeds.

One-to-one comparison: Based on the statistical analysis, the number of simulations of relevance has been narrowed down to those with wind speeds up to 14 m/s and BSs of 3 GN/m or 60 GN/m. These simulations are compared on a one-to-one level of time series and frequency spectra, with the aim to identify explanations for the interactions.

First, the frequency spectra of different wind speeds for a constant BS of 60 GN/m are

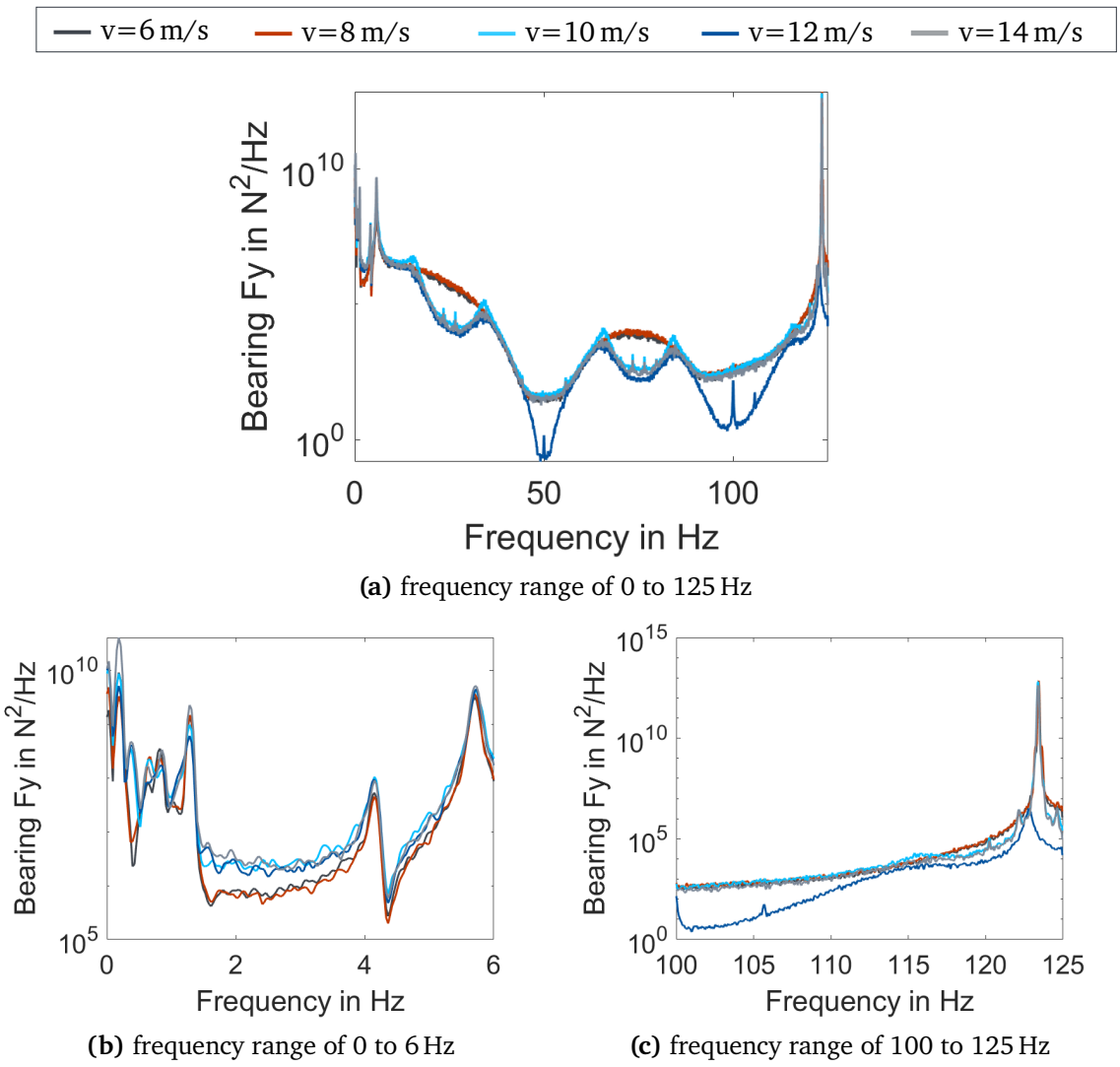

(a) frequency range of 0 to 125 Hz

(b) frequency range of 0 to 6 Hz

(c) frequency range of 100 to 125 Hz

Figure 5.27.: Comparison of frequency spectra of the bearing force in y-direction for different wind speeds a BS of 60 GN/m and ideal assembly, excluding BI (a) for the full frequency spectrum up to 125 Hz, (b) a close-up to the frequency range up to 6 Hz and (c) a close-up to the frequency range of 100 Hz to 125 Hz

compared. Figure 5.27 (a) shows the frequency range up to 125 Hz of the spectrum of the bearing force in y-direction for all wind speeds. All spectra have a similar shape. The drops at 50 Hz and 100 Hz, due to the chosen communication interval with the aerodynamic solver, are visible in the results for all wind speeds with varying depth. To better understand the details of differences, a close-up of the spectra is shown for the range up to 6 Hz in Figure 5.27 (b) and the range of 100 Hz to 125 Hz in Figure 5.27 (c). Differences mainly occur for the frequencies above 100 Hz. 12 m/s mean wind speed shows a peak of lower prominence for the bearing mode around 123 Hz. The first SS mode (0.19 Hz) and the second SS mode (1.28 Hz) have the highest amplitude for 14 m/s mean wind speed, though

Table 5.3.: Comparison of relative difference of 1-Hz-DEL for tower base, tower top and blade root between different wind speeds for a BS of 60 GN/m normalised to the 1-Hz-DEL of the baseline model.

wind speed	6 m/s	8 m/s	10 m/s	12 m/s	14 m/s
tower base Mx	0.00	0.02	0.01	0.00	0.00
tower base Mz	0.09	0.11	0.09	0.00	0.05
tower top Mx	1.37	1.50	1.01	0.00	1.14
tower top Mz	0.63	0.72	0.51	0.00	0.28
blade 1 root Mx	0.04	0.05	0.04	0.00	0.04
blade 2 root Mx	0.04	0.05	0.04	0.00	0.04
blade 3 root Mx	0.04	0.05	0.04	0.00	0.04
blade 1 root My	0.10	0.13	0.05	0.00	0.03
blade 2 root My	0.10	0.13	0.05	0.00	0.03
blade 3 root My	0.09	0.13	0.05	0.00	0.03

generally the differences between the spectra of the different mean wind speeds are minor.

The relative differences of 1-Hz-DEL for the investigated sensors are listed in Table 5.3. The comparison confirms that the highest differences occur for the tower top loads. The tower base loads are less affected. The rotor blades show a larger difference for the flapwise moment at 6 m/s and 8 m/s mean wind speed. No differences occur for 12 m/s mean wind speed, which showed the lower amplitude of the bearing mode peak in its spectrum (cf. Figure 5.27). This result supports the assumption of system coupling effects. The stronger the excitation of oscillations in the bearing, the higher the tower top 1-Hz-DEL. The reason for the reduced excitation of bearing oscillation for 12 m/s mean wind speed could not be determined. However, the standard deviation of the rotational speed was found to be significantly reduced compared to the other mean wind speeds. This could mean an interaction with the controller, reducing the bearing mode oscillation of the 12 m/s mean wind speed simulation and amplifying them for the other mean wind speeds.

In the next step, the frequency spectra for 8 m/s mean wind speed between the three simulated seeds are compared with a BS of 3 GN/m. Figure 5.28 (a) shows the overview over the frequency spectra up to 50 Hz. All three seeds show similar spectral shape. The low-frequency part, up to 6 Hz in Figure 5.28 (b), is only slightly affected by the variations of the seeds. For the higher frequency part from 20 Hz to 30 Hz in Figure 5.28 (c), the differences are also of minor prominence. Nevertheless, seed 1 shows the lowest spectral peak in the natural bearing frequency, which indicates a reduced excitation of the bearing

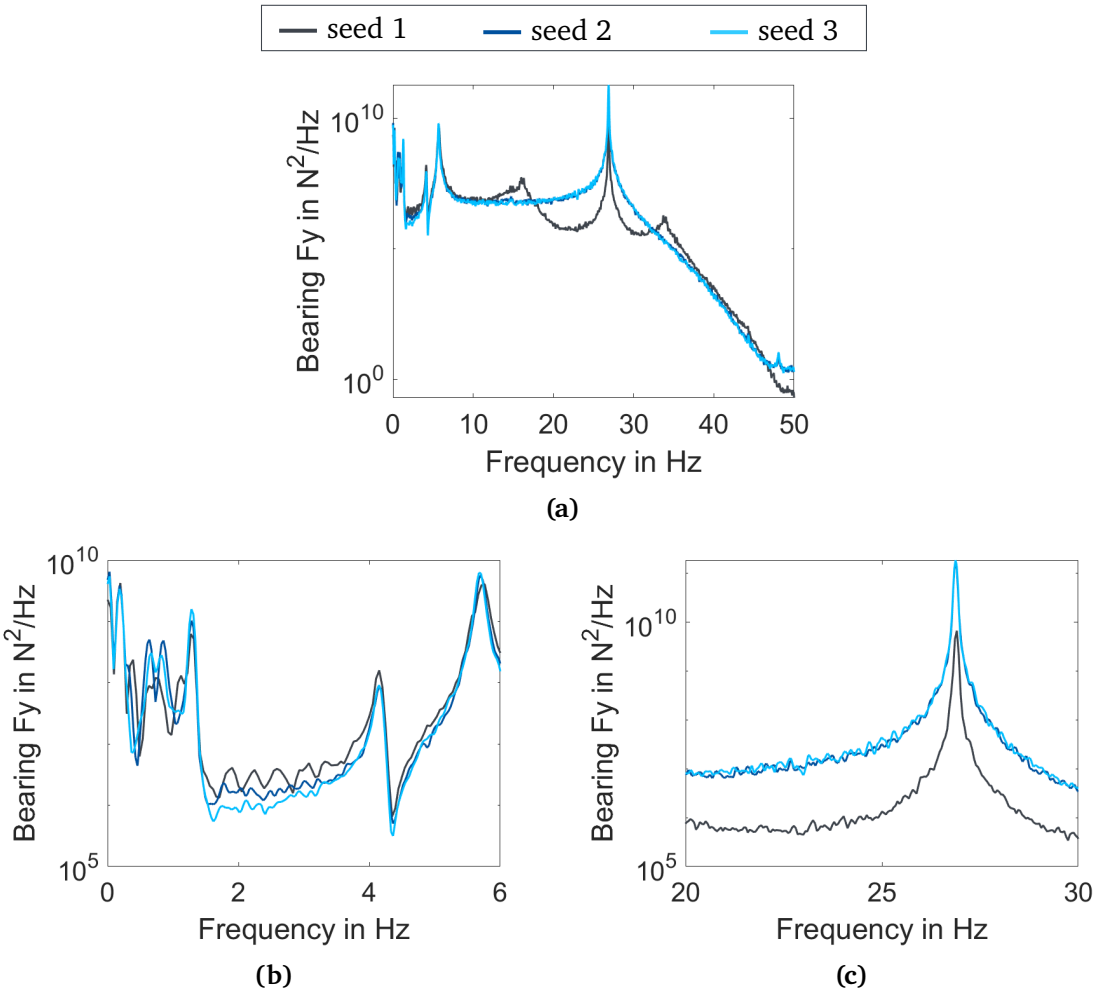

Figure 5.28.: Comparison of frequency spectra of the bearing force in y-direction for three seeds with 8 m/s mean wind speed with a BS of 3 GN/m and ideal assembly, excluding BI (a) for the full frequency spectrum up to 50 Hz, (b) a close-up to the frequency range up to 6 Hz and (c) a close-up to the frequency range of 20 Hz to 30 Hz

mode by this wind field. The 1-Hz-DEL for the investigated sensors are listed in Table 5.4.

In this case, the tower base loads are more affected than the tower top loads and the blade loads show only minor impacts of the seed variations. Seed 3 generally shows the highest relative differences in 1-Hz-DEL. The 1-Hz-DEL of the tower base bending moment in side-to-side direction are negative for all seeds. This implies that the SS oscillations are reduced for low BS, compared to the baseline model. One possible explanation can be that the added DoF with the high inertia of the rotor assembly mass and a larger oscillation amplitude, due to a lower BS, damps the tower top displacement. Furthermore, the first two seeds generally only show negative differences, while the third seed leads to positive differences. This indicates a dependency of the wind field variations on the WT loading.

Table 5.4.: Comparison of relative differences of 1-Hz-DEL for tower base, tower top and blade root between different wind seeds at a mean wind speed of 8 m/s for a BS of 3 GN/m.

wind seed	1	2	3
tower base Mx	-0.13	-0.20	-0.02
tower base Mz	0.00	-0.71	0.29
tower top Mx	0.00	-0.42	0.08
tower top Mz	0.00	-0.64	0.22
blade 1 root Mx	0.00	0.01	0.02
blade 2 root Mx	0.00	0.01	0.01
blade 3 root Mx	0.00	0.01	0.02
blade 1 root My	0.00	-0.01	0.15
blade 2 root My	0.00	-0.04	0.01
blade 3 root My	0.00	-0.54	0.01

The comparison of wind speeds has shown that the combination of 60 GN/m BS and 8 m/s mean wind speed produces the largest differences in 1-Hz-DEL. Though smaller than for a BS of 60 GN/m, the comparison of the three seeds with 8 m/s mean wind speed and a BS of 3 GN/m shows the largest deviation for seed three. This is assumed to be a wind field specific result, which is investigated further.

The time series of this seed for different BSs are compared. Figure 5.29 (a) to (f) show the comparison of the time series of the six load sensors for 20 s with the mean wind speed of 8 m/s, with a BS of 3 and 60 GN/m to the baseline results. For the higher BS, the tower top and blade root loads show a high frequency oscillation, which decreases at the tower base. The low BS leads to results closer to the baseline solution. Only the tower base moment in side-to-side direction differs clearly from the baseline solution for both BSs. The differences of tower top and base loads are due to the deformation energy stored in the tower.

Figure 5.30 compares the tower top displacement (a) in SS direction and (b) for MT. The displacements in SS direction are clearly affected by the BS. The RMSD, relative to the baseline, is 0.13 for the low BS and 0.11 for the high BS. Using the high BS as reference time series, the RMSD between the two BSs equals 0.1. Differences in torsion are less prominent in the time series. The RMSD, relative to the baseline, for the low BS is 0.17 and for the high BS is 0.01. Normalised to the high BS, the RMSD of the low BS also results in 0.17. This means, for torsion only the low BS differs from the solution of the baseline model, whereas for the SS movement both BSs differ equally from each other as they differ from

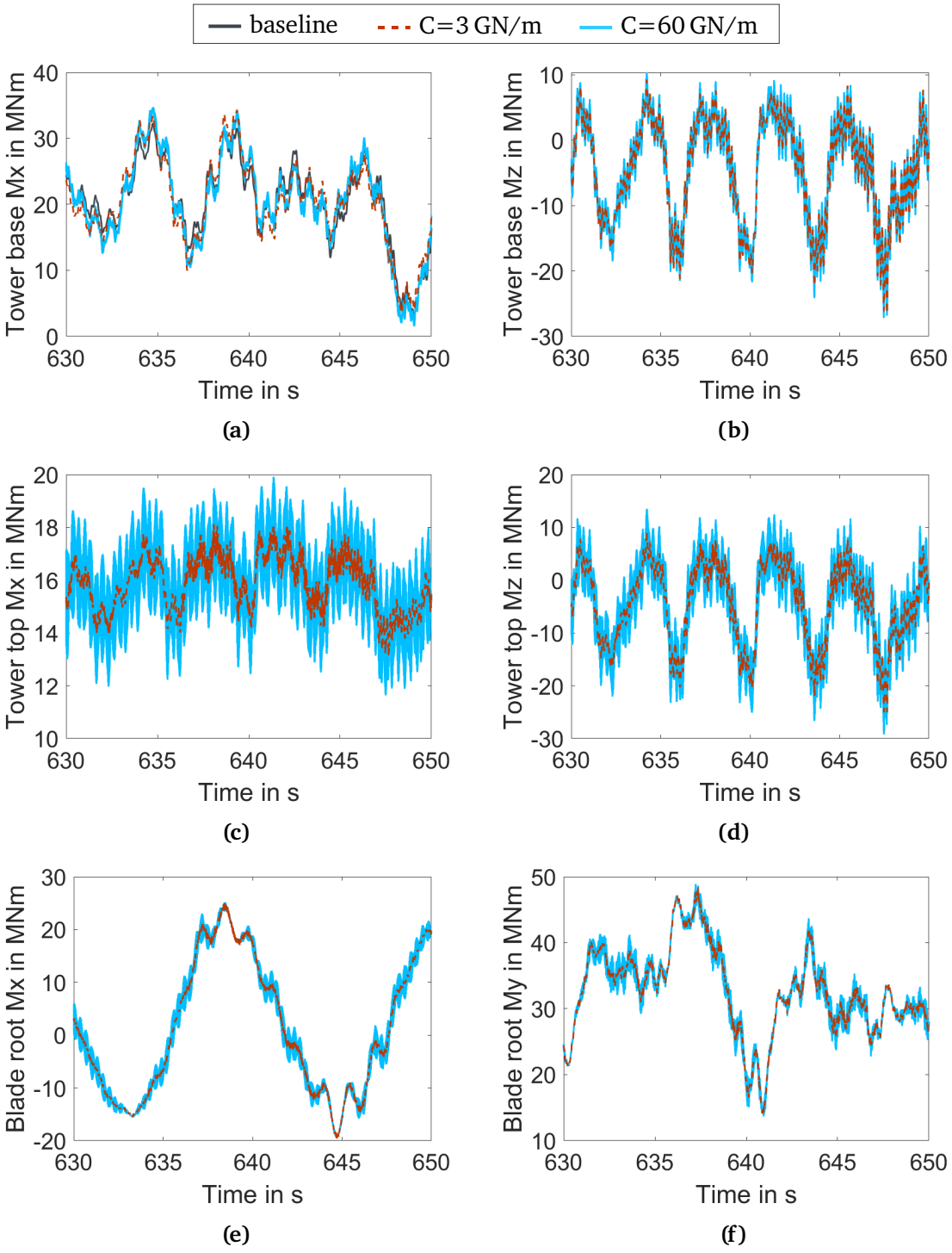

Figure 5.29.: Comparison of load time series for 8 m/s mean wind speed for seed 3 between the baseline model (dark grey), and the electro-mechanical model with a BS of 3 GN/m (red dashed) and 60 GN/m (light blue) (a) and (b) at the tower base, (c) and (d) at the tower top and (e) and (f) at the blade root.

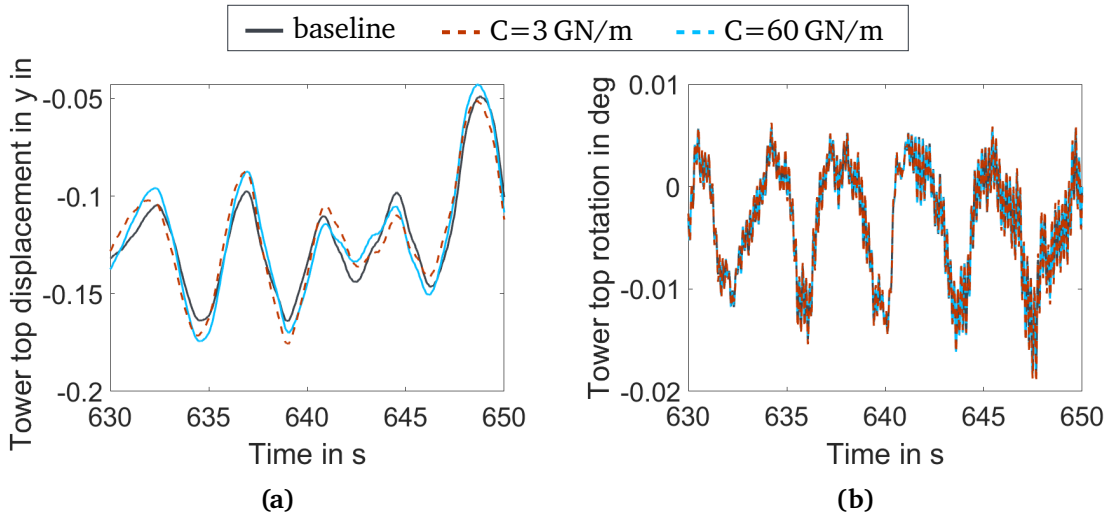

Figure 5.30.: Comparison of the tower top displacement time series for 8 m/s mean wind speed for seed 3 between the baseline model (dark grey), and the electro-mechanical model with a BS of 3 GN/m (red dashed) and 60 GN/m (light blue) (a) in global y-direction and (b) around the tower z-axis.

the baseline solution.

The BS influences the amplitude of the bearing mode oscillation, leading to larger amplitudes for lower BS. The maximum amplitude for a BS of 3 GN/m is ten times higher than for a BS of 60 GN/m for these simulations (cf. Figure 5.8). In addition, the natural frequency of the oscillation is lower for lower BS. This can cause the BS-dependent SS displacement, as a larger displacement of the generator leads to a larger tower top moment in SS direction. In consequence, the three simulations all behave different.

The torsional tower top displacement is not affected by the amplitude of the bearing mode oscillation. This displacement is affected by the main bearing forces in y-direction, which have an arm to the tower vertical axis. These forces differ only with a factor of two, with the higher force occurring for a BS of 60 GN/m. In consequence, the differences between the two BS for MT are reduced compared to the differences in SS direction.

To explain the differences to the baseline model, the impact of the added DoF and the BS to the coupled system modes has to be considered. The differences in SS 1-Hz-DEL can be explained by the differences of the tower top displacement due to the BSs. The differences in MT 1-Hz-DEL can be explained by the deformation energy distribution. The energy stored by the bearing spring equals $E_{\mathrm{spr}} = \frac{1}{2}cs^2$. Comparing the two BSs, the stiffness differs with a factor of 20, whereas the maximum eccentricity differs with a factor of 100. This means

the maximum energy stored in the bearing with the high BS is only 20 % of the maximum energy, stored in the soft bearing. Therefore, in case of the high BS, the energy contributes more to the tower displacement. The baseline solution equals an ideally stiff bearing, where all deformation energy is stored in the tower. That is why, the high BS solution is closer to the baseline solution than the low BS, when comparing tower top displacements.

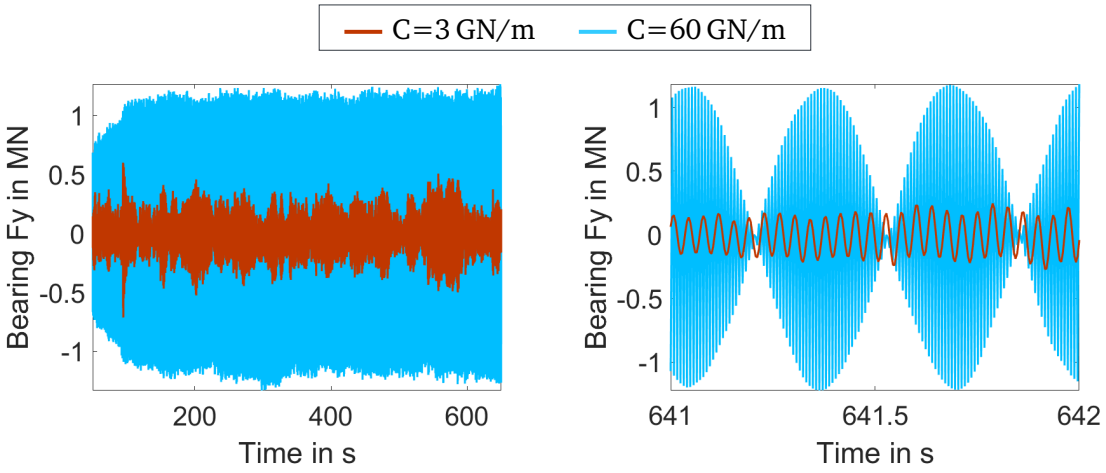

(a) complete time series from 50 s to 650 s

(b) Zoom of time series to 1 s

Figure 5.31.: Comparison of bearing force time series in local non-rotating y-direction with 8 m/s mean wind speed and seed 3 for the electro-mechanical models with 3 GN/m (red) and 60 GN/m (light blue), showing in (a) the complete 600 s and in (b) a zoom to 1 s of simulation.

Analysing the time series of the bearing forces in y-direction in Figure 5.31, shows the increased amplitude of the force for the BS of 60 GN/m. Looking at one second of the simulation time in Figure 5.31 (b), a significant difference between the two BSs can be observed. The frequency of the high BS is modulated by some other frequencies, leading to a cancelling out of the oscillations at certain times, which does not occur for the BS of 3 GN/m. One modulating frequency is determined to 3 Hz from the figure, which is not a known system frequency. Accordingly, the spectra for both cases (red curve in Figure 5.27 and light blue curve in Figure 5.28) do not show a peak at 3 Hz, leading to the assumption that the modulation is caused by a combination of other frequencies than the 3 Hz. Possible frequencies, which can be identified from the spectra, are the tower frequencies of the SS and MT modes. Nevertheless, a clear identification based on the given results is not possible.

The results indicate an interaction with the torque controller and Figure 5.21 shows that for wind speeds below 14 m/s, the controller behaviour is slightly affected by the changed

WT dynamics. In the next step, the interactions are investigated based on time series comparison. Similar to the investigations on aerodynamic interactions, one way to quantify the controller interactions is to switch off the controller. This means, the rotational speed and pitch angle are constant. This type of simulation is called open-loop system analysis, whereas the simulation including the controller feedback is called closed loop. For the wind fields with extreme turbulence, this can not be done, as the WT would run into operating conditions far from the design points. When the discrepancy from the designed operating points is too high, instabilities can occur.

Therefore, the open-loop analysis is performed with adapted wind fields with only 1 % of turbulence intensity. To account for statistical variations, three seeds are used, and the analysis is conducted for 6 m/s, 8 m/s and 14 m/s mean wind speed for the low (C=3 GN/m) and high (C=60 GN/m) BS. The simulation results of baseline model and electro-mechanical model are compared. The comparison is performed for the open loop and closed loop setup. As the number of 18 simulations for this analysis is limited, a lower communication interval to the aerodynamic solver of 0.0008 s can be used (cf. Section 5.4), to reduce modelling uncertainty.

Table 5.5.: Comparison of mean relative difference of 1-Hz-DEL ΔDEL_{rel} for the tower base bending moment in SS direction between new and baseline model over three seeds with a turbulence intensity of 1 % for different mean wind speeds v and different BSs C.

v in m/s	C in GN/m	ΔDEL_{rel} in %
6	3	0.14
6	60	3.05
8	3	-2.17
8	60	0.59
14	3	0.47
14	60	0.13

The mean difference of 1-Hz-DEL among the three seeds has been calculated. The results are listed in Table 5.5. The results show a trend of decreasing differences in 1-Hz-DEL with increasing wind speed for the high BS. For the wind speeds below rated, the higher BS leads to higher differences in 1-Hz-DEL. These results agree with the results of the extreme turbulence analyses but are significantly reduced in absolute values of the differences.

In the next step, the dynamic behaviour of the WT is evaluated in more details. Figure 5.32 compares the tower top displacements of the baseline model and the electro-mechanical

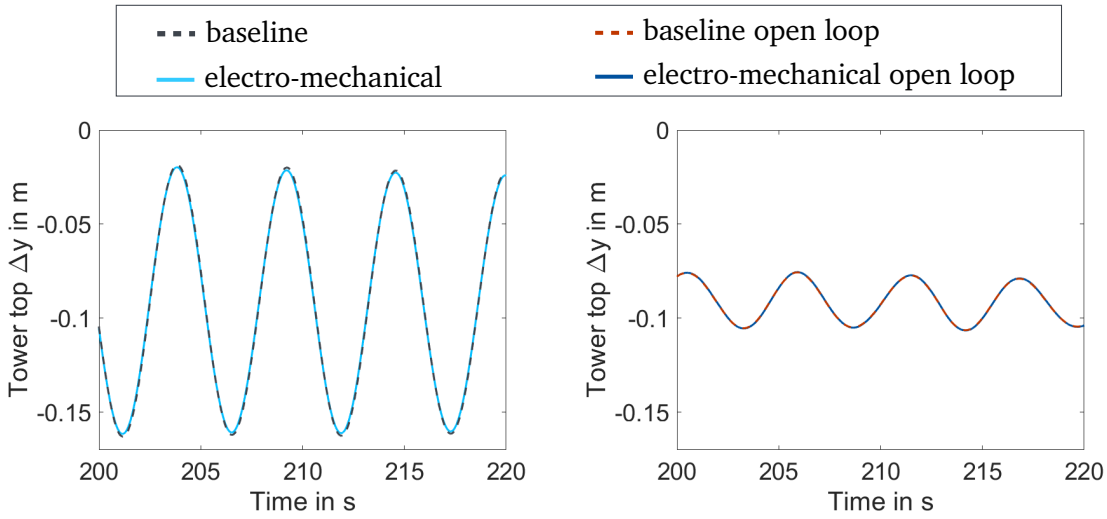

(a) closed loop **(b)** open loop

Figure 5.32.: Comparison of tower top displacement in global y-direction with 8 m/s mean wind speed and a turbulence intensity of 1 % (a) in closed loop simulation and (b) in open loop simulation with constant rotational speed of 5.7 rpm and a BS of 60 GN/m

model in (a) for closed loop analysis and in (b) for open loop analysis. A mechanical instability can be excluded from the open loop results, as the oscillation amplitudes do not increase over time. The amplitude of the closed loop simulations is about five times higher than for the open loop simulations, increasing from about 3 cm to about 15 cm. The oscillation equals the first SS natural frequency. All in all, the comparison of open and closed loop results of the baseline model shows similar differences as the comparison of open and closed loop results of the electro-mechanical model. The controller amplifies the tower top displacement oscillation with the first SS natural frequency.

Figure 5.33 shows the time series of the tower top SS bending moment. The SS moment is overlaid with a high frequency oscillation, when including the additional DoF. This effect occurs for open loop and closed loop conditions. The fact that the oscillations occur in open loop simulations, too, suggests that it is caused by mechanical interactions. However, the controller is amplifying this overlaid oscillation heavily. Equivalent to the results from Figure 5.31, the high-frequency oscillation is modulated by other frequencies, which are likely to be the tower natural frequencies for SS and MT mode. The increased oscillation amplitude of the tower top SS displacement could cause the bearing mode amplification.

An additional comparison to the closed loop result for the BS of 3 GN/m, which is not plotted here, shows that the low BS leads to a tower top bending moment equal to the

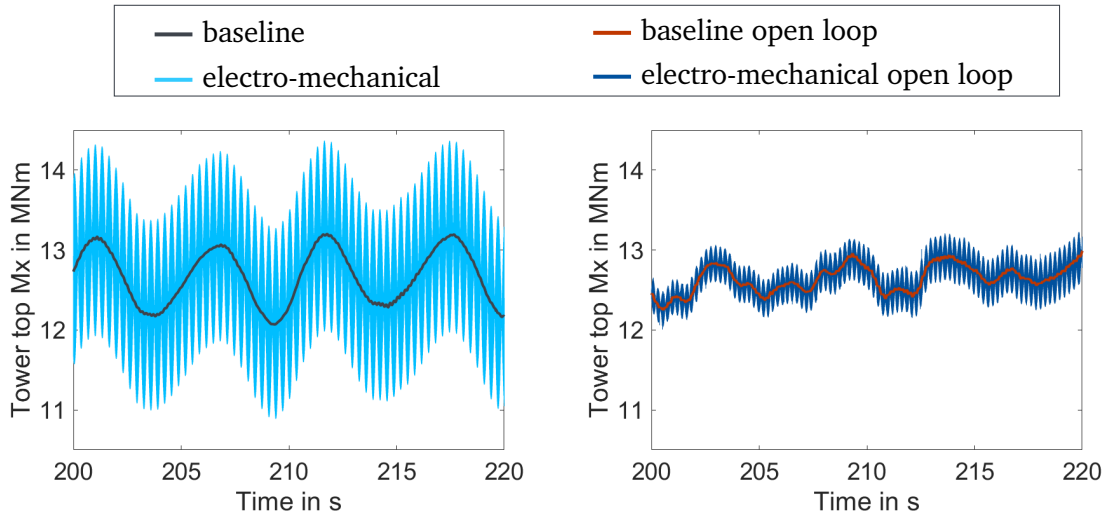

(a) closed loop **(b)** open loop

Figure 5.33.: Comparison of the moment around tower top x-axis pointing downwind, with 8 m/s mean wind speed and a turbulence intensity of 1 % (a) in closed loop simulation and (b) in open loop simulation with constant rotational speed of 5.7 rpm and a BS of 60 GN/m

baseline solution. The choice of the small communication time step excludes it as cause for the amplification of the oscillation. In consequence, the EmeIs depend on the oscillation amplitude and natural frequency of the bearing mode, and increasing wind speeds reduce their impact. It can not be distinguished, whether high wind speeds show reduced EmeIs due to the control region or due to the changed aerodynamic loads.

In summary, the statistical analysis of the full parameter space has shown that the highest differences in 1-Hz-DEL occur for low wind speeds up to 14 m/s and for the extremes of the investigated BSs (C=3 and 60 GN/m). For the high BS, mainly the tower top loading is affected. For the lower BS, the tower base loading is affected more. The blades generally only show slight impacts by EmeIs. No clear correlations for the parameters of BI or assembly tolerance have been identified. However, the results showed that the spread of 1-Hz-DEL differences decreases when these parameters are kept to their ideal values (no BI and perfect generator alignment). The results show that the larger amplitude of the bearing mode oscillation for low BS can increase and decrease loads at the tower base whereas the high BS leads to an interaction with the torque controller, which amplifies the bearing mode oscillation and increases the tower top loads. With a BS of 60 GN/m, oscillations with the bearing frequency are modulated by other frequencies, which could not be identified but are expected to be the tower natural frequencies of the coupled SS and MT mode. The fact

that load reductions can occur, using a low BS, whereas the high BS leads to load increases, shows that the common assumption that the bearings have to be as stiff as possible, to avoid EmeIs, can not be supported by the system design approach.

5.6.2. Fidelity influence

The interactions of the adapted model with the WT structure, the aerodynamics, and the controller have been discussed in the previous sections. So far it has not been differentiated between the influence of the added DoF and the influence of the electromagnetic forces. This differentiation will be discussed in this section.

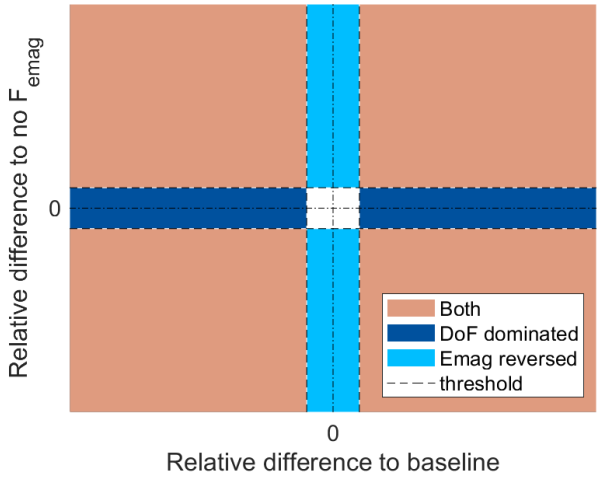

Figure 5.34.: Qualitative result plot, to distinguish between influences from the added DoF and the electromagnetic forces, to support the interpretation in the following

The comparison of the relative differences of 1-Hz-DEL of the model, including electromagnetic forces, to the baseline model and to the model, excluding electromagnetic forces, are shown in scatter plots. To facilitate the interpretation of the result plots, a qualitative plot is given in Figure 5.34. On the x-axis the difference of the electro-mechanical model to the baseline is plotted, and on the y-axis the relative difference of the electro-mechanical model to the model excluding electromagnetic forces but including the new DoF is plotted. Large differences on the x-axis in combination with small differences on the y-axis indicate that the differences mainly result out of the added DoF (dark blue shaded areas). A large difference on the y-axis and a small difference on the x-axis indicate that the electromagnetic forces cancel out the influence of the added DoF (light blue shaded areas). When the differences on both axis are large, it indicates that both, the additional DoF and the electromagnetic forces

contribute to the changed WT loads (red shaded areas). A positive difference generally means an increase in loads with fidelity and a negative difference means a load reduction with fidelity increase, respectively. A minimum absolute difference of 10 % in 1-Hz-DEL is used as threshold, to assume the relative difference as significant for design loads. To quantify the impact to design life accurately, however, a lifetime analysis according to the standards would be needed.

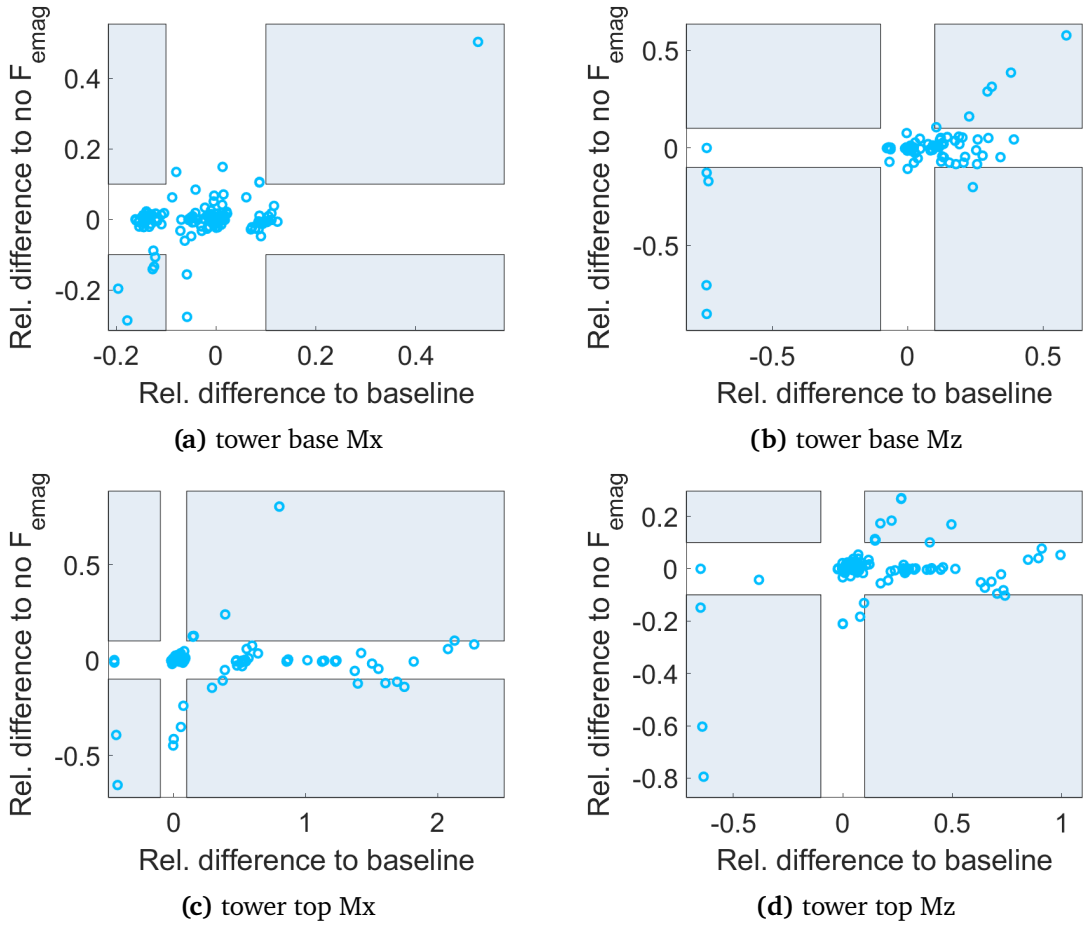

(a) tower base Mx

(b) tower base Mz

(c) tower top Mx

(d) tower top Mz

Figure 5.35.: Relative differences of 1-Hz-DEL of the electro-mechanical model to the model without electromagnetic forces, but with the added DoF over the relative differences to the baseline model for (a) and (b) at the tower base and (c) and (d) at the tower top. In (a) and (c) the SS bending moments, and in (b) and (d) the MT moments are shown. The areas where both differences cross the 10 % threshold are marked with shaded rectangles.

Figure 5.35 shows the scatter plot for the tower base loads in (a) and (b) and the tower top loads in (c) and (d). The areas, where the threshold is exceeded on both axes, are marked with blue shaded rectangles.

For all sensors, numerous points can be found close to the zero difference for both axes. For

those points, which exceed the threshold, the difference to the baseline model is dominant in most cases, indicating, that the added DoF is the main driver for the EmeIs. In consequence, it would be sufficient to include the DoF in the simulation model in the future and the coupling to the electromagnetic field could be neglected. Cases with possible influences of the electromagnetic forces are mainly found for the torsional loads.

Additionally, the significant number of points for tower top loads, where the difference to the baseline model is close to zero but the difference to the model without electromagnetic forces is far below zero, is interesting. This indicates a potential vibrational interaction due to the added DoF, which is damped by the electromagnetic forces. Alternatively, the shift in natural frequency due to the negative stiffness of the electromagnetic field avoids a resonance and reduces the oscillations. For those cases, a model neglecting the electromagnetic forces would lead to a highly conservative design of components. It would be preferable to use the state-of-the-art model for those cases, if computational efficiency is important.

Figure 5.36 shows the scatter plot of relative differences for the blade root loads of all three blades, in edgewise and flapwise direction. From this plot, it can be seen that the blade root 1-Hz-DEL rarely exceeds the threshold. Only for the flapwise moment, cases occur, where the threshold is exceeded on both axes. The flapwise mode can couple to the MT mode, in case of larger amplitudes of tower torsion. The results align with the analysis of interactions with the aerodynamic forces, which showed interactions with the MT mode, and no interaction with the bearing mode.

In summary, the tower can be affected by the added DoF or the EmeIs or both. Neglecting the EmeIs or both modelling aspects can lead to an in-correct design load.

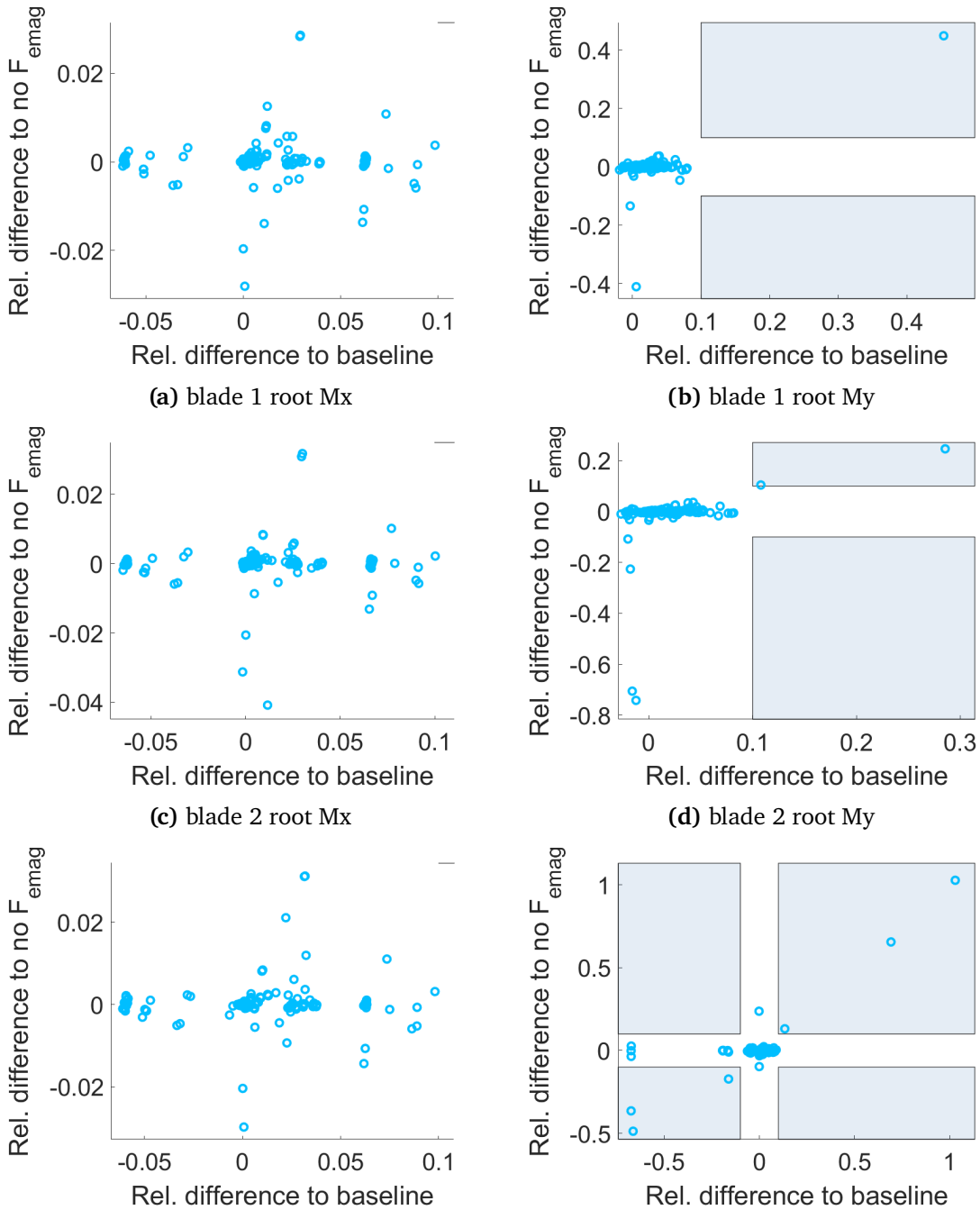

(a) blade 1 root Mx

(b) blade 1 root My

(c) blade 2 root Mx

(d) blade 2 root My

(e) blade 3 root Mx

(f) blade 3 root My

Figure 5.36.: Relative differences of 1-Hz-DEL of the electro-mechanical model to the model without electromagnetic forces, but with the added DoF over the relative differences to the baseline model for the blade root of the three blades. In (a), (c) and (e) the edgewise moments and in (b), (d) and (f) the flapwise moments are shown. The areas where both differences cross the 10 % threshold are marked with shaded rectangles.

Chapter 6

Summary, conclusion, and outlook

Wind energy research and industry aim to contribute to the transition towards 100 % renewable energy. Suitable sights for wind farms are limited, and so are the resources needed to build a Wind turbine (WT). Therefore, developments of new WTs show a trend of increasing nominal power per WT, reducing overall material consumption and increasing the power per area ratio. Wind farms are installed onshore and offshore. Onshore, the implications to residences, agriculture and environmental conservation programs limit the WT size and number. Offshore, these limitations can be avoided. At the same time, offshore sites are less accessible than onshore, requiring a high reliability of WTs to minimise maintenance efforts. One approach is using direct-drive concepts, avoiding gearboxes, as they showed a high error rate in the past.

Current developments of direct-drive WTs with nominal power of more than 10 MW, include a generator with 10 m diameter and more. Scaling laws to design generators of that size have shown that passive support structure mass is increasing over-proportionally to power. This has lead to an increased research effort for mass reduction of the generator by testing new generator concepts, applying lightweight construction methods and testing new materials and manufacturing techniques. All efforts try to optimise the generator design as isolated component with given boundary conditions. However, this work assumes that better optimisation results can be achieved based on a system design approach.

Modern design approaches are based on extensive numerical simulation campaigns to focus the prototype testing on the most promising designs. Therefore, accurate representations of

WTs are needed, based on a profound understanding of the physical phenomena involved in WT dynamics. The state-of-the-art WT models assume flexible blades, tower and foundation, modelled as Euler-Bernoulli beams and a torsional spring-damper-system for the drive-train. A system design approach for generator designs requires the investigation of Electromechanical interaction (EmeI)s. These interactions can occur through the generator torque in torsional direction. Additionally, radial eccentricity of the generator rotor relative to the stator can lead to additional forces in the system. The adaptations, needed for the torsional interactions, are easy to achieve, as analytical descriptions of generator torques are available to be added as new force into the system. Interactions due to eccentricity need a higher effort to be implemented, as they require an additional Degree of freedom (DoF) in the drive-train. Models to describe the local effects of eccentricity can be found in literature. However, the interface between the WT model and the generator model needs to be defined and is the basis of this work.

6.1. Summary

This work introduces a software coupling for the analysis of EmeIs in WTs using a high fidelity generator model in 2D Finite element method (FEM) representation in Chapter 3. This coupling defines the interface variables of the WT model to the generator model. The models of the WT and the generator are introduced in Chapter 4. The WT model is extended to include a radial DoF in the drive-train, allowing the modelling of radial eccentricity. This goes along with a model for bearing support at the locations of the main bearings. Besides a 2D FEM representation of the generator, an analytical model for electromagnetic forces in radial direction is coupled to the WT model.

Before an application of the developed models to a system design approach for WTs of high rated power, a better understanding of potential interactions is needed. This work aims to contribute to this multi-physical understanding. Therefore, three Research question (RQ)s are derived based on a literature review in Chapter 2. The analyses to answer these RQs are explained in Chapter 5. The identification of interactions shows that the aerodynamics are not affected. The interactions with the structural dynamics of the WT strongly depend on the chosen Bearing stiffness (BS). Finally, the controller shows an amplification of the interactions with the structural dynamics of the WT.

The EmeIs cause changes in the overall WT dynamics and imply changes to the WT loading at the tower and the main bearings. These implications can lead to both, an under- and an overestimation of fatigue loads using the state-of-the-art approaches.

The comparison of the varying model fidelities reveals that the representation of EmeIs in WTs using an analytical generator model enhances the load estimations for the WT design. At the same time, the computational effort is limited, as the simulation time of a 10 min simulation increases only by a factor of roughly 1.3. Higher fidelity analyses showed potential for additional interactions, which can not be captured by the analytical model. However, the computational effort makes these models currently unfeasible for load analysis. A detailed discussion of the results, the derived conclusions and the answers to the RQs are explained in Section 6.2.

6.2. Conclusions about electro-mechanical interactions in wind turbines

Based on a literature review outlined in Section 2.3, three RQs have been formulated in Section 2.4. This section discusses the results and gives concluding answers to the RQs.

The studies were based on a broad parameter study, investigating the influence of wind speed, Blade imbalance (BI), BS and assembly tolerances to the EmeIs. In Section 5.3, their implications to the natural frequencies of the system modes have been shown.

The BS has the highest influence to the bearing system mode. Additionally, the added mass for BI and the inclusion of electromagnetic forces affect the natural frequency of the bearing mode.

Analysing the interactions with the aerodynamics showed that the bearing mode, for all BSs investigated here, has a frequency above the cut-off frequency of unsteady aerodynamics and can not lead to interactions. Nevertheless, the Monopile torsion (MT) mode appears as a modulated peak in the spectrum of the aerodynamic forces (see Section 5.4). The modulating frequency equals the rotational speed, and the peak indicates a potential coupling to the aerodynamics. In case the excitation of the torsional mode by the structure is increased, this can have impacts to the aerodynamics. Based on these findings, the first RQ can be answered as follows:

RQ1: Can electro-mechanical interactions have an impact on the aerodynamics of the wind turbine?

Electro-mechanical interactions can only interact with the aerodynamics through their impact to low frequency oscillations below 20 Hz. Such impact can appear by the excitation of the system mode of MT.

Changes of the aerodynamic forces or the WT dynamics can affect the WT loading. Therefore, the loads were analysed in Section 5.6.1. At low wind speeds, the extreme BSs, in both directions, have the highest impact on the 1-Hz-DEL. Unfavourable eEmeIs in WTs with high BSs were also found in [76]. In this work, the tower loads are affected the most. The tower top loading shows the strongest impact for cases with high BSs and the tower bottom loads for cases with low BSs. However, changes to loads can mean an increase or a decrease. Correlations between the parameters of BI or constant eccentricity due to assembly tolerance and the EmeIs have not been identified. The controller was excluded as source of EmeIs based on simulations. However, without retuning, it amplifies them significantly. In combination with the findings on interactions with the aerodynamics, it can be concluded that the changes of loads mainly result from EmeIs within the WT structure. Based on these findings, the second RQ can be answered as follows:

RQ2: Can electro-mechanical interactions increase load levels outside the drive-train?

Electro-mechanical interactions can increase the loads at the turbine's tower-monopile assembly. The exact mechanisms could not be identified based on the results of this work and are the subject of future studies.

The parameter study on EmeIs is based on an analytical description of electromagnetic forces in the generator (cf. Section 4.2.1) and a state-of-the-art WT model with an additional radial DoF for the generator, using a linear spring bearing model (cf. Section 4.1.1). Furthermore, a software coupling (cf. Chapter 3) replacing the analytical generator model with a 2D FEM representation (cf. Section 4.2.2) is developed and applied. For the last RQ about the required model fidelity, different model fidelities are compared. Four levels of model detail were included in the study. Besides the state-of-the-art, the WT model without electromagnetic forces, the model including the analytical description of the electromagnetic forces and the model using the FEM representation of the electromagnetic field are used. Section 5.6.2 shows that the added DoF has significant impact on the loads. Including the electromagnetic forces can increase or decrease the loads. A direct correlation

of the fidelity with the loads can not be identified. However, the three model fidelities show differences in loads to each other.

The model fidelity can change the system modes and the equivalent dynamic bearing loads (see Section 5.5). Compared to the state-of-the-art two-step approach, the bearing load predictions were increased for high BSs, when including the EmeIs. These findings are in line with the results found in [63, 68], where the consideration of electromagnetic forces can lead to 15 to 30 % higher bearing loads. Furthermore, an open loop analysis showed that the controller amplifies the occurring interactions. A controller retuning with the higher model fidelity is therefore recommended.

The comparison of the analytical representation to the FEM representation of the generator forces in Section 5.1 showed a significant excitation of the first Side-to-side (SS) mode for the FEM model. The results from [55], showing SS excitations under voltage dips, support this observation. In addition, the bearings showed additional load oscillations. However, due to the limited simulation time of 15 s, the coupled simulations are not free of numerical transients. To increase computational efficiency, an adaptation of the coupling may be needed in the future and a deeper analysis of the impact of the higher fidelity generator model is recommended for future work. Based on these findings, the third RQ can be answered as follows:

RQ3: What is the needed model fidelity to represent the electro-mechanical interactions with limited computational effort?

As the adapted model shows indications for a load increase at the tower and the main bearings, and potential amplifications of the interactions through the controller, it is recommended to include the radial DoF for the generator and the electromagnetic forces in future dynamic wind turbine load analyses. This will ensure a proper representation of relevant system modes, a proper tuning of the turbine controller and a correct coupling with the aerodynamics. The analytical representation of the electromagnetic forces is considered as minimum requirement. However, the FEM model of the generator can include additional mechanisms of interaction, which could not be studied in detail in this work and are recommended for future investigations.

6.3. Outlook

This work has identified potential EmeIs in WTs, leading to changes in the WT loading and requiring adaptations in WT modelling. However, some assumptions made in this work, require further investigations in the future. These will be outlined in the following and suggestions are made for follow-up RQ, enhancing the understanding of EmeIs in WTs further. The suggestions can be grouped into two main categories: modelling approach and environmental conditions.

For the **modelling approach**, the bearing model, the communication with the aerodynamic solver, the controller design and the electromagnetic model are the major aspects to be investigated in the future. Within this work, the bearing is modelled as a linear radial spring without damping. The assumption of the linear spring and the influence of damping should be revisited. These parameters influence the dynamic displacement of the generator, as they determine the natural frequency of the bearing mode and the amplitude and persistence of the vibrations. A thorough analysis of these parameters will allow the bearing design to be more closely matched to the WT specific load conditions over the service life.

In Section 5.4 the communication frequency with the aerodynamic solver was studied. To limit the computational effort for this work, the frequency was set to 50 Hz, accepting aliasing effects for the bearing mode frequencies. However, this choice introduces an uncertainty into the simulation results. The quantification of this uncertainty requires a more extensive investigation of the interactions with the aerodynamic solver using a higher communication frequency of at least 1250 Hz, to ensure that it is 10 times higher than the highest bearing natural frequency of 123 Hz and avoids the numerical instabilities discussed in Section 5.4.

The WT controller used in this work was designed for the reference WT of the International Energy Agency (IEA). Generally, a controller can be designed and tuned to avoid or reduce unfavourable interactions. This work aimed to identify and understand these interactions rather than avoiding them. Therefore, the controller is not retuned for the electro-mechanical model in this study. However, a controller retuning to avoid the amplifications of interactions is recommended. A comparison of the retuned controller to the given controller will add a deeper understanding to the reason, why the given controller amplifies the EmeIs.

The software coupling, developed in Chapter 3, has been validated based on measurements. However, the required computational effort for the coupling is beyond the available computational capabilities, when running fully coupled simulations for WTs. In the meantime, a general interface software framework, called preCICE [92], was developed by others. This interface could significantly speed up the coupled simulations and allow longer high fidelity analysis in the future.

The analytical generator model and the high fidelity model showed differences in the excitation of SS vibrations. Furthermore, high-frequency oscillations were introduced by the high fidelity generator into the drive-train, which did not occur for the analytical model. In case the high fidelity coupling can be speeded up, a broader comparison of the two models is recommended. Based on the results of such a comparison, the analytical model could potentially be adapted, to include the higher frequency excitations from the electromagnetic forces.

This work aims to isolate EmeIs for the radial DoF in the drive-train. Therefore, the tilting DoF of the generator was neglected. Literature, however, has shown that the tilting DoF can introduce EmeIs into the drive-train. Thus, the impact of this DoF should be investigated in the future.

In this work, the **environmental conditions** were limited to turbulent wind inflow with zero yaw misalignment and hydrodynamics are neglected. As the tower loading shows sensitivity to EmeIs, the interference with the loads and damping coming from the hydrodynamics can be relevant. In addition, cases of yaw misalignment, wind direction changes or other events in the wind inflow should be considered.

New trends in offshore wind energy have lead to floating WTs. These WTs experience higher dynamics through the movements of the floater. It has been shown in literature, that the accelerations experienced by the drive-train of floating WTs can increase compared to accelerations in bottom fixed WTs. Current floater designs have a limit on the tower top accelerations, to keep the drive-train loading within the design limits. However, literature has shown that increased main bearing loads do not correlate with nacelle accelerations [79], suggesting a more complex dependency of floater design and drive-train loads. Using the modelling approach introduced in this work, an extended understanding of the floating offshore WT as a system can be gained. This can potentially support the enhancement of

design requirements of floating offshore WTs in the future.

When the assumptions, made in this work, have been revisited and the uncertainty of the modelling, based on the analytical generator model, can be estimated, the lifetime of a WT can be determined. This work shows the implications of EmeIs on the WT loading for extreme turbulence in the inflow conditions. However, an operating WT experiences many different environmental conditions throughout the lifetime. Thus, to fully evaluate the relevance of EmeIs to the WT design, all possible design and operating conditions should be investigated.

Bibliography

[1] D. Quinn. *Beyond civilization: Humanity's next great adventure*. Crown, 2000 (cit. on p. 23).

[2] E. Commission, J. R. Centre, T. Telsnig, A. Georgakaki, S. Letout, A. Kuokkanen, A. Mountraki, E. Ince, D. Shtjefni, G. Joanny Ordonez, O. Eulaerts, M. Grabowska. *Clean Energy Technology Observatory, Wind energy in the European Union : status report on technology development, trends, value chains and markets : 2022*. Publications Office of the European Union, 2022. DOI: doi/10.2760/855840 (cit. on p. 23).

[3] J. P. Gijs van Kuik. *Long-term Research Challenges in Wind Energy - A Research Agenda by the European Academy of Wind Energy*. Ed. by G. van Kuik, J. Peinke. Vol. 6. Research Topics in Wind Energy. Cham: Springer International Publishing, 2016. DOI: 10.1007/978-3-319-46919-5 (cit. on pp. 23, 29).

[4] A. Durakovic. 'World's First 16 MW Offshore Wind Turbine Rolls Off Production Line'. In: *offshoreWind.biz* (Nov. 2022). accessed : 19.06.2023 (cit. on p. 23).

[5] J. Liu, H. Lin, J. Zhang. 'Review on the technical perspectives and commercial viability of vertical axis wind turbines'. In: *Ocean Engineering* 182 (2019), pp. 608–626. DOI: https://doi.org/10.1016/j.oceaneng.2019.04.086 (cit. on p. 26).

[6] B. Stoevesandt, G. Schepers, P. Fuglsang, Y. Sun, eds. *Handbook of Wind Energy Aerodynamics*. Cham: Springer International Publishing, 2022. DOI: 10.1007/978-3-030-31307-4 (cit. on pp. 26, 27, 35).

[7] S. Struggl, V. Berbyuk, H. Johansson. 'Review on wind turbines with focus on drive train system dynamics'. In: *Wind Energy* 18.4 (Apr. 2015), pp. 567–590. DOI: 10.1002/we.1721 (cit. on p. 27).

[8] A. R. Nejad, J. Keller, Y. Guo, S. Sheng, H. Polinder, S. Watson, J. Dong, Z. Qin, A. Ebrahimi, R. Schelenz, F. Gutiérrez Guzmán, D. Cornel, R. Golafshan, G. Jacobs, B. Blockmans, J. Bosmans, B. Pluymers, J. Carroll, S. Koukoura, E. Hart, A. McDonald, A. Natarajan, J. Torsvik, F. K. Moghadam, P.-J. Daems, T. Verstraeten, C. Peeters, J. Helsen. 'Wind turbine drivetrains: state-of-the-art

technologies and future development trends'. In: *Wind Energy Science* 7.1 (Feb. 2022), pp. 387–411. DOI: 10.5194/wes-7-387-2022 (cit. on pp. 27, 29).

[9] M. D. Reder, E. Gonzalez, J. J. Melero. 'Wind turbine failures-tackling current problems in failure data analysis'. In: *Journal of Physics: Conference Series*. Vol. 753. IOP Publishing. 2016, p. 072027 (cit. on pp. 28, 31).

[10] E. Hart, B. Clarke, G. Nicholas, A. Kazemi Amiri, J. Stirling, J. Carroll, R. Dwyer-Joyce, A. McDonald, H. Long. 'A review of wind turbine main bearings: design, operation, modelling, damage mechanisms and fault detection'. In: *Wind Energy Science* 5.1 (Jan. 2020), pp. 105–124. DOI: 10.5194/wes-5-105-2020 (cit. on p. 28).

[11] W. Finley, M. Hodowanec, W. Holter. 'An analytical approach to solving motor vibration problems'. In: *Industry Applications Society 46th Annual Petroleum and Chemical Technical Conference (Cat.No. 99CH37000)*. IEEE, 1999, pp. 217–232. DOI: 10.1109/PCICON.1999.806440 (cit. on p. 31).

[12] M. Valavi. 'Mostafa Valavi Magnetic Forces and Vibration in Wind Power Generators Analysis of Fractional-Slot Low-Speed PM Machines with Concentrated Windings'. PhD thesis. Norwegian University of Science and Technology, Aug. 2015, p. 63 (cit. on p. 31).

[13] J. Sopanen, V. Ruuskanen, J. Nerg, J. Pyrhönen. 'Dynamic torque analysis of a wind turbine drive train including a direct-driven permanent-magnet generator'. In: *IEEE Transactions on Industrial Electronics* 58.9 (2011), pp. 3859–3867. DOI: 10.1109/TIE.2010.2087301 (cit. on p. 31).

[14] G. Shrestha, H. Polinder, J. Ferreira. 'Scaling laws for direct drive generators in wind turbines'. In: *2009 IEEE International Electric Machines and Drives Conference*. IEEE, May 2009, pp. 797–803. DOI: 10.1109/IEMDC.2009.5075295 (cit. on p. 31).

[15] A. S. McDonald, M. A. Mueller, H. Polinder. 'Structural mass in direct-drive permanent magnet electrical Generators'. In: *European Wind Energy Conference and Exhibition 2007, EWEC 2007* 1.1 (2007), pp. 48–56. DOI: 10.1049/iet-rpg (cit. on p. 31).

[16] M. A. Mueller, A. S. McDonald. 'A lightweight low-speed permanent magnet electrical generator for direct-drive wind turbines'. In: *Wind Energy* 12.8 (2009), pp. 768–780. DOI: 10.1002/we.333 (cit. on p. 32).

[17] G. Shrestha, H. Polinder, D. J. Bang, J. A. Ferreira. 'Structural flexibility: A solution for weight reduction of large direct-drive wind-turbine generators'. In: *IEEE Transactions on Energy Conversion* 25.3 (2010), pp. 732–740. DOI: 10.1109/TEC.2010.2048713 (cit. on p. 32).

[18] A. Hayes, L. Sethuraman, K. Dykes, L. J. Fingersh. 'Structural Optimization of a Direct-Drive Wind Turbine Generator Inspired by Additive Manufacturing'. In: *Procedia Manufacturing* 26 (2018), pp. 740–752. DOI: 10.1016/j.promfg.2018.07.084 (cit. on p. 32).

[19] V. Delli Colli, F. Marignetti, C. Attaianese. 'Analytical and multiphysics approach to the optimal design of a 10-MW DFIG for direct-drive wind turbines'. In: *IEEE Transactions on Industrial Electronics* 59.7 (2012), pp. 2791–2799. DOI: 10.1109/TIE.2011.2168790 (cit. on p. 32).

[20] K. Tartt, A. K. Amiri, A. McDonald, P. Jaen-Sola. 'Structural optimisation of offshore direct-drive wind turbine generators including static and dynamic analyses'. In: *Journal of Physics: Conference Series* 2018.1 (2021). DOI: 10.1088/1742-6596/2018/1/012040 (cit. on p. 32).

[21] M. Kirschneck, H. Polinder, R. A. J. V. Ostayen, F. C. M. V. Kempen, D. J. Rixen. 'Structural Dynamic Topology Optimisation of a Direct-Drive Single Bearing Wind Turbine Generator'. In: *11th World Congress on Structural and Multidisciplinary Optimization*. Sydney, 2015, pp. 1–6 (cit. on p. 32).

[22] P. Jaen-Sola, A. S. McDonald, E. Oterkus. 'Dynamic structural design of offshore direct-drive wind turbine electrical generators'. In: *Ocean Engineering* 161 (2018), pp. 1–19. DOI: 10.1016/j.oceaneng.2018.04.074 (cit. on p. 32).

[23] P. Jaen-Sola, E. Oterkus, A. S. McDonald. 'Parametric lightweight design of a direct-drive wind turbine electrical generator supporting structure for minimising dynamic response'. In: *Ships and Offshore Structures* 16.S1 (2021), pp. 266–274. DOI: 10.1080/17445302.2021.1927356 (cit. on p. 32).

[24] E. Gaertner, J. Rinker, L. Sethuraman, B. Anderson, F. Zahle, G. Barter, N. Abbas, F. Meng, P. Bortolotti, W. Skrzypinski, G. Scott, R. Feil, H. Bredmose, K. Dykes, M. Shields, C. Allen, A. Viselli. *Definition of the IEA 15-Megawatt Offshore Reference Wind*. Tech. rep. 2020, pp. 1–44 (cit. on pp. 33, 34, 61, 84).

[25] J. M. Jonkman, M. L. Buhl Jr. *Fast user's guide-updated august 2005*. Tech. rep. National Renewable Energy Lab.(NREL), Golden, CO (United States), 2005 (cit. on p. 33).

[26] N. J. Abbas, D. S. Zalkind, L. Pao, A. Wright. 'A reference open-source controller for fixed and floating offshore wind turbines'. In: *Wind Energy Science* 7.1 (Jan. 2022), pp. 53–73. DOI: 10.5194/wes-7-53-2022 (cit. on p. 33).

[27] A. Gambier. *Control of Large Wind Energy Systems*. Advances in Industrial Control. Cham: Springer International Publishing, 2022. DOI: 10.1007/978-3-030-84895-8 (cit. on pp. 35, 112).

[28] O. A. Bauchau, J. I. Craig. 'Euler-Bernoulli beam theory'. In: 2009, pp. 173–221. DOI: 10.1007/978-90-481-2516-6_5 (cit. on p. 36).

[29] B. E. Abali, C. Çakıroğlu. *Numerische Methoden für Ingenieure*. Berlin, Heidelberg: Springer Berlin Heidelberg, 2020. DOI: 10.1007/978-3-662-61325-2 (cit. on p. 37).

[30] J. Donnevert. *Maxwell´s Equations*. Wiesbaden: Springer Fachmedien Wiesbaden, 2020. DOI: 10.1007/978-3-658-29376-5 (cit. on p. 37).

[31] J. A. Melkebeek. *Electrical Machines and Drives*. Springer, 2018 (cit. on pp. 37, 40).

[32] A. Bonfiglio, F. Delfino, F. Gonzalez-Longatt, R. Procopio. 'Steady-state assessments of PMSGs in wind generating units'. In: *International Journal of Electrical Power & Energy Systems* 90 (Sept. 2017), pp. 87–93. DOI: 10.1016/j.ijepes.2017.02.002 (cit. on p. 39).

[33] P. Jaen-Sola. 'Advanced structural modelling and design of wind turbine electrical generators'. PhD. University of Strathclyde, 2017 (cit. on pp. 39, 88).

[34] F. D. Lüdecke, M. Schmid, E. Rehe, S. Panneer Selvam, N. Parspour, P. W. Cheng. 'Numerical Aspects of a Two-Way Coupling for Electro-Mechanical Interactions-A Wind Energy Perspective'. In: *Energies* 15.3 (2022). DOI: 10.3390/en15031178 (cit. on pp. 41, 43, 44, 61, 62, 64, 71–74).

[35] W. G. Dettmer, D. Perić. 'A new staggered scheme for fluid–structure interaction'. In: *International Journal for Numerical Methods in Engineering* 93.1 (2013), pp. 1–22. DOI: https://doi.org/10.1002/nme.4370 (cit. on p. 42).

[36] J. M. Jonkman, M. L. Buhl, et al. *FAST user's guide*. Vol. 365. National Renewable Energy Laboratory Golden, CO, USA, 2005 (cit. on pp. 47, 113).

[37] W. Popko, M. L. Huhn, A. Robertson, J. Jonkman, F. Wendt, K. Müller, M. Kretschmer, F. Vorpahl, T. R. Hagen, C. Galinos, J.-B. Le Dreff, P. Gilbert, B. Auriac, F. N. Víllora, P. Schünemann, I. Bayati, M. Belloli, S. Oh, Y. Totsuka, J. Qvist, E. Bachynski, S. H. Sørum, P. E. Thomassen, H. Shin, F. Vittori, J. Galván, C. Molins, P. Bonnet, T. van der Zee, R. Bergua, K. Wang, P. Fu, J. Cai. 'Verification of a Numerical Model of the Offshore Wind Turbine From the Alpha Ventus Wind Farm Within OC5 Phase III'. In: International Conference on Offshore Mechanics and Arctic Engineering Volume 10: Ocean Renewable Energy (June 2018), V010T09A056. DOI: 10.1115/OMAE2018-77589 (cit. on p. 47).

[38] *SIMPACK - MultiBody System Simulation Software by Dassault Systèmes*. Version 2021 (cit. on pp. 47, 68).

[39] X. Xu, Q. Han, F. Chu. 'Review of Electromagnetic Vibration in Electrical Machines'. In: *Energies* 11.7 (July 2018), p. 1779. DOI: 10.3390/en11071779 (cit. on p. 49).

[40] H. Jordan, R.-D. Schroeder, H. O. Seinsch. 'Zur Berechnung einseitig magnetischer Zugkräfte in Drehfeldmaschinen'. In: *Electrical Engineering (Archiv fur Elektrotechnik)* 63.2 (1981), pp. 117–124 (cit. on p. 50).

[41] P. Pennacchi. 'Computational model for calculating the dynamical behaviour of generators caused by unbalanced magnetic pull and experimental validation'. In: *Journal of Sound and Vibration* 312.1-2 (Apr. 2008), pp. 332–353. DOI: 10.1016/j.jsv.2007.10.052 (cit. on p. 50).

[42] U. Werner. 'Elastic multiple-mass model for rotordynamic analysis of flexible electrical rotors'. In: *Forschung im Ingenieurwesen* 75.4 (Dec. 2011), pp. 209–229. DOI: 10.1007/s10010-011-0146-3 (cit. on p. 50).

[43] F. Boy, H. Hetzler. 'A Co-energy Based Approach to Model the Rotordynamics of Electrical Machines'. In: *Mechanisms and Machine Science*. Vol. 63. Springer International Publishing, 2019, pp. 190–204. DOI: 10.1007/978-3-319-99272-3_14 (cit. on pp. 50, 77).

[44] L. Wang, R. Cheung, Z. Ma, J. Ruan, Ying Peng. 'Finite-Element Analysis of Unbalanced Magnetic Pull in a Large Hydro-Generator Under Practical Operations'. In: *IEEE Transactions on Magnetics* 44.6 (June 2008), pp. 1558–1561. DOI: 10.1109/TMAG.2007.916023 (cit. on p. 50).

[45] K. Hameyer, S. Böhmer, I. Coenen, D. Eggers, M. Felden, D. Franck, M. Hafner, F. Henrotte, T. Herold, M. Hombitzer, E. Lange, P. Offermann, B. Riemer, S. Steentjes. 'The art of modelling Electrical Machines'. In: *ICS Newsletter, International Compumag Society* 19.2 (2012), pp. 3–19 (cit. on p. 50).

[46] J. Martinez, A. Belahcen, J. Detoni. 'A 2D magnetic and 3D mechanical coupled finite element model for the study of the dynamic vibrations in the stator of induction motors'. In: *Mechanical Systems and Signal Processing* 66-67 (Jan. 2016), pp. 640–656. DOI: 10.1016/j.ymssp.2015.06.014 (cit. on p. 50).

[47] F. Boy, H. Hetzler. 'On the electromechanical coupling in rotordynamics of electrical machines'. In: *Pamm* 17.1 (2017), pp. 365–366. DOI: 10.1002/pamm.201710152 (cit. on p. 50).

[48] T. Duda, G. Jacobs, D. Bosse. 'Investigation of Modelling Depths for an Electromechanical Simulation of a Direct-Drive Generator Considering Parasitic Airgap Forces and External Loads'. In: *Journal of Physics: Conference Series* 1222.1 (May 2019), p. 012029. DOI: 10.1088/1742-6596/1222/1/012029 (cit. on pp. 50, 54, 96).

[49] T. P. Holopainen, A. Tenhunen, A. Arkkio. 'Electromechanical Interaction in Rotor Vibrations of Electric Machines'. In: *Proceedings of the 5th World Congress on Computational Mechanics*. Vienna, 2002 (cit. on p. 50).

[50] F. Mei, B. Pal. 'Modal Analysis of Grid-Connected Doubly Fed Induction Generators'. In: *IEEE Transactions on Energy Conversion* 22.3 (Sept. 2007), pp. 728–736. DOI: 10.1109/TEC.2006.881080 (cit. on p. 51).

[51] J. Carmona-Sanchez, Z. Lin, M. Collu, M. Barnes, O. Marjanovic, D. Cevasco. 'An analysis of the impact of an advanced aero-hydro-servo-elastic model of dynamics on the generator-converter dynamics, for an offshore fixed 5MW PMSG wind turbine'. In: *15th IET International Conference on AC and DC Power Transmission (ACDC 2019)*. Vol. 2019. CP751. Institution of Engineering and Technology, 2019, 80 (6 pp.)–80 (6 pp.) DOI: 10.1049/cp.2019.0080 (cit. on p. 51).

[52] J. Diao, H. Zhao, B. Li, L. Niu. 'Refined Modeling and Real-Time Simulation of DFIG Based Wind Farm'. In: *2020 IEEE/IAS Industrial and Commercial Power System Asia, I and CPS Asia 2020* 51707106 (2020), pp. 1416–1420. DOI: 10.1109/ICPSAsia48933.2020.9208540 (cit. on p. 52).

[53] A. Lorenzo-Bonache, A. Honrubia-Escribano, F. Jiménez-Buendía, Á. Molina-García, E. Gómez-Lázaro. 'Generic type 3 wind turbine model based on IEC 61400-27-1: Parameter analysis and transient response under voltage dips'. In: *Energies* 10.9 (2017), pp. 1–23. DOI: 10.3390/en10091441 (cit. on p. 52).

[54] R. Fadaeinedjad, M. Moallem, G. Moschopoulos. 'Simulation of a wind turbine with doubly fed induction generator by FAST and Simulink'. In: *IEEE Transactions on Energy Conversion* 23.2 (2008), pp. 690–700. DOI: 10.1109/TEC.2007.914307 (cit. on p. 52).

[55] R. Fadaeinedjad, G. Moschopoulos, M. Moallem. 'Investigation of voltage sag impact on wind turbine tower vibrations'. In: *Wind Energy* 11.4 (2008), pp. 351–375. DOI: 10.1002/we.266 (cit. on pp. 52, 153).

[56] J. Röder, G. Jacobs, T. Duda, D. Bosse, F. Herzog. 'Investigation of dynamic loads in wind turbine drive trains due to grid and power converter faults'. In: *Energies* 14.24 (2021). DOI: 10.3390/en14248542 (cit. on p. 52).

[57] A. Staino, B. Basu, M. Basu. 'Suppression of grid fault-induced vibration in wind turbines using UPQC'. In: *2014 IEEE 5th International Symposium on Power Electronics for Distributed Generation Systems (PEDG)*. IEEE, June 2014, pp. 1–8. DOI: 10.1109/PEDG.2014.6878663 (cit. on p. 52).

[58] M. Wiens, S. Frahm, P. Thomas, S. Kahn. 'Holistic simulation of wind turbines with fully aero-elastic and electrical model'. In: *Forschung im Ingenieurwesen/Engineering Research* 85.2 (2021), pp. 417–424. DOI: 10.1007/s10010-021-00479-6 (cit. on p. 52).

[59] B. Novakovic, Y. Duan, M. Solvenson, A. Nasiri, D. M. Ionel. 'Multi-physics system simulation for wind turbines with permanent magnet generator and full conversion power electronics'. In: *Proceedings of the 2013 IEEE International Electric Machines and Drives Conference, IEMDC 2013* (2013), pp. 541–548. DOI: 10.1109/IEMDC.2013.6556148 (cit. on p. 53).

[60] D. S. Ochs, R. D. Miller, W. N. White. 'Simulation of electromechanical interactions of permanent-magnet direct-drive wind turbines using the fast aeroelastic simulator'. In: *IEEE Transactions on Sustainable Energy* 5.1 (2014), pp. 2–9. DOI: 10.1109/TSTE.2013.2269681 (cit. on p. 53).

[61] P. Li, D. Lu, R. Schmoll, B. Schweizer. 'Explicit Co-simulation Approach with Improved Numerical Stability'. In: *IUTAM Bookseries*. Vol. 35. 2019, pp. 153–201. DOI: 10.1007/978-3-030-14883-6_9 (cit. on p. 53).

[62] I. P. Girsang, J. S. Dhupia, E. Muljadi, M. Singh, L. Y. Pao. 'Gearbox and drivetrain models to study dynamic effects of modern wind turbines'. In: *IEEE Transactions on Industry Applications* 50.6 (2014), pp. 3777–3786. DOI: 10.1109/TIA.2014.2321029 (cit. on p. 53).

[63] J. Gallego-Calderon, A. Natarajan. 'Assessment of wind turbine drive-train fatigue loads under torsional excitation'. In: *Engineering Structures* 103 (2015), pp. 189–202. DOI: 10.1016/j.engstruct.2015.09.008 (cit. on pp. 53, 153).

[64] M. Michon, R. C. Holehouse, K. Atallah, G. Johnstone. 'Effect of rotor eccentricity in large synchronous machines'. In: *IEEE Transactions on Magnetics* 50.11 (2014). DOI: 10.1109/TMAG.2014.2330452 (cit. on p. 53).

[65] F. Fateh, W. N. White, D. Gruenbacher. 'Torsional Vibrations Mitigation in the Drivetrain of DFIG-Based Grid-Connected Wind Turbine'. In: *IEEE Transactions on Industry Applications* 53.6 (2017), pp. 5760–5767. DOI: 10.1109/TIA.2017.2730159 (cit. on p. 53).

[66] F. Fateh, W. N. White, D. Gruenbacher. 'Mitigation of torsional vibrations in the drivetrain of DFIG-based grid-connected wind turbine'. In: *2015 IEEE Energy Conversion Congress and Exposition (ECCE)*. Vol. 53. 6. IEEE, Sept. 2015, pp. 4159–4164. DOI: 10.1109/ECCE.2015.7310247 (cit. on p. 53).

[67] A. Bartschat, M. Morisse, A. Mertens, J. Wenske. 'Analysis of Dynamic Interactions between Different Drivetrain Components with a Detailed Wind Turbine Model'. In: *Journal of Physics: Conference Series* 753.8 (2016). DOI: 10.1088/1742-6596/753/8/082022 (cit. on pp. 53, 55).

[68] D. Matzke, S. Rick, S. Hollas, R. Schelenz, G. Jacobs, K. Hameyer. 'Coupling of electromagnetic and structural dynamics for a wind turbine generator'. In: *Journal of Physics: Conference Series* 753.8 (2016). DOI: 10.1088/1742-6596/753/8/082034 (cit. on pp. 54, 96, 153).

[69] A. Baseer, Y. He, R. Schelenz, A. Kari, B. Roscher, G. Jacobs. 'Comparison of a Direct Drive Wind Turbine with and without LSS-Coupling Regarding Air Gap Displacement'. In: *Journal of Physics: Conference Series* 1618.5 (2020). DOI: 10.1088/1742-6596/1618/5/052004 (cit. on p. 54).

[70] *BEARINX-online Shaft Calculation by Schaeffler Technologies AG & Co. KG* (cit. on p. 54).

[71] C. Mülder, T. Duda, G. Jacobs, K. Hameyer. 'Model approach for electromagnetically excited mechanical vibrations in direct-drive wind turbines'. In: *Journal of Physics: Conference Series* 1618.2 (2020). DOI: 10.1088/1742-6596/1618/2/022060 (cit. on p. 54).

[72] M. Cardaun, R. Schelenz, G. Jacobs, T. Duda. 'Calculation of structure-borne sound in a direct drive wind turbine'. In: *Forschung im Ingenieurwesen/Engineering Research* 85.2 (2021), pp. 165–171. DOI: 10.1007/s10010-021-00443-4 (cit. on p. 55).

[73] T. Duda, C. Mülder, G. Jacobs, K. Hameyer, D. Bosse, M. Cardaun. 'Integration of electromagnetic finite element models in a multibody simulation to evaluate vibrations in direct-drive generators'. In: *Forschung im Ingenieurwesen/Engineering Research* 85.2 (2021), pp. 257–264. DOI: 10.1007/s10010-021-00472-z (cit. on p. 55).

[74] M. Cardaun, C. Mülder, T. Decker, B. Dilba, T. Duda, R. Schelenz, G. Jacobs, K. Hameyer, S. Keuchel. 'Multi-Physical Simulation Toolchain for the Prediction of Acoustic Emissions of Direct Drive Wind Turbines'. In: *Journal of Physics: Conference Series* 2265.4 (2022). DOI: 10.1088/1742-6596/2265/4/042047 (cit. on p. 55).

[75] Y. Xing, M. Karimirad, T. Moan. 'Modelling and analysis of floating spar-type wind turbine drivetrain'. In: *Wind Energy* 17.4 (Apr. 2014), pp. 565–587. DOI: 10.1002/we.1590 (cit. on p. 55).

[76] L. Sethuraman, V. Venugopal, A. Zavvos, M. Mueller. 'Structural integrity of a direct-drive generator for a floating wind turbine'. In: *Renewable Energy* 63 (2014), pp. 597–616. DOI: 10.1016/j.renene.2013.10.024 (cit. on pp. 55, 56, 152).

[77] A. R. Nejad, E. E. Bachynski, M. I. Kvittem, C. Luan, Z. Gao, T. Moan. 'Stochastic dynamic load effect and fatigue damage analysis of drivetrains in land-based and TLP, spar and semi-submersible floating wind turbines'. In: *Marine Structures* 42.7491 (2015), pp. 137–153. DOI: 10.1016/j.marstruc.2015.03.006 (cit. on pp. 55, 56).

[78] L. Sethuraman, Y. Xing, V. Venugopal, Z. Gao, M. Mueller, T. Moan. 'A 5 MW direct-drive generator for floating spar-buoy wind turbine: Drive-train dynamics'. In: *Proceedings of the Institution of Mechanical Engineers, Part C: Journal of Mechanical Engineering Science* 231.4 (2017), pp. 744–763. DOI: 10.1177/0954406215623306 (cit. on pp. 55, 58, 77, 121, 123).

[79] A. R. Nejad, E. E. Bachynski, T. Moan. 'Effect of axial acceleration on drivetrain responses in a spar-type floating wind turbine'. In: *Journal of Offshore Mechanics and Arctic Engineering* 141.3 (2019), pp. 1–7. DOI: 10.1115/1.4041996 (cit. on pp. 56, 77, 155).

[80] *IEC 60404-4: Magnetic materials-Part 4: Methods of measurement of dc magnetic properties of magnetically soft materials*. Standard. Geneva, CH: IEC - International Electrotechnical Commission, Nov. 2008 (cit. on pp. 67, 179).

[81] K. E. Brenan, S. L. Campbell, L. R. Petzold. *Numerical solution of initial-value problems in differential-algebraic equations*. SIAM, 1995 (cit. on p. 68).

[82] J. Chung, G. M. Hulbert. 'A Time Integration Algorithm for Structural Dynamics With Improved Numerical Dissipation: The Generalized-α Method'. In: *Journal of Applied Mechanics* 60.2 (June 1993), pp. 371–375. DOI: 10.1115/1.2900803 (cit. on p. 68).

[83] *COMSOL Multiphysics-Documentation by Comsol Multiphysics GmbH*. https://doc.comsol.com/5.6/docserver/#!/com.comsol.help.comsol/comsol_ref_mesh.20.19.html?highlight=skewness. accessed : 24.03.2023 (cit. on p. 68).

[84] B. Ratner. 'The correlation coefficient: Its values range between+ 1/- 1, or do they?' In: *Journal of targeting, measurement and analysis for marketing* 17.2 (2009), pp. 139–142 (cit. on pp. 71, 73).

[85] F. D. Lüdecke, M. Schmid, P. W. Cheng. 'Identification of electro-mechanical interactions in wind turbines'. In: *Wind Energy Science Discussions (preprint)* 2024 (2024). in review, pp. 1–25. DOI: 10.5194/wes-2024-13 (cit. on pp. 75, 100).

[86] P. Jaen-Sola, A. McDonald. 'Structural Analysis and Characterization of Radial Flux PM Generators for Direct-Drive Wind Turbines'. In: *3rd Renewable Power Generation Conference (RPG 2014)*. Vol. 2014. CP651. Institution of Engineering and Technology, 2014, pp. 5.3.3–5.3.3. DOI: 10.1049/cp.2014.0866 (cit. on p. 77).

[87] B. J. Jonkman. *TurbSim user's guide*. Tech. rep. National Renewable Energy Lab.(NREL), Golden, CO (United States), 2006 (cit. on p. 108).

[88] *IEC 61400-1: 2019 Wind Energy Generation Systems—Part 1: Design Requirements*. Standard. Geneva, CH: IEC - International Electrotechnical Commission, Feb. 2019 (cit. on p. 109).

[89] *ASTM E1049-85(2017): Standard practices for cycle counting in fatigue analysis*. Standard. West Conshohocken, USA: ASTM International ASTM Committee E-8 on Fatigue and Fracture, June 2017. DOI: 10.1520/E1049-85R17 (cit. on p. 112).

[90] M. Hansen. *Aerodynamics of Wind Turbines: second edition*. English. 2nd ed. Earthscan, 2008 (cit. on p. 119).

[91] B. Schlecht. *Maschinenelemente 2*. Vol. 2. Pearson Deutschland GmbH, 2010 (cit. on pp. 123, 124).

[92] G. Chourdakis, K. Davis, B. Rodenberg, M. Schulte, F. Simonis, B. Uekermann, G. Abrams, H. Bungartz, L. Cheung Yau, I. Desai, K. Eder, R. Hertrich, F. Lindner, A. Rusch, D. Sashko, D. Schneider, A. Totounferoush, D. Volland, P. Vollmer, O. Koseomur. 'preCICE v2: A sustainable and user-friendly coupling library [version 2; peer review: 2 approved]'. In: *Open Research Europe* 2.51 (2022). DOI: 10.12688/openreseurope.14445.2 (cit. on p. 155).

List of Figures

List of Tables

Appendix A

Magnetisation curve of test bench iron cores

Table A.1.: Magnetisation curve of magnetic field H and induction B measured according to [80] for the iron cores of the test bench in Section 3.2.2

H in A/m	B in T	H in A/m	B in T	H in A/m	B in T
0.00	0.000	901.20	0.248	3164.14	0.809
11.42	0.001	1009.81	0.280	3339.02	0.844
29.56	0.002	1120.35	0.313	3515.44	0.879
50.34	0.004	1237.44	0.347	3695.13	0.913
79.79	0.007	1358.83	0.382	3878.20	0.946
113.38	0.011	1484.26	0.417	4061.76	0.979
154.16	0.018	1616.07	0.452	4249.62	1.012
200.94	0.028	1752.82	0.488	4437.06	1.044
256.59	0.043	1893.63	0.524	4627.08	1.075
315.41	0.061	2038.42	0.560	4818.64	1.106
382.38	0.081	2188.62	0.596	5011.54	1.137
455.36	0.105	2342.14	0.632	5205.46	1.166
532.32	0.130	2499.29	0.668	5400.25	1.195
615.79	0.158	2659.93	0.704	5595.05	1.223
706.11	0.186	2825.19	0.739	5791.63	1.251
802.40	0.217	2992.45	0.774	5987.32	1.277

Continued on next page

Table A.1 – continued

H in A/m	B in T	H in A/m	B in T	H in A/m	B in T
6184.15	1.303	9479.29	1.577	13207.87	1.648
6380.71	1.328	9636.96	1.585	15123.63	1.656
6575.35	1.351	9791.26	1.591	17317.28	1.661
6770.85	1.373	9941.28	1.597	19829.11	1.665
6962.24	1.393	10087.04	1.602	22705.27	1.669
7157.37	1.412	10227.74	1.606	25998.62	1.673
7347.85	1.430	10364.13	1.610	29769.65	1.678
7538.08	1.447	10495.88	1.613	34087.67	1.683
7726.85	1.463	10624.17	1.616	39032.00	1.689
7912.88	1.479	10747.19	1.619	44693.50	1.697
8097.32	1.493	10863.50	1.621	51176.12	1.705
8280.42	1.506	10976.80	1.622	58599.11	1.714
8460.29	1.519	11083.17	1.624	67098.78	1.725
8637.01	1.530	11184.09	1.625	76831.34	1.737
8810.87	1.541	11279.35	1.626	87975.53	1.751
8983.73	1.551	11370.05	1.628	100736.18	1.767
9151.88	1.561	11455.04	1.629	103951.42	1.771
9317.89	1.569	11533.77	1.630		

Appendix B

Additional coupling validation cases

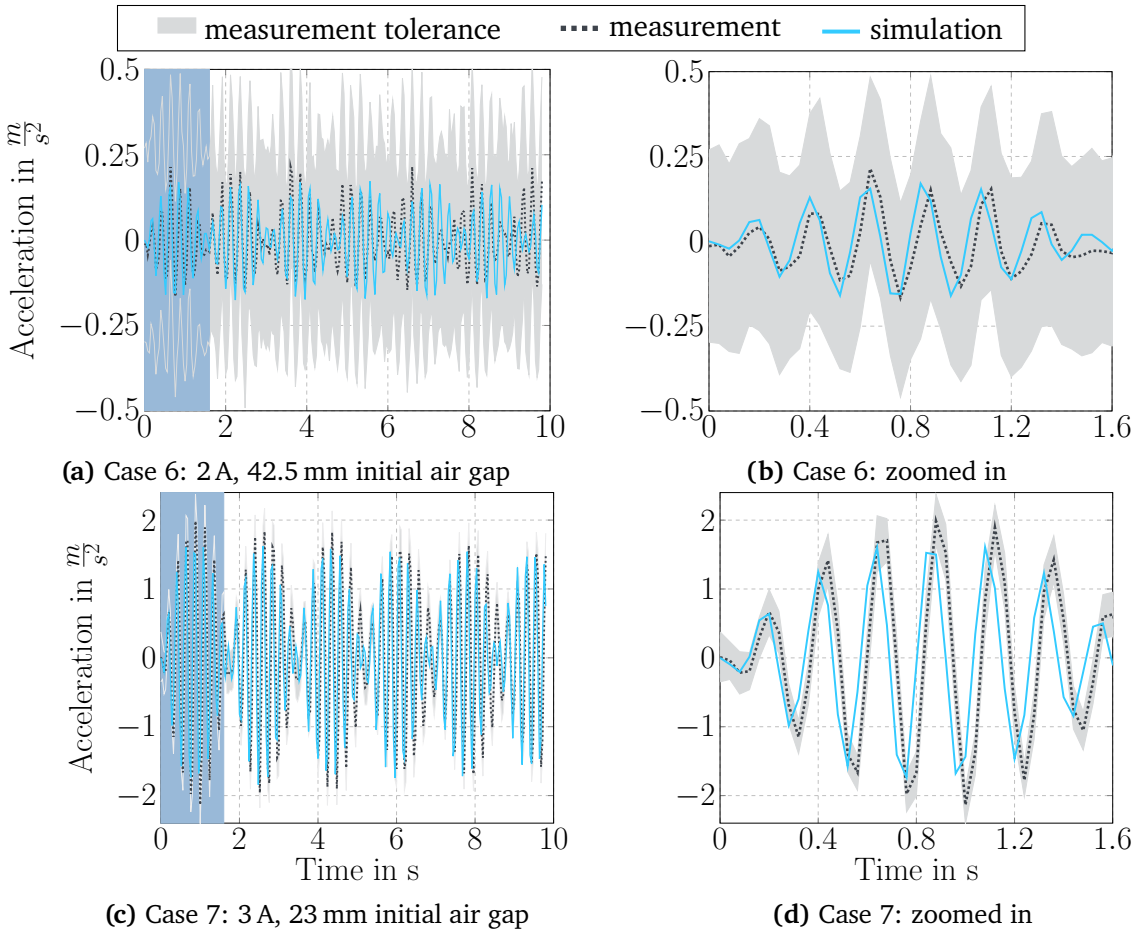

(a) Case 6: 2 A, 42.5 mm initial air gap

(b) Case 6: zoomed in

(c) Case 7: 3 A, 23 mm initial air gap

(d) Case 7: zoomed in

Figure B.1.: Comparison of measured (black) and simulated (blue) dynamic response for validation cases 6 and 7 in Table 3.3, including measurement uncertainties (light grey). Right-hand side: zoom to the first period marked on the left-hand side (blue shaded area).

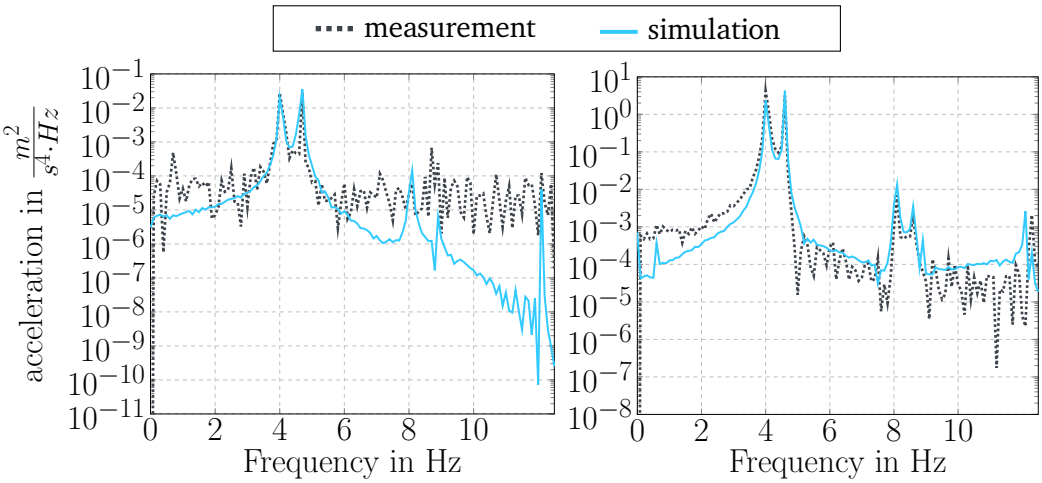

(a) Case 6: 2 A, 42.5 mm initial air gap **(b)** Case 7: 3 A, 23 mm initial air gap

Figure B.2.: Power spectral density (PSD) of the acceleration of the anchor for measurements (black) and simulation (light blue) for the validation cases 6 and 7.

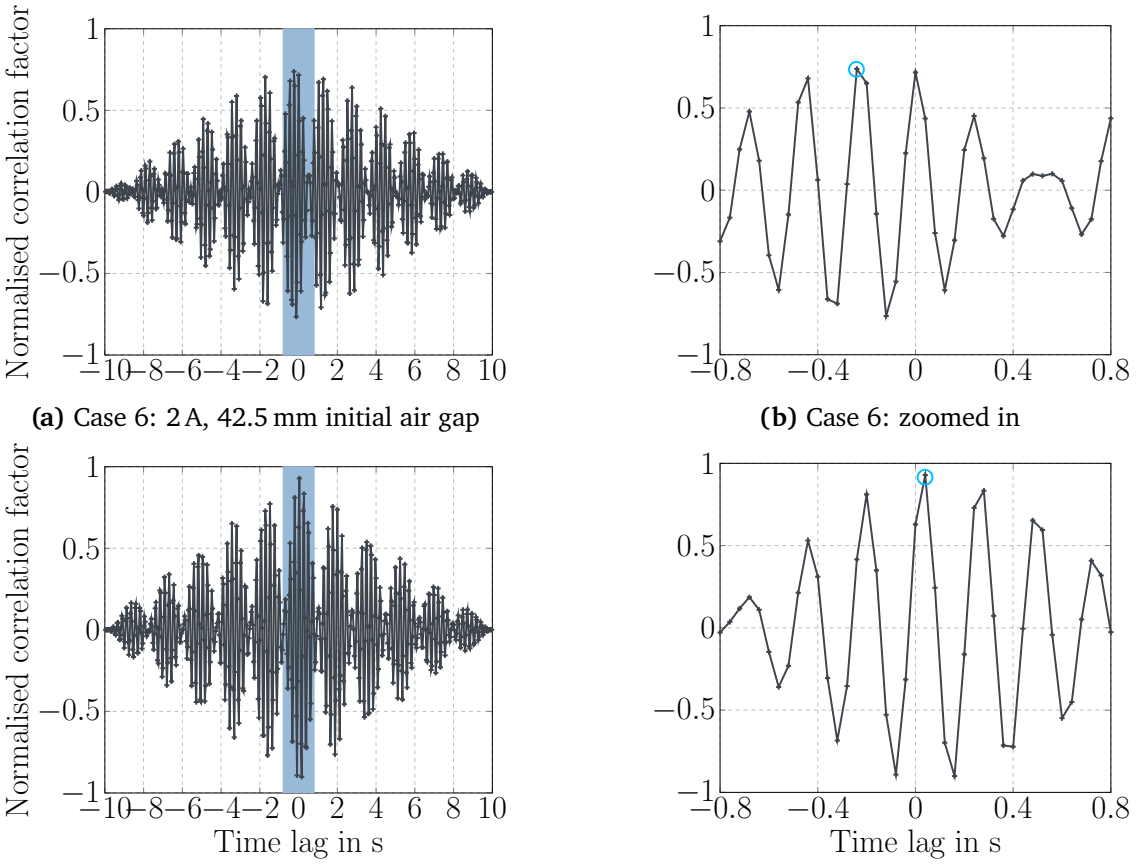

(a) Case 6: 2 A, 42.5 mm initial air gap **(b)** Case 6: zoomed in

(c) Case 7: 3 A, 23 mm initial air gap **(d)** Case 7: zoomed in

Figure B.3.: Normalised cross-correlation factors of the comparison of measurement and simulation for the cases 6 and 7. Right-hand side: zoom of the blue shaded area on the left-hand side; light blue circles: optimal correlation factor; the optimum for case 6: time lag of -0.24s and correlation factor of 0.7375; the optimum for case 7: time lag of 0.04s and correlation factor of 0.9284